Relating chemical structure and molecular packing to charge transport in conjugated polymers

Dissertation
zur Erlangung des Grades
“Doktor der Naturwissenschaften”
am Fachbereich Physik, Mathematik und Informatik
der Johannes Gutenberg-Universität
in Mainz

Anton Melnyk

geb. in Kryvyi Rih (UdSSR)
Mainz, den 21 September, 2016

Anton Melnyk
Relating chemical structure and molecular packing to charge transport in conjugated polymers
PhD Thesis

Datum der mündlichen Prüfung: 17 Januar, 2017
1. Berichterstatter: Prof. Dr. Kurt Kremer
2. Berichterstatterin: Prof. Dr. Friederike Schmid

Johannes Gutenberg-Universität Mainz

Physics department
Staudingerweg 9
D55128 , Mainz

Abstract

Polymer solar cells are a promising, renewable source of electricity, which currently exhibit low efficiencies. To improve solar cell performance, one needs to understand how microscopic processes are linked to the material's chemistry, local ordering, and macroscopic composition. In the following a combination of first-principles calculations, molecular dynamics simulations, perturbative energy calculations and, Marcus charge transfer theory are used for multiscale studies of two polymer systems, Poly[2,6-(4,4-bis-(2-ethylhexyl)-4H-cyclopenta [2,1-b;3,4-b'] dithiophene)-alt-4,7(2,1,3-benzothiadiazole)] (PCPDTBT) and Poly[2,5-bis (3-tetradecylthiophen-2-yl) thieno [3,2-b] thiophene] (PBTTT).

In PCPDTBT and its four derivatives, a number of possible crystalline morphologies are simulated in a bottom-up scheme, starting from the chemical structure. Four polymorphs, including two π-stacked configurations, are found and verified against experimental data. Also, the key degrees of freedom, responsible for crystal formation, are identified. In π-stacked structures, transfer integrals, site energies, and mobilities are calculated. The calculated energetic disorder is high and comparable to the one in amorphous materials. It originates from electrostatics of individual donor and acceptor units in the backbone and from the disordered structure of the side-chains. Chemical substitution increases the disorder, while the push-pull architecture has no effect on it. Resulting mobilities are hindered by the large energetic disorder.

For the second polymer, PBTTT, the available NMR data is combined with molecular dynamics simulations and an analytical model to assess its dynamics and macroscopic composition. The dynamics is addressed via a generalized order parameter. Elevated temperature MD simulations are used to extrapolate side-chain dynamics to the μs time-scale. The macroscopic composition is resolved via an analytical model which combines microscopic parameters obtained from simulations and macroscopic averages extracted from NMR measurements. The original NMR data suggests a two-mesophase composition with $1:1$ crystalline to amorphous mesophase ratio. In combination with the analytical model and simulations, a three-mesophase model is proposed in which crystalline, intermediate and amorphous mesophases have 8%, 42% and 50% volume fractions. A formula is derived, which can be used to interpret the crystalline composition of other semi-crystalline polymers.

Zusammenfassung

Solarzellen aus Polymeren sind vielversprechende, erneuerbare Energiequellen, die zur Zeit aber durch ihren geringen Wirkungsgrad limitiert sind. Um die Effizienz zu steigern, muss der Einfluss der chemischen Zusammensetzung des Materials, der lokalen mesokopischen Ordnung und des makrospischen Aufbaus auf die mikroskopischen Prozesse geklärt werden. Im Folgenden wurden Multi-Skalensimulationen verwendet, die eine Kombination aus ab initio Rechnungen, molekulardynamischen Simulationen, Störungstheorie und Markus-Theorie benutzen, um diesen Zusammenhang für die zwei Polymere Poly[2,6-(4,4-bis-(2-ethylhexyl)-4H-cyclopenta [2,1-b;3,4-b'] dithiophene)-alt-4,7(2,1,3- benzothiadiazole)] (PCPDTBT) und Poly[2,5-bis (3-tetradecylthiophen-2-yl) thieno [3,2-b] thiophene] (PBTTT) zu untersuchen.

Mit Hilfe eines Bottom-Up Ansatzes wurden ausgehend von der chemischen Struktur kristalline Morphologien für PCPDTBT und seiner vier Derivate simuliert. Vier polymorphe Strukturen, darunter zwei π-π-wechselwirkende Konfigurationen, wurden entdeckt und gegen experimentelle Befunde verifiziert. Ebenso wurden die molekularen Freiheitsgerade, die verantwortlich für die Kristallisation sind, identifiziert. In den π-π-wechselwirkenden Strukturen wurden Transferintegrale, Lageenergien einzelner Moleküle und Mobilitäten berechnet. Die aus den Lageenergien berechnete elektrostatische Unordnung für die kristallinen Strukturen ist hoch und vergleichbar mit Unordnung in amorphen Materialien. Die hohe elektrostatische Unordung wird durch die unterschiedlich geladenen Donatoren und Akzeptoren in der Hauptkette und durch die sehr ungeordnete Struktur der Seitenketten verursacht. Die chemische Substitution einzelner Atome verstärkt diesen Effekt, während die Push-Pull Architektur keinen Einfluss darauf hat. Durch die hohe elektrostatische Unordnung wird die Bewegung der Ladungsträger erschwert und somit die Ladungsträgermobilität gesenkt.

Für das zweite Polymer PBTTT wurden experimentelle NMR Daten mit molekulardynamischen Simulationen und einem analytischen Modell, zur Beurteilung der Polymerdynamik und makroskopischen Zusammensetzung, kombiniert. Die Dynamik wird durch den sogenannten generalisierten Ordnungsparameter charakterisiert. Molekulardynamische Simulationen wurden bei erhöhten Temperaturen durchgeführt um realistische Seitenkettenbewegungen auf der Mikrosekundenskala zu erhalten. Die makroskopische Zusammensetzung wurde dann durch das analytische Modell ermittelt, welches mikroskopische Parameter aus den Simulationen und makroskopische Durchschnittswerte aus den NMR Daten kombiniert. Die ursprünglichen NMR Daten lassen auf zwei Mesophasen, eine kristalline und eine amorphe, die zu gleichen Anteilen vorliegen, schließen. Die Kombination von analytischen Modell mit den Simulationen zeigt, dass ein Modell aus drei Mesophasen, in dem kristalline, gemischte und amorphe Mesophasen in Volumenanteilen von 8%, 42% und 50% vorliegen am wahrscheinlichsten ist. Abschließend wurde eine Gleichung hergeleitet, die es erlaubt, den Anteil der kristallinen Phase in semi-kristallinen Polymere zu bestimmen.

Contents

1 Organic solar cells

Photovoltaic (PV) technology allows one to convert an emitted solar radiation to a direct electric current. It is a renewable, environmentally friendly and one of the most promising sources of energy for future energy requirements, which is expected to replace fossil fuels. Improving the device efficiency and lowering the material costs defines if an emerging technology, such as PV, will become economically viable and competitive. This requires an extensive study of new materials and physical processes within these materials.

Research on solar cells began in the 1950s with building the first *in*organic, silicon-based solar cells with a power conversion efficiency (PCE) of 6% for space applications [1, 2]. To date, this is the most used solar cell type, and its PCE reaches over 25% in single-junction and 46% in multi-junction devices, according to annual PV progress reports [3, 4]. However, mono- and poly-crystalline *in*organic solar cells have a number of deficiencies, which include fragility, high specific weight and high manufacturing costs. The latter is a consequence of high energy consumption and complexity of the manufacturing process. Alternative solar cell types, based on new materials, were considered over time to overcome these limitations. At present, the best material alternatives are amorphous silicon [5, 6], small organic molecules [7, 8], conjugated polymers [9–11], quantum dots [12, 13], perovskites [14–16] and their combinations. The best conversion efficiencies that were achieved with these materials reach only up to 12% in laboratory conditions [3]. Improvements are required to increase these PCE values and match those in *in*organic solar cells, or even reach a theoretical maximum of 30%, which is known as a Shockley-Queisser limit [17].

This work focuses on organic materials, in particular conjugated semi-crystalline polymers. While polymers are widely used in polymer-based solar cells (PSC) and give highly efficient PV devices [18–21], the relationship between their complicated nano-scale morphologies, opto-electronic properties and their in-device performance is not fully understood [20, 22]. It requires further studies in order to reach the full potential of these materials.

Before one goes into details, it is useful to understand the basic working principles of solar cells, as well as consequences of employing organic materials such as conjugated polymers.

1.1 Characterization of PV devices

A solar cell is a device that converts an incident light to a direct electric current. It is typically characterized by three parameters: the short-circuit current density J_{sc}, the open-circuit voltage V_{oc} and the geometric fill-factor FF (see fig. 1.1). The latter reflects the deviation of a JV-curve from an ideal, rectangular shape, at which the maximum power $P_{max} = J_{sc} \cdot V_{oc}$ is achieved. For a typical solar cell the open-circuit voltage V_{oc} is in the range $0.5 - 1.0$ eV and the short-circuit current density J_{sc} is $10 - 20$ mA/cm^2. The corresponding charge-carrier

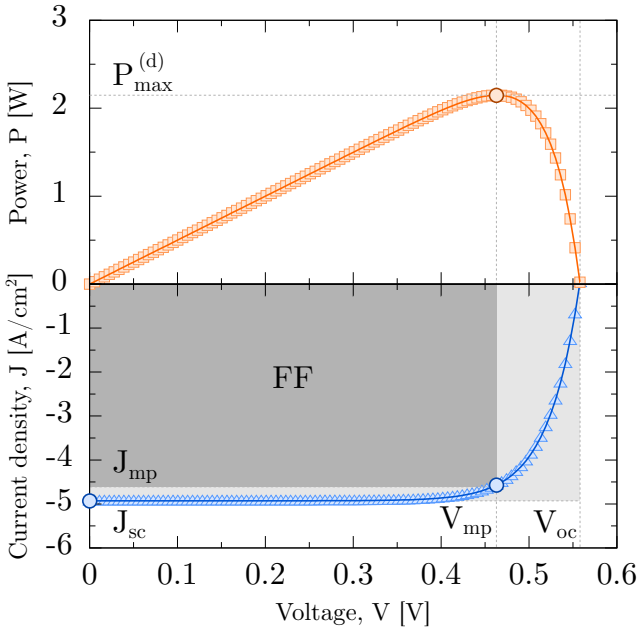

Figure 1.1: Typical JV- and a power curves of a solar cell. Here, J_{sc} is the short-circuit current density, V_{oc} is the open-circuit voltage, $P^{(d)}_{max} = J_{mp}V_{mp}$ is the maximum power the device can produce, J_{mp} and V_{mp} are current density and voltage values that correspond to the maximum power, FF is the fill-factor.

densities in solar cells are low, $n = 10^{16}$ cm^{-3} (ca. 10^{-4} per molecule), as compared to organic light emitting diodes (OLEDs) or organic thin-film transistors (OTFTs) [23]. The solar cell is also characterized by the power conversion efficiency (PCE) η, which defines how much solar radiation a device can convert into an electric current. It is the ratio of the maximum power $P^{(d)}_{max}$, which the device can produce, and the power P_{in} of the incident light

$$\eta = \frac{P^{(d)}_{max}}{P_{in}} = \frac{J_{sc}\, V_{oc}\, FF}{P_{in}}. \tag{1.1}$$

Due to the imperfection of the light-to-photocurrent conversion, which is caused by losses, the theoretical maximum PCE of any single-junction solar cell is less than $\eta = 30\%$ [17]. In order to understand the origin of losses in organic solar cells, one should look at the microscopic processes that take place in the solar cells.

1.2 Processes in solar cells: microscopic view

At the microscopic level, photon-to-current conversion is a multi-step process (see fig. 1.2). An incident photon can create an exciton (a bound electron-hole pair) in the active layer, if the energy of this photon is higher than the band gap of the material, $\hbar\omega > E_g$. Due to weak intermolecular forces, the exciton is strongly localized. It is known as Frenkel exciton and cannot be dissociated into free charges at room temperature. The reason for the stability is a low relative dielectric constant $\epsilon_r = 2 - 4$ within organic materials, which results in binding energies $E_b > 0.3$ eV. A thermal energy $k_BT = 0.025$ eV and typical for solar cells electric fields $E \approx 10^6$ V/m are not enough to overcome such high binding energies. Additionally,

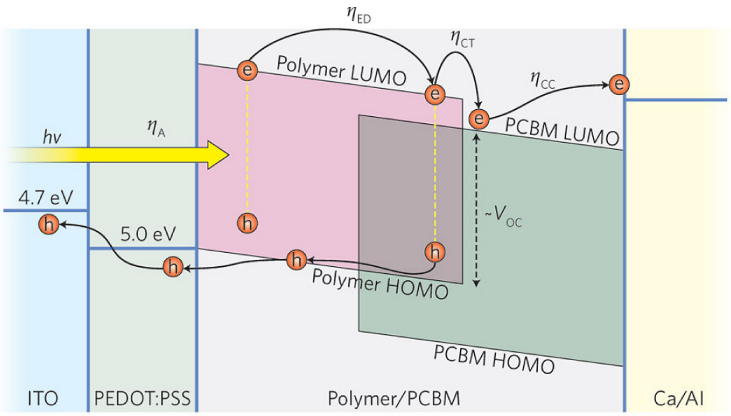

Figure 1.2: Structure and microscopic processes in an organic solar cell. Here, the polymer/PCBM (i.e. donor/acceptor) active layer is sandwiched between two electrodes: ITO/PEDOT:PSS anode and Ca/Al cathode. The parameters η are the probabilities of corresponding microscopic processes, $\hbar\omega$ is the energy of the incident photon, the highest occupied molecular orbital (HOMO) conducts holes (h), the lowest unoccupied molecular orbital (LUMO) conducts electrons (e), V_{oc} is the open circuit voltage. Reprinted by permission from Macmillan Publishers Ltd: Nature Photonics, [11], copyright (2012).

an exciton can recombine due to its finite lifetime. For these reasons, the majority of the generated excitons decay. This was the reason for an extremely low PCE ($\eta < 0.1\%$) in the very first organic solar cells, which had a single-material device architecture (fig. 1.3, a).

As a comparison, this problem does not exist in *in*organic, silicon-based solar cells, where strong covalent bonds and a high relative dielectric constant $\epsilon_r = 12$ lead to delocalized Wannier-Mott excitons with binding energies of the order of $k_B T$. Consequently, in *in*organic solar cells most excitons can be dissociated into free charges.

The problem of exciton recombination can be circumvented by using two materials instead of one in a bi-layer heterojunction device architecture (fig. 1.3, b), which was first proposed by Tang [24]. These materials are typically called donor (D) and acceptor (A), and have different ionization potentials (IP) and electron affinities (EA). If the created exciton diffuses to the DA interface between the two materials, it can be dissociated into free charges due to a HOMO/LUMO offset. At the time, this allowed to improve the efficiency of the cell by an order of magnitude and reach $\eta \approx 1\%$.

Because of their finite lifetimes, excitons can diffuse for short distances of $1 - 10$ nm [25], and so the charge generation takes place only in a small region around the DA interface. Further efficiency improvement can be achieved by introducing the bulk heterojunction architecture (fig. 1.3, c), in which the two materials are intermixed [26]. Matching a typical domain size with an exciton diffusion length (10 nm) helps to create a large-area interface in the vicinity of most excitons, allowing the in-bulk charge generation.

Provided that the majority of excitons can be converted into free charges, one needs to ensure the existence of continuous conducting pathways for both holes and electrons that lead to their respective electrodes. Otherwise, free charges become trapped and eventually recombine, giving no contribution to a photo-current. Creating bulk heterojunction mixtures of donor and acceptor materials with a carefully balanced domain size and connectivity is

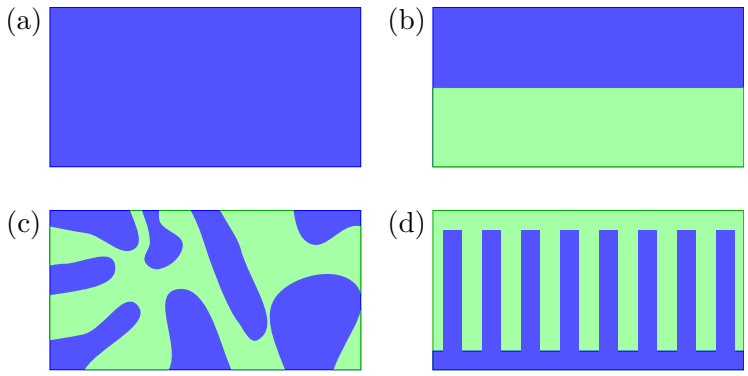

Figure 1.3: Different organic solar cell architectures: (a) single junction, (b) bi-layer heterojunction, (c) bulk heterojunction, (d) ordered bulk heterojunction. The green and blue domains correspond to the donor and acceptor materials respectively.

critical for high PCE solar cells, and, if successful, leads to current record efficiencies of 12% in organic solar cells. This also correlates with an improved exciton dissociation and charge extraction. One can go one step further and imagine an ideal solar cell architecture (fig. 1.3, d), which would combine a high-surface interface and good charge conductivity, known as ordered bulk heterojunction [27, 28].

To recap, in order to convert photons to the photo-current, the following sequence of successful steps is required (see fig. 1.2): Exciton creation from an absorbed photon (η_A), exciton diffusion (η_{ED}), charge separation (η_{CT}), charge diffusion and extraction (η_{CC}). Here, the quantities η_x are the probabilities of the corresponding processes, which are typically far from ideal ($\eta_x < 1$) due to presence of loss mechanisms: Geminate (exciton) and non-geminate (free charge) recombinations. From this perspective one can define another important characteristic for solar cells, the external quantum efficiency (EQE) as

$$EQE(\lambda) = \eta_A(\lambda) \cdot \eta_{ED}(\lambda) \cdot \eta_{CT}(\lambda) \cdot \eta_{CC}(\lambda). \tag{1.2}$$

This quantity shows how many photons in the active layer are converted to charge pairs and extracted into the external electric circuit. It depends on the energy of the photon. In high-performing solar cells it exceeds 80%. The EQE includes not only internal but also optical losses due to other layers having different refractive indexes and absorbed photons that did not lead to exciton creation. The solar cell parameters can be improved as well as losses decreased via a proper choice of the donor and acceptor materials.

Mobility plays an important role in organic solar cells. It has been shown that materials with high charge-carrier mobilities are needed for efficient solar cells [29, 30]. It is a macroscopic parameter that defines how fast charges can move in the external field and is defined by microscale electronic properties, energetics and morphology. Though the functional dependence of carrier mobility on microscopic parameters is unknown, one can track the effects of mobility on the overall solar cell performance in various models. In one of these models [31], optimal mobilities up to 1 cm^2/Vs and band gap values of 1.3 eV are required to achieve the highest possible efficiency, $\eta = 14\%$. Hence, it is important to develop and study materials with high carrier mobilities and small band gaps.

1.3 Polymer materials for solar cells

Among the variety of possible materials one may consider organic molecules as solar cell ingredients. They are made of abundant elements and are easy to process due to weak intermolecular interactions [25]. As acceptor molecules, fullerenes and their derivatives, PCBMs [26, 32], have proven to be highly efficient electron transporting materials due to their high mobilities of $\mu = 10^{-2} - 10^{-1}$ cm^2/Vs. Also, it has been shown that unbalanced transport leads to a charge accumulation, which reduces the efficiency of devices. Hence, one needs organic donor materials that would match the PCBM's mobility and energies, for example conjugated polymers.

The fast electron transfer between a conjugated polymer and a fullerene has been shown already in the 1990s [33, 34], proving that it is possible to use polymers as a donor material in solar cells [26, 35]. Conjugated polymers exhibit good mechanical and opto-electronic properties, where the latter includes efficient absorption and high carrier mobilities. They enable the construction of thin-film (the active layer thickness is on average $80 - 200$ nm), low specific weight, flexible solar cells [9–11, 21, 25, 28, 36]. Also, rich chemical synthesis techniques allow one to tune the relevant parameters, such as bandgap, orbital energies, structure and solubility of these materials. Last, but not least, a variety of processing techniques, for example roll-to-roll printing, allows low-cost, large-area production of polymer/PCBM devices [37, 38]. The well studied polymers for organic solar cells include MDMO-PPV[39], highly crystalline P3HT [40] and low-bandgap PCPDTBT [41].

Because exciton conversion is often inefficient, one can increase the number of excitons that are absorbed by decreasing the band gap of a material. This can be easily done through chemical tuning in a number of ways [42]. For example, it is observed that a HOMO-LUMO difference (fig. 1.2) decreases with the conjugation length. This can be loosely traced back to a particle in the box problem, where the difference between energy levels $\Delta E = C/a$ and a is the characteristic width of the box, C is a dimensional prefactor. Hence, extended conjugated compounds will have lower band gap. Another possibility to effectively modify the gap is to mix electron-donating (donor) and electron-withdrawing (acceptor) building blocks. Indeed, upon combining the two blocks (see fig. 1.4) with different HOMO/LUMO energy levels, one obtains new states with the reduced gap. According to a simple two-state model, the perturbed energy difference E_{DA} is smaller than the individual gaps of donor and acceptor molecules, E_D and E_A. Conjugated polymers successfully combine these two properties and make it easy to create new donor-acceptor compounds, also known as push-pull polymers, with even lower band gap values.

Despite numerous advantages, organic materials, and polymers in particular, have a number of deficiencies. For example, the theoretical efficiency (Shockley-Queisser) limit, is modified if one takes into account the specific nature of organic materials, such as low carrier mobilities and energy penalties for charge-carrier generation [9, 43]. For a single-junction OPV device, the limit remains at the value of 30% in an ideal cell, where EQE$= 1.0$ and FF$= 1.0$ (i.e. ideal absorption and conversion), but reduces to 20% in realistic devices with EQE$= 0.9$ and FF$= 0.7$. The best polymer-based solar cells with similar parameters currently reach only 12% PCE. This is attributed to the drop in the open circuit voltage V$_{oc}$, resulting from energy losses during exciton dissociation.

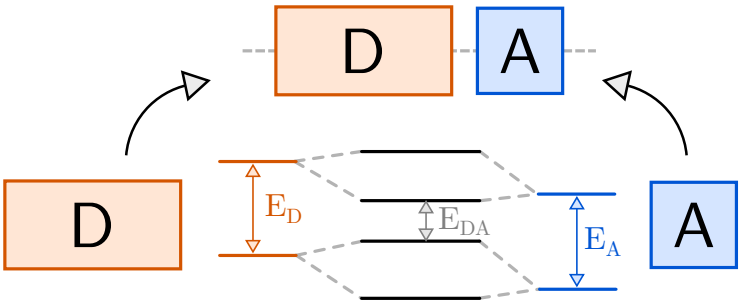

Figure 1.4: Effect of donor-acceptor architecture on a band gap in conjugated polymers. Blocks D and A comprise the chain and have band gaps energies E_D, E_A. Energy E_{DA} is the resulting band gap of the polymer.

Still, though more efficient materials exist for solar cell applications, organic-based devices will always be in demand for large area energy collection due to large scale production techniques, flexibility, low thickness and transparency.

1.4 Further improvements

Up to now only single layer devices were considered. Another way to improve solar cell efficiency is to use two or more active layers with low and high band gap materials, in order to utilize the solar spectrum more efficiently. This OPV device structure is known as a multi-junction or tandem solar cell [11, 44]. However, the corresponding efficiency increase is not linear since properties of multiple cells are competing and need to be optimized (layer thickness, mobilities and more). This can be seen from the Shockley-Queisser limit for tandem OPV devices. In multi-junction cells, for a number of active layers $n = 1, 2, 3$ the theoretical efficiency limits become 37%, 50%, 56%, respectively [45].

In addition to low efficiencies, organic solar cells exhibit short lifetimes due to a low stability. Studies reveal that material's chemistry and electronic structure are altered by the presence of oxygen and water molecules, accumulated during production phase or insufficient isolation. Over time this leads to the creation of additional traps and destruction of conducting pathways [46, 47]. This effectively translates to a decrease in mobility of specific carrier types [48].

1.5 Structure of the thesis

Given the basic understanding of polymer-based solar cells, a problem of linking material chemistry to macroscopic device properties prevails. In particular, in polymers a variety of local and global packing motives, knows as polymorphs, makes the task especially difficult. To understand how chemistry gives rise to numerous morphologies, local opto-electronic properties and overall device efficiency, one can use computer simulations. The rest of this thesis is focused on applying simulation techniques to derive and study various morphologies of common semi-crystalline polymers, as well as their electronic and transport properties in the resulting environments.

In chapter 2, an overview of simulation techniques is given, including quantum chemistry methods, notes on force field development, molecular dynamics simulations and a charge transfer theory. A particular attention is paid to static and dynamic characterization of morphologies using order parameters. These techniques and methods are then applied to two polymer systems.

In chapter 3, the chemistry of PCPDTBT polymer is varied in a systematic way through atom substitution. This results in five derivatives with modified band gap values and in-device performance. To study the trends via simulations, accurate force fields for five polymers are developed from quantum chemical calculations. Through molecular dynamics simulations, various crystalline polymorphs are obtained in a systematic way and verified against the experimental data. Simulated crystals include π-stacked, side-chain mediated and cross-hatched constructions. Key degrees of freedom responsible for the crystal structures are discussed. In π-stacked configurations, hole transport and related quantities, such as site energies and transfer integrals, are investigated in detail using simulated morphologies, first-principles calculations, perturbative energy evaluation methods and Marcus charge transfer theory. As a result, systematic variation of chemistry is linked to observed trends of microscopic properties, such as transfer integral, site energy distributions and mobilities.

In chapter 4, molecular dynamics simulations are combined with solid-state NMR data to study dynamics and macroscopic composition of PBTTT chains in a sample. The initial NMR analysis suggests a *two-mesophase* composition, with a $1{:}1$ ratio of amorphous and crystalline mesophases. However, the experimental data is not resolved with respect to these mesophases. This is done via molecular dynamics simulations. Three morphologies of PBTTT are simulated using an adapted OPLS force field. The local ordering is verified against the structural NMR data. In obtained morphologies, dynamics of chains is addressed via the generalized order parameter. Poor sampling of conformer populations at short simulation times is recognized and overcome within high temperature simulation runs. Structural and dynamical simulated data are then combined with the initial NMR mesophase assessment through an analytical model. With this model, the two-mesophase composition cannot be achieved within the physical range of parameters. Better results are obtained for a refined, *three-mesophase* composition, where the crystalline fraction is no more than 8%. A simple formula with generic parameters is derived to estimate the crystalline fraction in any semi-crystalline polymer with a similar structure.

2 Simulation techniques

In soft matter systems, such as polymer semiconductors, thermal fluctuations play an important role. They emerge from the interplay of a broad range of length- and time-scales in the system and need to be captured in simulations, in order to predict structure, dynamics, and physical properties such as charge mobility. A multiscale approach combines simulations at various levels of theory in order to connect the chemistry of materials to their macroscopic morphologies and transport properties. These methods include first-principles (or quantum chemistry) methods, such as Hartree-Fock (HF) method and density function theory (DFT), which introduce chemistry into the problem. Further, dynamics is introduced via classical molecular dynamics (MD) simulations in order to generate realistic morphologies. These morphologies can then be analyzed through available order parameters. Finally, morphologies are combined with Marcus charge transport theory to simulate charge transport dynamics. In the following sections, related theories, methods and links between them are presented.

2.1 First principles methods

Since it was introduced in the 1920s, quantum theory is routinely used in many research areas, including studies of novel materials for electronics applications. Its goal is to solve the Schrödinger equation [49], which can be written in a stationary form as

$$\hat{H}\left|\psi_\alpha\right\rangle = E_\alpha\left|\psi_\alpha\right\rangle. \tag{2.1}$$

Here the core objects of quantum theory are introduced: the Hamiltonian $\hat{H}$, that defines the system and its properties and the quantized states $|\psi_\alpha\rangle$ (often called wave functions) in which the system can be found. Wave functions correspond to an energy spectrum E_α, where index α represents a set of quantum numbers. The states $|\psi_\alpha\rangle$ form a complete orthonormal basis set (i.e. $\langle\psi_\alpha|\psi_\beta\rangle = \delta_{\alpha\beta}$, where $\delta_{\alpha\beta}$ is the Kronecker delta), that can be used to expand any other state with an arbitrary precision. An important feature of quantum theory is that the spectrum E_α is bound from below, and has the lowest energy E_0 and a corresponding non-degenerate state $|\psi_0\rangle$, called the ground state. For a collection of atoms in a molecule with N_e electrons and N_n nuclei, (without relativistic effects) the Hamiltonian takes the form

$$\hat{H} = \sum_{I=1}^{N_n}\frac{P_I^2}{2M_I} + \sum_{i=1}^{N_e}\frac{p_i^2}{2m_e} + \frac{1}{2}\sum_{I\neq J} k\frac{Z_I Z_J}{|\vec{R}_I - \vec{R}_J|} + \frac{1}{2}\sum_{i\neq j} k\frac{1}{|\vec{r}_i - \vec{r}_j|} + \sum_{i,I} k\frac{Z_I}{|\vec{r}_i - \vec{R}_I|}. \tag{2.2}$$

The first term is the total kinetic energy of the nuclei I with masses M_I, located at positions $\vec{R}_I$ and having charges Z_I. It is followed by the kinetic energy of electrons, labeled with indexes i, carrying masses m_e (identical for all electrons) and located at positions $\vec{r}_i$. The last three terms cover Coulomb interactions between electrons and nuclei and contain the Coulomb constant $k = e^2/4\pi\epsilon_0$ (here ϵ_0 is the permittivity of free space and e is an elementary electric charge). A summation in these terms is carried out over all unique pairs of a given type.

In this form the Schrödinger equation for a molecule is rather complex. Due to correlated motions of particles, the wave function ψ depends on the positions of these particles (i.e. in the position space $\psi = \psi([\vec{r}_i], [\vec{R}_I])$ and is many-body in nature. Here, the notation $[\vec{r}_i]$ is a short-hand notation for $(\vec{r}_1, \ldots, \vec{r}_N)$. One needs to simplify (eq. 2.1) in order to solve it.

2.1.1 Solving the molecular Schrödinger equation

Several approximations are typically used to reduce the complexity of the Schrödinger equation (eq. 2.1) of a molecule. First, one applies a Born-Oppenheimer ansatz (also known as adiabatic approximation) to separate fast and slow degrees of freedom (DOF), i.e. electrons and nuclei. This is motivated by the separation of relaxation times of these DOFs, which is justified in most cases and allows to treat nuclei as a static background during the electron dynamics (or, vice versa, electrons are always found in a particular state for a given nuclear geometry). One can then write the Schrödinger equation for the electronic sub-system as $\hat{H}_{el}\psi_\alpha(\{\vec{R}_I\}) = E_\alpha\psi_\alpha(\{\vec{R}_I\})$, where the Hamiltonian with its states and energies depends on the nuclear positions parametrically

$$\hat{H}_{el} = \sum_{i=1}^{N_e} \frac{p_i^2}{2m_e} + \frac{1}{2}\sum_{i\neq j} k\frac{1}{|\vec{r}_i - \vec{r}_j|} + \sum_{i,I} k\frac{Z_I}{|\vec{r}_i - \vec{R}_I|}. \tag{2.3}$$

The ground state energies $E_0([\vec{R}_I])$, calculated for all nuclear positions $\vec{R}_I$ define the potential energy surface (PES) in which the nuclei are moving. Minima of the PES define equilibrium geometries for a given molecule.

However, after the adiabatic approximation is employed, equation (eq. 2.3) still cannot be solved analytically for the vast majority of molecular systems, and should be solved numerically. To this end, one can project the electronic wave-functions on a complete basis set of orthonormal, continuous functions ϕ_i, so that $\psi([\vec{R}_I]) = \sum_i C_i\phi_i([\vec{R}_I])$. Following the variational principle, this transforms the Schrödinger equation into the eigenvalue problem

$$HC = CE, \tag{2.4}$$

which can be solved via numerical eigensolvers. Here, matrix H is the Hamiltonian of a system in a representation of the basis ϕ_i and is known, while C contains expansion coefficients for eigenstates of the system and E carries the corresponding state energies (which are found through a diagonalization procedure). One should note that, in practice, basis sets are neither complete, nor orthogonal. For finite, N-dimensional, non-orthogonal

basis sets (i.e. $\langle\phi_k|\phi_l\rangle = S_{kl} \neq \delta_{kl}$, where S_{kl} is the overlap matrix), a generalized eigenvalue problem emerges

$$HC = SCE. \tag{2.5}$$

It can be converted to a regular eigenvalue problem (as in eq. 2.4) by means of unitary transformation U (for example, $U = S^{-1/2}$, as was proposed by Löwdin [50]) and then solved, though at a higher computational cost. The resulting energies and states are the best approximations to their true values of a system for a given incomplete basis set ϕ_i.

2.1.2 Hartree-Fock method

The first attempt to solve the many-body Schrödinger equation for molecular systems dates back to Hartree and Fock, who derived a self-consistent method bearing their names (HF). To solve the Schrödinger equation, one needs to deal with the many-body wave function $\psi(\vec{r}_i)$, which is tedious. In the HF method, the wave function is approximated by the anti-symmetric product of single-particle states (the Hartree product) in order to decrease the number of DOFs. As a result, non-interacting, single-particle states are found in an external mean-field potential, generated by other electrons. The equivalent of the Hamiltonian is a single-particle Fock operator

$$\hat{f}_i^{HF} = -\frac{1}{2}\nabla_i^2 - \sum_J^{N_n} \frac{Z_J}{r_{iJ}} + V_i^{HF}(j), \tag{2.6}$$

which acts on the i-th electron. Here, atomic units are used. In addition to kinetic energy and electron-nuclear attraction, a HF potential is introduced, which includes the classical Coulomb J_{ij} and exchange K_{ij} integrals. They are, in general, eight dimensional two-electron integrals of the form

$$[ij|kl] = \int d\vec{x}_1 d\vec{x}_2 \; \phi_i(\vec{x}_1)^* \phi_j(\vec{x}_1) \frac{1}{r_{12}} \phi_k(\vec{x}_2)^* \phi_l(\vec{x}_2), \tag{2.7}$$

where $\phi_i(\vec{x}_j)$ are eigenfunctions of the Fock operator (eq. 2.6), often called the spin orbitals. Because the HF potential depends on single-particle states, the equation should be solved self-consistently, starting from an initial guess. Though the method allows to solve a molecular Hamiltonian (eq. 2.3), it is a mean-field approximation with a number of deficiencies. Despite an exact treatment of the exchange (which stems from the Pauli exclusion principle), it ignores some correlations. This leads to overestimation of predicted HF values from experimental results (a classical example is a positive electron affinity energy upon adding the $(N+1)$-st electron). Also the computation time of the HF method scales as $O(N_{orb}^4)$ with the number of orbitals N_{orb}. This is due to four-center integral calculations (eq. 2.7) which are proved to be the bottleneck of the method. One can correct for these errors using post-HF wavefunction-based methods (such as CI [51], MPn [52], CC [53] and more) at a cost of less favorable scaling $O(N_{orb}^k)$, where $k \geq 5$. At this point it is natural to ask if it is

possible to derive molecular properties in a simpler way, using a more intuitive object, such as the total electron density.

2.1.3 Density functional theory

An alternative to wavefunction-based methods is density functional theory (DFT). It operates not with wave-functions of the Hamiltonian operator, but with a total electron density $\rho(\vec{r})$, which has only three spatial coordinates and, therefore, is much easier to treat. Its basic property is that the integral over the electron density gives the total number of electrons in the system: $\int \rho(\vec{r})d\vec{r} = N_e$, where integration is performed over entire space. However, the electron density $\rho(\vec{r})$ can be also used to calculate other physical properties, for example energies.

The foundation of the DFT method relies on two theorems proved by Hohenberg and Kohn [54]. The first, "existence" theorem, says that there is a unique map between the Hamiltonian of a system $\hat{H}$ and its ground-state electron density $\rho(\vec{r})$, though it does not provide a recipe on how to construct such a map. Further, through the Hamiltonian, the electron density is linked to the ground and excited properties of a system. The second, "variational" theorem shows that, similarly to wave-functions, the density obeys the variational principle. This means that the true electron density of the system $\rho(\vec{r})$ will have the lowest, ground state energy E_0. In this form, the energy of a system $E[\rho]$ is a functional of the electron density, which needs to be minimized.

One may hope to use electron density only and skip the need to solve the molecular Schrödinger equation, in order to derive physical properties of a system. Unfortunately, this cannot be realized in practice, since one needs to know the functional dependence on the density $\rho(\vec{r})$ for observables of interest. This turns out to be problematic already for such a basic observable as the total energy of a system. Though it is proven that the exact energy functional exists, its analytical form is unknown. A solution to this problem is to introduce a single-particle representation [54], i.e $\rho(\vec{r}) = \sum_i^{N_e} \langle\psi_i|\psi_i\rangle$. This results in a single-particle-based energy functional

$$E_{DFT}[\rho] = T_s[\rho] + V_{ne}[\rho] + V_{ee}[\rho] + E_{xc}[\rho], \tag{2.8}$$

where an additional, exchange-correlation energy term E_{xc} was introduced to compensate for errors due to a single-particle kinetic energy T_s and non-classical corrections to the electron-electron repulsion energy V_{ee}. One should note that E_{xc} is unknown and is defined by (eq. 2.8). In practice it is obtained by minimizing the difference between the DFT and true observables for various systems, which are obtained from experiments or precise, wavefunction-based calculations. Through the variational principle one derives Kohn-Sham equations that minimize the energy of the system (i.e. $\hat{h}_i^{ks}\psi_i = \epsilon_i\psi_i$), where $\hat{h}_i^{ks}$ is the Kohn-Sham (KS) one-electron operator

$$\hat{h}_i^{ks} = -\frac{1}{2}\nabla_i^2 - \sum_J^{N_n} \frac{Z_J}{|\vec{r}_i - \vec{R}_J|} + \int \frac{\rho(\vec{r}\,')}{|\vec{r}_i - \vec{r}\,'|} d\vec{r}\,' + V_{xc}(\vec{r}_i), \tag{2.9}$$

where the exchange-correlation potential is defined as variational derivative $V_{xc} = \delta E_{xc}/\delta\rho$. The KS operator has a structure identical to a Hartree-Fock operator $\hat{f}_i^{HF}$. This allows to solve (eq. 2.9) using the same techniques as in the HF method, which include the SCF procedure. The resulting states ψ_i are the Kohn-Shan orbitals of non-interacting electrons, with a total electron density, identical to the density of an interacting electron system.

In practice, due to similarities between the HF and KS equations, similar SCF work-flows are employed. Unlike the HF method, the computation time of the DFT is defined not by the number of integral evaluations, but by the scaling of the diagonalization routines, which is close to $O(N_{orb}^3)$. However, to obtain good results from DFT calculations, hybrid exchange-correlation functionals are often used. They contain terms with the exact exchange energy, as introduced in the HF method, and require four-center integral evaluations. Consequently, the $O(N_{orb}^4)$ scaling is re-introduced. Also, the scaling prefactor is higher than for the HF method, since integrals over some correlation potentials in the KS equations are not analytical and should be evaluated numerically. But, in the end, DFT provides a much higher accuracy of the results than the HF method, which makes it more cost-effective.

The key difference between the HF and the DFT theories is that HF is a mean-field approximation and DFT is in principle exact. But, since the functional dependence of the E_{xc} operator on density $\rho(\vec{r})$ is unknown, it has to be replaced with an adequate approximation. Once the E_{xc} approximation is adopted, the method can produce energies that are lower than the true values (though by a small fraction). One should remember that KS and HF orbitals are not the same. The KS orbitals do not have a phase, as the true wave-functions do. This reflects the fact that they are merely a mathematical basis for an expansion of the total electron density of the system. In practice, the KS orbitals are extremely similar to the HF states [55] and are often used for analysis or further calculations, such as transfer integral evaluations, Green-function-based calculations and more.

One can judge the complexity of a general $E_{xc}[\rho]$ energy by the number of existing parameterizations, which stem from different employed functional forms and reference data. Some of these functionals perform better than the others and are regularly used for a variety of molecular systems.

Hybrid functionals

A number of robust functionals is derived using the adiabatic connection method [56] (ACM), based on the Hellmann-Feynman theorem. In the spirit of Kohn and Sham, if one does not know the exact E_{xc} energy, one can interpolate it between several known, limiting cases. This was successfully done by Becke and Stevens in a three-parametric B3LYP functional [57, 58], where the LSDA[59] and the HF exchange energies are mixed and further corrected by Becke's GGA exchange, while the LSDA correlation energy is mixed with the pure correlation LYP functional [60]. It is written as

$$E_{xc}^{B3LYP} = (1-a)E_x^{LSDA} + aE_x^{HF} + b\Delta E_x^{B88} + (1-c)E_c^{LSDA} + cE_c^{LYP}. \qquad (2.10)$$

Here the HF exchange E_x^{HF} is calculated using KS orbitals and parameters a, b, c take values 0.20, 0.72, 0.81, respectively. As suggested by the ACM method, the HF and the DFT components here are mixed into a hybrid, and so the obtained functionals are referred to as hybrid functionals. B3LYP is a widely used functional and gives accurate results for a variety of systems, including organic molecules. Further extensions, which use more fitting parameters give mild improvements at best and demonstrate the robustness of the derived B3LYP parameterization.

Basis sets

One introduces basis set functions to allow analytical evaluation of multi-dimensional integrals. Analytical integrals are then computed rapidly and on the fly. For periodic systems, such as crystals, plain waves is a typical choice, while for isolated molecules a linear combination of Gaussian functions is employed. The most common classification of these basis sets was introduced by John Pople and is known as split-valence basis sets.

As an example, let us consider a at 6-311++g(d,p) basis set. Within this basis set, six primitive Gaussians represent each core atomic basis function. The remaining valence orbitals are expanded over three basis functions, containing three, one and one primitive Gaussian function. Multiple primitive Gaussians combined into one orbital are often called a contracted Gaussian function. For higher precision calculations one additionally uses diffuse (++) and polarization (d,p) functions. Some times these functions must be discarded as they cause convergence problems, when the Hamiltonian is diagonalized.

2.1.4 Limitations of first-principles methods

Already for fixed-geometry single-molecule calculations, both Hartree-Fock and DFT methods can be computationally demanding. However, in systems like partially disordered polymer semiconductors, dynamics and ordering play an important role. And, though it is possible to carry out the first-principles molecular dynamics simulations, these methods become not feasible for realistic morphology sizes and simulation times. A drastic simplification can be done, if one assumes that molecules always remain in the ground state and their nuclei are moving in the averaged field of surrounding electrons (PES). Using appropriate effective potentials, one can propagate nuclei classically, hence, significantly reduce the computation time and enable studies of realistic morphologies.

2.2 Molecular dynamics simulations

In order to obtain a meaningful insight into physics of organic semiconductors, large systems sizes and long simulation runs are needed. Such requirements cannot be fulfilled with the first-principles methods due to their high computation cost and unfavorable scaling. Hence, one makes further approximations, which allow to overcome these limitations, and arrives at the idea of classical molecular dynamics simulations.

Molecular dynamics (MD) is a simulation technique, which allows one to compute equilibrium and transport properties of classical systems [61, 62] (i.e. systems, in which particle dynamics is governed by classical, Newtonian equations of motion). In fact, a large number of material properties can be studied within a classical approximation. The first simulations were performed already in the 1950s [63, 64], and, since then, major hardware and algorithm improvements have been achieved. At present, MD simulations are widely used in many areas of material science, which include studies of solids, nano-structures, proteins, small molecules, polymers and more. One distinguishes between two types of MD simulations: ab initio (AIMD) and classical (MD) molecular dynamics. In the ab initio MD (i.e. Born-Oppenheimer and extended Lagrangian methods, such as Car-Parinello MD [65, 66]), one treats electrons of each molecule explicitly and solves the corresponding Schrödinger equation for every time step. The resulting electron densities are then used to calculate forces, which are used to propagate the nuclei. This approach, in principle, does not rely on parameterizations, and hence is universally transferable (i.e. the results are valid at each point of the phase diagram). It is a method of choice to observe quantum-related processes, like bond cleavage and chemical reactions [67, 68], binding and adsorption [69], non-adiabatic charge transfer effects and more.

Though it is more precise, AIMD simulations are computationally expensive and not applicable to large systems for sufficiently long times. Luckily, for a broad range of problems, the nature of chemical bonds is of minor importance, and their explicit quantum treatment is unnecessary. One can assume that molecules remain in their ground states at all times, and parametrize their potential energy surface (PES) with a linear combination of analytical functions. By doing so, one arrives at a concept of classical MD force field.

2.2.1 Force fields

In molecular dynamics, molecules are treated as a collection of N classical particles, often called atoms, which are centered at the nuclei and interact via classical inter-atomic forces. One is forced to introduce atom types, as the same chemical element may have different chemical environments and interactions with other atoms within a molecule. Consequently, the number of atom types is much larger than the number of chemical elements.

The inter-atomic forces are determined by a position-based potential $U(\vec{r}_1, \ldots, \vec{r}_i, \ldots, \vec{r}_N)$, where $\vec{r}_i$ is a instantaneous position of the i-th atom. The force acting on atom i is calculated as

$$\vec{F}_i = -\nabla_{\vec{r}_i} U([\vec{r}_i]) \tag{2.11}$$

where $\nabla_{\vec{r}_i} = \partial/\partial\vec{r}_i$ is the nabla operator and $[\vec{r}_i]$ stands for a collection of all atom positions in a compound. The inter-atomic potential $U([\vec{r}_i])$ results from interactions between electrons and nuclei, and is a classical approximation to the first-principles PES, justified by the Born-Oppenheimer approximation and fitted to ab initio and/or experimental data. A specific implementation of the potential energy $U([\vec{r}_i])$, combined with its fitted parameters, is often referred to as a force field.

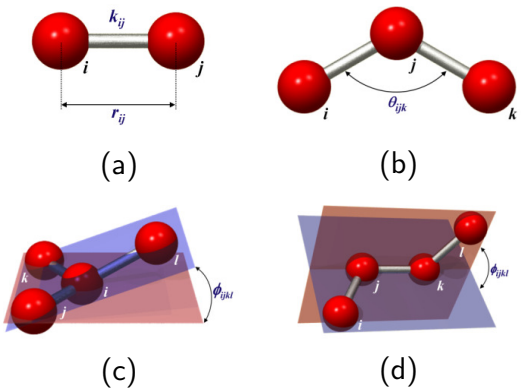

Figure 2.1: Visualization of bonded potentials, used in a force field: (a) bond, (b) angle, (c) improper, (d) dihedral potentials (the figure is obtained from Pumma MD webpage [70]).

Force fields usually follow an intuitive *ball*-and-*stick* picture, which introduces concepts of bonds, angles, impropers and dihedrals (see fig. 2.1). These potentials are covalent and short-range in nature, and are often referred to as *bonded* interactions $U_B([\vec{r}_i])$, as they define an internal structure of a molecule. Additionally, one needs *non-bonded* potentials $U_{NB}([\vec{r}_i])$, which provide inter-molecular interactions. Combined, these two groups of potentials constitute the force field of a molecule and can be written as

$$U([\vec{r}_i]) = U_B([\vec{r}_i]) + U_{NB}([\vec{r}_i]), \tag{2.12}$$

where each term will be explained in detail in the following sections.

Bonded interactions

The bonded part of a force field can be represented in the following functional form

$$U_B = \sum_{i=1}^{N_b} \frac{k_i^{(b)}}{2}(x_i - x_i^{(0)})^2 + \sum_{i=1}^{N_a} \frac{k_i^{(a)}}{2}(\theta_i - \theta_i^{(0)})^2 + \sum_{i=1}^{N_i} \frac{k_i^{(i)}}{2}(\psi_i - \psi_i^{(0)})^2 + \sum_{i=1}^{N_d} V^{(i)}(\phi_i) \tag{2.13}$$

The four terms correspond to interactions due to bonds, angles, impropers and dihedrals, respectively (see fig. 2.1). Improper dihedrals are often presented as a separate group due to the presence of out-of-plane bending motions in a molecule [71]. Here, N_b, N_a, N_d, N_i are the numbers of bonds, angles, impropers and dihedrals in a molecule. Spring constants $k_i^{(b)}$, $k_i^{(a)}$, $k_i^{(i)}$ for bonds, angles and impropers can be unique for each degree of freedom, though in practice one introduces identical interaction parameters between the same atom types (for example, between two carbon atoms in the alkyl chain). Each bond is defined by a pair of values: The instantaneous displacement x_i and its equilibrium value $x_i^{(0)}$. Similarly, angles and impropers are defined by the pairs $(\theta_i, \theta_i^{(0)})$ and $(\psi_i, \psi_i^{(0)})$, respectively. While it is justified to use a harmonic (and therefore non-periodic) approximation for stiff bond, angle and improper potentials, this is not sufficient for the proper degrees of freedom. Torsional

potentials are periodic and, hence, need to be expanded in periodic basis functions, i.e. the Fourier series, as

$$V(\phi) = \sum_{n=0}^{K} C_n \cos(n\phi - \phi_0^{(n)}), \tag{2.14}$$

where C_n, $\phi_0^{(n)}$ are the coefficients of the expansion, upper bound K is a cut-off of the expansion dictated by a desired precision of the fit, and the total number of fitted parameters is $2K$.

The dihedral potentials are soft, and their profiles are defined by the electronic structure and local symmetry of molecular fragments. In case of simple molecules, dihedrals are well represented by a single term potential, which is used in AMBER force field

$$V_p(\phi) = C_0 \left[1 + \cos(n\phi - \phi_0)\right]. \tag{2.15}$$

This function generates a potential with n minima and contains two parameters: Position of the first minimum ϕ_0/n and equal barrier height $C_0/2$. For potentials with multiple minima and barrier heights, the following six-term Ryckaert-Bellemans potential suits better

$$V_{rb}(\phi) = \sum_{n=0}^{5} (-1)^n C_n \cos^n(\phi). \tag{2.16}$$

It is symmetric with respect to the origin, $\phi = 0$. For even more complex organic molecules, typically used in organic electronics devices, a more sophisticated Fourier expansion with a larger cut-off may be needed to reproduce complex energy profiles, as in (eq. 2.14).

Non-bonded interactions

The non-bonded section of a force field represents long-range interactions between two molecules and is often factorized into two parts

$$U_{NB}([\vec{r}_i]) = U_{vdw}([\vec{r}_i]) + U_{Pauli}([\vec{r}_i]) + U_{Coulomb}([\vec{r}_i]). \tag{2.17}$$

Here, the terms are van der Waals, Pauli and Coulomb potentials, respectively. The van der Waals term, also known as London dispersion forces, is the long-range attraction due to induced dipole-dipole interactions. It depends on the inter-atomic distance as r^{-6}. The short-range repulsion part, often called the Pauli repulsion, is due to quantum mechanical exchange interactions, and is responsible for the excluded volume of molecules. Combined,

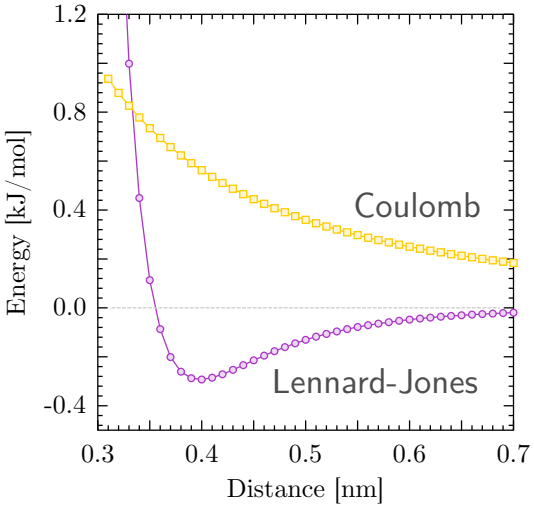

Figure 2.2: Non-bonded potentials, used in molecular dynamics simulations: Lennar-Jones and Coulomb.

van der Waals and Pauli interactions are often modeled by the Lennard-Jones potential (also called the 6-12 potential), written as

$$U_{LJ}(r_{ij}) = \frac{1}{2}\sum_{i \neq j} 4\epsilon_{ij}\left[\left(\frac{\sigma_{ij}}{r_{ij}}\right)^{6} - \left(\frac{\sigma_{ij}}{r_{ij}}\right)^{12}\right] f_{ij}, \tag{2.18}$$

which includes inter-atomic distances $r_{ij} = |\vec{r}_i - \vec{r}_j|$ between atoms i and j and parameters ϵ_{ij} and σ_{ij}, that define a potential's unique minimum and its distance from the center of an atom. While the attractive part is physical, the repulsive part is not. Prefactor f_{ij} is a damping factor, which modifies short-range interactions within a molecule. It is force field specific and will be defined in the section below. Indices i, j in the sum go through all pairs of atoms (of all molecules) in a system.

Third term represents electrostatic interactions introduced via atomic partial charges q_i, centered at the atoms' nuclei. The resulting Coulomb energy is

$$U_{Coulomb}(r_{ij}) = \frac{1}{2}\sum_{i \neq j} k\frac{q_i q_j}{r_{ij}} f_{ij} \tag{2.19}$$

where $k = 1/4\pi\epsilon_0\epsilon_r$ is the electrostatic constant, that includes screening effects by means of relative dielectric constant ϵ_r, greater than one. Indices i, j and prefactor f_{ij} carry the same function as in the van der Waals potential. The introduced van der Waals and Coulomb potentials are shown in fig. 2.2. They are routinely used in molecular dynamics and other simulations.

On the final note, combined bonded and non-bonded potentials themselves represent two-, three- and (partly) four-body contributions of the expansion of a many-body PES, which can be written as

$$U([\vec{r}_i]) = \sum_{i,j} U_2(\vec{r}_i, \vec{r}_j) + \sum_{i,j,k} U_3(\vec{r}_i, \vec{r}_j, \vec{r}_k) + \sum_{i,j,l} U_4(\vec{r}_i, \vec{r}_j, \vec{r}_k, \vec{r}_l) + \ldots, \tag{2.20}$$

where higher order terms are neglected.

OPLS-AA force field specification

OPLS is an all-atom force field for simulations of protein-ligand interactions [72, 73], including small aromatic heterocycles [74, 75]. Therefore, it is a good starting point for building force fields for new compounds, such as conjugated, semi-crystalline polymers.

The OPLS force field parameters are transferable, i.e. force fields of larger compounds can be assembled from smaller building blocks. It aims to reproduce conformational energetics and liquid-phase properties, while keeping the number of parameters at a minimum. More importantly, the Lennard-Jones parameters in the force field are found to be highly transferable (for example, all aromatic carbons have the same parameter values), as opposed to partial charges, which are often compound specific.

The functional form of the force field follows a general structure, outlined previously (see eq. 2.12). The OPLS force field does not contain improper dihedrals, since in the original parametrization scheme the out-of-plane motions were excluded (molecules were restrained to planar geometries [74]), and torsional potentials are fitted by the Ryckaert-Bellemans functional form. Values of bonds and angles are obtained from equilibrium geometries, optimized at the HF level of theory using localized 6-31G* Pople's split-valence basis set. The force constants for these potentials are adopted from similar interactions in the AMBER force field by Kollman and coworkers [76], which in turn are based on experimental data (i.e. X-ray and vibrational frequencies). Since, originally, geometries of heterocycles were restrained to a plane, dihedral potentials were not employed as well.

For conjugated molecules, partial charges (and atom types) are difficult to classify due to the presence of delocalized electron states (π-orbitals), and should be re-calculated individually for new compounds. In the OPLS force field, partial charges are obtained from fitting the ground state electron density to the electrostatic potential using CHELPG procedue [77]. Resulting molecular dipole moments are often overestimated due to lack of polarization and poor performance of point charge in the case of out-of-plane electrostatics in conjugated molecules. The van der Waals parameters were found to be highly transferable and, therefore, were adopted from earlier OPLS parametrizations [74] and extended to hetero-interactions via the "geometrical" mixing rules

$$\sigma_{ij} = (\sigma_{ii} \cdot \sigma_{jj})^{1/2}, \ \epsilon_{ij} = (\epsilon_{ii} \cdot \epsilon_{jj})^{1/2}, \tag{2.21}$$

as oposed to the Lorentz-Bertelot mixing rules

$$\sigma_{ij} = \frac{1}{2}\left(\sigma_{ii} + \sigma_{jj}\right), \; \epsilon_{ij} = \left(\epsilon_{ii} \cdot \epsilon_{jj}\right)^{1/2}, \tag{2.22}$$

which are used in the above mentioned AMBER force field [76]. Here σ_{ii} and ϵ_{ii} are the self-interaction van der Waals parameters.

Finally, all non-bonded interactions in the OPLS force field make use of the fudge factor f_{ij} definded as

$$f_{ij} = \begin{cases} 0, & \text{interactions } 1-2, 1-3 \\ \frac{1}{2}, & \text{interactions } 1-4 \\ 1, & \text{interactions } 1-n, \text{where } n > 4. \end{cases} \tag{2.23}$$

This re-scaling is introduced to remove the unphysically high van der Waals repulsion between the nearest atoms within a molecule, though the 1-4 scaling is arbitrary and force field specific.

The main focus of the OPLS force field is on interactions between molecules. The intra-molecular interactions are optimized using single point calculations (at the same level of theory) using molecule-molecule and molecule-water dimer complexes in vacuum with lowest energy geometries.

OPLS refinement

It was mentioned previously, that new conjugated compounds require individual force field development. To this end, one employs the OPLS force field as a reference and follows a modified parameterization procedure.

The initially used HF method is replaced with a better performing DFT. In it, the B3LYP density functional is combined with 6-311+G(d,p) basis set to obtain equilibrium geometries and partial charges. Because CHELPG procedure overestimates charges on heavy atoms, it is replaced with Merz-Kollman procedure[78], which otherwise produces similar results [79–81]. Other parameters, like spring constants and transferable van der Waals parameters are adopted from the original OPLS-AA force field potentials with similar interactions.

Additionally, out-of-plane (improper) and torsional degrees of freedom are re-introduced. The harmonic approximation is used for stiff improper potentials, as it is done for bond and angle DOFs. Contrary to impropers, dihedral potentials are sensitive to molecule's local electronic structure and symmetry. Especially in conjugated compounds, dihedral energy profiles may deviate significantly (not only quantitatively, but also qualitatively) from profiles generated by classical Coulomb and van der Waals interactions. To account for

this mismatch, one parametrizes the difference between QM and MD potentials along the reaction coordinate as

$$\Delta U(x) = U_{QM}(x) - U_{MD}(x|\ C_i = 0). \tag{2.24}$$

Here $U_{QM}(x)$ is the energy profile obtained from ab initio, single point calculations, performed on a relaxed geometry, restrained to the reaction coordinate (x), and $U_{MD}(x|\ C_i = 0)$ is a classical potential energy surface under identical conditions in the absence of parametrization. One example of a reaction coordinate would be a dihedral angle. The remaining dihedrals, if present, are restrained to one of their equilibrium values. The resulting energy difference $\Delta U(x)$, parametrized in a given functional form, is then added to the MD potential in order to reproduce the ab initio potential energy surface in MD simulations. One should note, that some dihedral profiles can be asymmetric and, thus, require a truncated Fourier expansion (eq. 2.14), as compared to simplified and symmetric AMBER and Ryckaert-Bellemans functional forms.

Force field validation

If parameterized correctly, the force field should reproduce structural and thermodynamic properties of a system. For example the OPLS force field is capable of producing reasonable densities and radial distribution functions, as well as heat capacities, free energies of solution and heats of vaporization of various organic liquids, which are in a good agreement with the reference experimental data [74, 75]. For proteins, Ramachandran plots of dihedral angles are used to ensure correct sampling, while in polymer melts, one is interested in the radii of gyration and persistent lengths.

Though new force fields may not reproduce thermodynamic properties of new compounds correctly (since parametrization in vacuum excludes solute-solute and solute-solvent effects), the structural properties, which are dominated by the van der Waals interactions in conjugated polymers (i.e. densities, π-stacking and inter-lamellar distances, unit cell parameters of crystalline polymers), are expected to be well reproduced due to transferability of the Lennard-Jones parameters of the OPLS force field.

Polarizable force fields

Due to their simplicity, the presented above force fields have two major deficiencies. Local charge densities are not spherically symmetric, hence, the point charge representation of the electrostatic potential may not be accurate. Even in cases, where the point charge description is adequate, the parameterization is valid only in a small region of the phase space, i.e. the force fields is not transferable. Also, molecule's electron density is constantly modified by changes in nuclear degrees of freedom, as well as changes in the environment [82]. The two issues play an important role in protein-ligand binding [83], charge transfer dynamics

[84] and more, and can be treated via a number of extensions of the classical point charge models, though at a cost of higher complexity and longer computational times.

One can introduce the polarization effects to the model through the fluctuating charges, the Drude oscillators or polarizable multipoles. The first model is the fluctuating charge model [85, 86], in which partial charges are supplied with masses and treated as additional degrees of freedom with their own equations of motion. The charges are then allowed to flow between the molecules until the instantaneous electronegativity is equalized. The benefit of this approach is that interactions between charges are still described via Coulomb potentials, which makes it equivalent to the classical force field model. On the other hand, the model inherits the problem of static charges and cannot treat out-of-plane electrostatics and polarization.

The second model is the Drude oscillator model [87, 88], where each atom is supplied with a pair of charges, one of which is fixed at the site. The other charge is attached to the site with a spring and is mobile, giving rise to induced dipole moments. The two charges represent a nucleus and a local electron density, their magnitudes remain constant during simulation runs. The atomic polarizability is then given as $\alpha = q^2/k$, where q is the charge of a Drude particle and k is the spring constant. The disadvantage of the method comes from an increased number of coulomb interactions, that need to be evaluated, since evaluation of non-bonded interactions is the most expensive part of MD simulations.

The third approach involves inducible dipoles added to cites with fixed partial charges [82, 89]. This approach is similar to the Drude model, but interaction types are extended and include charge-dipole and dipole-dipole interactions, which require additional effort in terms of implementation and longer computational times.

Another issue is representation of molecules' permanent electrostatics. The Coulomb interactions between molecules are treated via point charges q_i, that are localized at atomic nuclei. As a result, electrostatics of individual atoms is isotropic. One example, where the models fails, is force fields of conjugated molecules, with point charges located within the plain of a molecule and unable to reproduce quadrupole-like electrostatics, originating from the π-orbitals of these molecules. Other issues include lone pairs, π-clouds and σ-holes [90]. To introduce a local anisotropy, a better expansion of electron density is required. This can be achieved, for example, via introducing auxiliary, off-center point charges [91].

A more theoretically robust solution, however, is to employ multipole moments (such as dipoles and quadrupoles) [82]. Due to lower symmetry, multipoles reproduce all of the above-mentioned effects and, thus, circumvent the need for auxiliary charges. The AMOEBA force field [83] is a widely used implementation of this approach and includes static moments up to quadrupoles and polarizable dipoles, located at atom sites. Further, sites are collected into groups, which represent molecular fragments. Static moments within the group can induce moments belonging to other groups, but self-induction is not allowed. In this way, large molecules can be built from small parametrized fragments, following the force field modularity principle. Another consequence of the model is capability of atoms to adjust to their environment, which effectively reduces the number of atom types needed for various compounds (but does not eliminate them completely). Results, generated with the AMOEBA force field, are in good agreement with experiments in both gas and liquid phases, including

binding and solvation energies, static and dynamic properties of small molecules. Such diversity makes this force field transferable, a result that is impossible for point-charge-based force fields. The flexibility, as was mentioned previously, comes at a higher computational cost due to an increased number and complexity of interactions.

The main difference of the method comes from replacement of fixed point charges with polarizable multipoles up to quadrupole moments, which are parameterized against gas phase experimental data or high-level quantum chemistry calculations (i.e. electron density decomposition). The permanent atomic multipoles are described by a vector

$$M_i = \left(q_i, \mu_i^{(x)}, \mu_i^{(y)}, \mu_i^{(z)}, Q_i^{(xx)}, \dots, Q_i^{(zz)}, \dots\right), \tag{2.25}$$

where q_i is a monopole, $\vec{\mu}_i$ is a dipole vector and $\hat{Q}_i$ is a quadrupole tensor in cartesian representation, defined in a local molecular frame at a site i. Tensor $\hat{Q}$ is traceless: $\mathrm{Tr}(\hat{Q}) = 0$. The interaction between sites i and j is mediated by the potential $U^{(p)}_{Coulomb,\ ij} = \vec{M}_i^{\dagger}\hat{T}_{ij}\vec{M}_j$, where label (p) stands for permanent. The $\hat{T}$-tensor in this notation is defined as

$$T_{ij} = \begin{bmatrix} 1 & \partial_{x_j} & \partial_{y_j} & \partial_{z_j} & \dots \\ \partial_{x_i} & \partial_{x_i x_j} & \partial_{x_i y_j} & \partial_{x_i z_j} & \dots \\ \partial_{y_i} & \partial_{y_i x_j} & \partial_{y_i y_j} & \partial_{y_i z_j} & \dots \\ \partial_{z_i} & \partial_{z_i x_j} & \partial_{z_i y_j} & \partial_{z_i z_j} & \dots \\ \dots & \dots & \dots & \dots & \dots \end{bmatrix} \left(\frac{1}{r_{ij}}\right), \tag{2.26}$$

where $\partial_{x_i} = \frac{\partial}{\partial x_i}$ is a partial derivative, the total multipole energy is invariant under permutation of two multipole sites.

Electronic polarizability accounts for a distortion of electron density in the presence of an external field. Apart from dispersion and repulsion interactions, it is a defining many-body contribution in clusters and condensed phases. In a polarizable force field, each site can be supplied with a polarizable multipoles, though in most calculations polarizable dipoles only are used. The polarization is calculated via the self-consistent Thole's damped induction model [92] and employs distributed polarizabilities. In this model, a short-range damping is applied to avoid a polarization catastrophe due to the usage of unphysical point multipoles, a known artifact of polarization models. This is done by smearing the interaction moment with a function

$$\rho(u) = \frac{3a}{4\pi}\exp(-au^3) \tag{2.27}$$

where $u = r_{ij}/(\alpha_i\alpha_j)^{1/6}$, r_{ij} is a linear separation, α_i is an isotropic atomic polarizability on site i, a is a dimensionless factor, controls damping strength and is universal ($a = 0.39$).

Damping functions for higher multipoles are derived recursively. Finally, the energy due to induction is given by

$$U_{Coulomb}^{(i)} = -\frac{1}{2}\left[\vec{\mu}_d^{(i)}\right]^{\dagger}\vec{E}^{(p)} \tag{2.28}$$

Despite using isotropic atomic polarizabilities, total molecular polarizabilities of small compounds are normally well reproduced. Yet, larger polarizabilities are used for carbons in conjugated fragments due to more polarizable π-states, than for carbons in alkyl chains with much more localized states.

2.2.2 Technical details of MD simulations

Since the purpose of MD simulations is to study dynamics of classical systems, one needs to know how to propagate such systems, provided various ways to generate such forces through various force fields. In the following, one reviews such propagation algorithms, as well as related topics.

Integrators

In MD simulations, time evolution of a system is obtained via integration of N coupled Newton's equations of motion of N particles in a simulation box

$$\vec{F}_i = m_i \frac{d^2\vec{r}_i}{dt^2}. \tag{2.29}$$

Here, $\vec{F}_i = \sum_j \vec{F}_{ij}$ is the force acting on the i-th atom (and calculated from pair-wise interactions, defined in point-charge force-fields), m_i is the mass and $\vec{r}_i$ is the instantaneous position of the i-th atom at time t. Each differential equation requires two initial conditions at time $t = 0$: Positions $\vec{r}_{0,i}$ and velocities $\vec{v}_{0,i}$. For atoms with $N > 2$, these equations have no closed analytical solution and must be solved numerically.

To solve equations in this way, they are discretized and propagated with finite-difference algorithms or integrators. Integrator is an expression that links positions (and velocities) $\vec{r}_i(t_1)$ of atoms at a time t_1 to their values $\vec{r}_i(t_2)$ at the following time t_2, where $t_2 > t_1$. One can obtain a number of integrators using Trotter decomposition, which are stable and reversible [93]. One of such integrators is the Verlet algorithm [94]. It is one of the oldest stable integrators, that is regularly used in MD simulations. It can be also obtained from the Taylor series of the trajectory around two points in time and reads

$$\vec{r}_i(t + \Delta t) \approx 2\vec{r}_i(t) - \vec{r}_i(t - \Delta t) + \frac{\vec{F}_i(t)}{m_i}\Delta t^2 + O(\Delta t^4). \tag{2.30}$$

The last term represents the discretization error of the algorithm. In the case of the Verlet algorithm it is of the order of Δt^4. Variations of this method include the leapfrog and the velocity Verlet algorithms, routinely used in MD simulation packages.

The last point should be made about the properties of trajectories, generated with (eq. 2.30) or similiar schemes. It is known that trajectories generated from MD simulations decorrelate quickly upon small perturbation of the initial positions (i.e. $\vec{r}_{0,i} + \delta\vec{r}_i$, $\vec{v}_{0,i} + \delta\vec{v}_i$) already within the first 100 steps of a simulation [61]. This property is known as Lyapunov instability [95]. However, one is not interested in the trajectories of individual particles, but in the statistical averages (observables) of the entire system. Because modern integrators are phase space and energy conserving (or, alternatively, coupled to a thermostat), correct statistics (i.e. ensemble) and observables can be obtained. In this way, molecular dynamics is a valid tool for studies of thermodynamic properties of molecular systems.

Constraints

It should be noted that the time-step Δt defines how far the system can be propagated and is desired to be as large as possible, as one wishes to have longer trajectories to ensure a proper sampling. Yet, one cannot set Δt to an arbitrary large value, as Δt must capture all dynamics of the system, including its fastest motions such as bond vibrations occurring on the femtosecond time-scales. Hence, Δt must be on the sub-femtosecond scale to reproduce such motions. In practice, the fastest DOFs typically contribute in an averaged way (see the time-scale separation of DOFs) and can be constrained to their average values. In the case of bond vibrations, one typically imposes bond-length restraints, which allow to increase the time-step by up to one order of magnitude. The LINCS algorithm is often used in MD simulations for this purpose [96], which solves constrained Newton's equations of motion

$$-\mathbf{M}\frac{d^2\vec{r}}{dt^2} + \mathbf{B}^\dagger\vec{\lambda} + \vec{f} = 0, \tag{2.31}$$

for $3N$ degrees of freedom, $\vec{r}$ is a generalized positions in the configuration space, $\mathbf{M}$ is the mass matrix, $B_{ij} = \partial g_i/\partial r_j$ is the direction constraint matrix, $\vec{g}(\vec{r}) = 0$ is a set of rigid constraints, $\vec{\lambda}$ is the vector of Lagrange multipliers and $\vec{f}$ is the vector of forces. The algorithm is time reversible and is implemented in a number of MD simulation packages.

Evaluation of non-bonded interactions

Even after shifting the problem from ab initio level to classical mechanics, one still cannot simulate realistic systems in terms of observed sizes (μm $-$ m) and times (μs - s) due to limited computational resources. Currently, simulations only begin to approach these scales. Typical simulated system sizes are, in fact, in nm to μm range, while simulated times are between ns and μs. Because of this mismatch, one is interested in reliability of simulated properties, compared to bulk characteristics in real materials. Indeed, interaction at a surface of the system create finite-size effects, hence the thermodynamic limit is not applicable.

Also, short simulation times may be insufficient to sample thermodynamic properties and to observe equilibrium dynamics of a system, so one faces sampling problems as well.

The finite size effects can be substantially reduced via periodic boundary conditions (PBC). In this approach, the system is surrounded by its replicas. This removes the interface and allows to simulate properties of an infinite system, that are much closer to real conditions. To ensure that each particle interacts with other particles only once, a minimal-image convention is used, which requires to apply cut-off $r_c < L/2$, and L is the smallest box dimension. Even so, using PBC does not cure the finite-size problem completely. PBC introduces artifacts to spatial correlations and properties that are related to them, for example those at transition points. Therefore, one should use sufficiently large box sizes even while using PBC. Another consequence of this approach is that one needs to evaluate long-range interactions, including self-interactions between charges and their images.

Because of the pair-wise nature of non-bonded potentials, the evaluation of non-bonded contributions to the forces scales as $O(N^2)$ with number of atoms and is, therefore, the most time-consuming part of simulations. One applies cut-offs to reduce scaling from quadratic N^2 to linear N. The maximum cut-off value is defined by the half of the smallest box dimension (minimal image convention), so that no particle can interact with itself. This works well for the van der Waal interaction, which decays as r^{-6} and therefore short-ranged. Electrostatics on the other hand decays as r^{-1} and noticeable errors come out of truncation. A proper way to evaluate the electrostatic contributions is to use the Ewald summation technique.

Ewald summation

To derive the Eewald method [97, 98], one begins with the total interaction energy of a neutral system with N charged particles

$$E = \frac{1}{4\pi\epsilon_0} \sum_{i>j} \frac{q_i q_j}{r_{ij}} \tag{2.32}$$

where q_i is the charge of particle i, $r_{ij} = |\vec{r}_i - \vec{r}_j|$ is the distance between particles i and j, $1/4\pi\epsilon_0$ is an electrostatic constant. The computation time of the calculation scales as $O(N^2)$ with the number of particles and is the most expensive part of MD simulations.

The simulation box is described by three vectors $\vec{L}_1$, $\vec{L}_2$ and $\vec{L}_3$, and the volume of the cell is $V = \left(\vec{L}_1, [\vec{L}_2 \times \vec{L}_3]\right)$. Therefore, there are infinitely many charges q_i located at positions $\vec{r}_{inf,\,i} = \vec{r}_i + \sum_\alpha n_\alpha \vec{a}_\alpha$, where index α goes through independent directions, $\alpha = 1, 2, 3$, and numbers n_α are integers. For simplification, one can rewrite vector $\vec{r}_{inf,\,ij}$ symbolically as $\vec{r}_{inf,\,ij} = \vec{r}_{ij} + \vec{n}L$, where L is the length of the cubical simulation box. The total Coulomb energy of an infinite system then takes the form

$$E = \frac{1}{8\pi\epsilon_0} \sum_{\vec{n}} \sum_{i,\, i\neq j}^{N,N} \frac{q_i q_j}{|\vec{r}_{ij} + \vec{n}L|}, \tag{2.33}$$

where self-interactions are excluded only for the central box with $\vec{n} = 0$. Though this sum is conditionally convergent, but the rate of convergence depends on a system and a way of summation. This also results on numerical errors that may lead to different answers. In the Ewald method, one re-writes the sum in a way, that allows rapid convergence.

The main idea is to split the electrostatic potential of a point charge $\frac{1}{r}$ into short-range and long-range components via an error function

$$\mathrm{erf}(x) = \frac{2}{\sqrt{\pi}} \int_0^x e^{-t^2} dt \tag{2.34}$$

and its complementary $\mathrm{erfc}(x) = 1 - \mathrm{erf}(x)$ as

$$\frac{1}{r} = \frac{\mathrm{erf}(\frac{1}{2}\sqrt{\eta}r)}{r} + \frac{\mathrm{erfc}(\frac{1}{2}\sqrt{\eta}r)}{r}, \tag{2.35}$$

and the value of parameter η defines the partition of the space. Within this decomposition, one can re-write the initial energy expression in three parts

$$E = E_L + E_S - E_{self}. \tag{2.36}$$

Here E_L is the energy due to interactions by means of long-range coulomb potential, E_S is the short-range analogue, which includes the $\vec{n} = 0$ case, and E_{self} is a compensating self-interaction energy, caused by inclusion of $\vec{n} = 0$ box into the calculation of the E_S. This equality is exact and the three terms are given by

$$E_S = \frac{1}{8\pi\epsilon_0} \sum_{\vec{n}} \sum_{i,\ i \neq j}^{N,\ N} \frac{q_i q_j}{|\vec{r}_{ij} + \vec{n}L|} \mathrm{erfc}\left(\frac{|\vec{r}_{ij} + \vec{n}L|}{\sqrt{2}\sigma}\right) \tag{2.37}$$

$$E_L = \frac{1}{2V\epsilon_0} \sum_{\vec{k} \neq 0} \frac{e^{-\sigma^2 k^2/2}}{k^2} |S(\vec{k})|^2 \tag{2.38}$$

$$E_{self} = \frac{1}{4\pi\epsilon_0} \frac{1}{\sqrt{2\pi}\sigma} \sum_{i=1}^{N} q_i^2. \tag{2.39}$$

Here σ is an adjustable parameter, V is the volume of the system, that is $V = L^3$. Because of the cut-off function $\mathrm{erfc}(x)$, the short-range part of the sum now converges rapidly in the real space. The long-range part E_L, similarly, is summed over the k-vectors of the reciprocal space, in which this sum converges rapidly as well. Also, a structure factor $S(\vec{k})$ is introduced, which takes into account the shape of the simulation box. If one considers charged systems or systems with higher multipoles, additional terms should be included.

The classical Ewald summation method, presented above, with an optimal choice of parameter $\sigma(N)$, scales as $O(N^{3/2})$, which is only a mild improvement in the performance. A more efficient summation technique is the Particle Mesh Ewald method (PME), where the reciprocal-space energy contribution is evaluated using discrete Fast-Fourier Transform (FFT) on a grid. The FFT method, via an appropriate choice grid spacing, allows to reduce the computational complexity of the Ewald summation from $O(N^{3/2})$ to a much better $N \log(N)$ scaling. In this form, PME is implemented in various MD packages.

Thermostat and barostat

The propagation of a system using Newton's equations of motions is equivalent to the NVE ensemble. However, in reality experiments are performed under conditions of constant pressure and constant temperature, which correspond to NPT ensemble. For this reason, equations of motion are coupled to a thermostat and a barostat, in order to reproduce an intended statistics.

For a thermostat, a velocity rescaling thermostat [99] is often used, which ensures that MD simulations are performed in a canonical (NVT) ensemble. It is based on the (non-canonical) Berendsen's velocity rescaling scheme, which is then corrected by a properly chosen random variable. In a velocity rescaling scheme, kinetic energy at a new time step is based on its previous value through

$$dK = (\bar{K} - K)\frac{dt}{\tau_t} + 2\sqrt{\frac{K\bar{K}}{N_f}}\frac{dW}{\sqrt{\tau_t}}, \tag{2.40}$$

in order to smooth fast fluctuations of K. Here dK is the change of the kinetic energy over time dt, τ_t is a time-scale of the thermostat, $\bar{K}$ is the average kinetic energy at a target temperature T, N_f is a number of a degrees of freedom in a system and dW is a Wiener noise. Defined in this way, dynamics of the kinetic energy K leaves a canonical distribution unchanged and generates a proper NVT ensemble.

Similarly, the pressure is coupled to a system in MD simulations via Berendsen algorithm [100], in which the instantaneous pressure is corrected according to

$$d\hat{P} = \left(\hat{\bar{P}} - \hat{P}\right)\frac{dt}{\tau_p}, \tag{2.41}$$

where $\hat{P}$ is a instantaneous pressure value and $\hat{\bar{P}}$ is a target reference. In this scheme the box vectors and particle coordinates are rescaled using a scaling matrix $\hat{\mu}$, defined as

$$\mu_{ij} = \delta_{ij} - \frac{dt}{3\tau_p}\beta_{ij}\left(\bar{P}_{ij} - P_{ij}\right). \tag{2.42}$$

Here $\hat{\beta}$ is a diagonal isothermal compressibility tensor of the system ($\beta_{ij} = \beta\delta_{ij}$ and $\beta = 4.5 \cdot 10^{-5}$ bar^{-1}), τ_p is a time-scale of the barostat. As it was mentioned earlier, the resulting ensemble does not exactly reproduce the NPT ensemble, and therefore is only used during system equilibration or morphology generation runs.

Limitations of molecular dynamics

Regarding computer simulations, there is always a trade-off between the precision and the system size or the simulation time. An increase of the system size or simulation time always goes along with a decrease of the accuracy of the model. If further simplifications are required, one can use coarse-graining (CG), mean field theories and continous models. In novel simulation techniques, attempts are made to combine simulation methods of varying accuracy in order to simulate a region of interest at a higher resolution for a longer time, while treating its enviroment at a lower level of theory [101].

2.3 Static and dynamic characterization of morphologies

Upon simulation of morphologies with MD, the ordering and the dynamics of a system can be characterized by a set of order parameters, such as a dynamic order parameter S and a nematic order parameter Q, which originate from liquid crystal theory [102]. They can be applied to partially ordered materials, like organic semiconductors, to link their structure and dynamics to a performance in organic electronics devices. In particular, morphologies of small molecules [103–106] and polymers (alignment [107, 108] and crystallization dynamics [106]) can be investigated. In the case of semi-crystalline polymers and molecular crystals, one can use the paracrystallinity parameter to assess the degree of their ordering in simulations [107, 108]. These parameters not only reflect the structural properties, but are also useful to study phase transitions [108]. In the following, these three order parameters are introduced.

2.3.1 Dynamic order parameter

The dynamic order parameter S reflects a degree of orientational order of molecular fragments in a simulated morphology. For example, one may be interested in the dynamics of C-H bonds attached to the conjugated core, or C-C bonds in alkyl side-chains. A time evolution of these bonds is reflected through the parameter S, which is defined as [108]

$$S = \left\langle \frac{1}{N} \sum_{i=1}^{N} \left(\frac{3}{2} \left(\vec{U}^{(i)} \cdot \vec{u}^{(i)} \right)^2 - \frac{1}{2} \right) \right\rangle . \tag{2.43}$$

Here, the summation is conducted over N equivalent molecules and represents the ensemble average, the angular brackets $\langle \dots \rangle$ stand for the time average. The vector $\vec{u}^{(i)}$ is the

instanteneous orientation of the bond of interest at time t, belonging to the i-th molecule. It is compared to its time average $\vec{U}^{(i)} = \langle \vec{u}^{(i)} \rangle$ via projection. All vectors are typically measured in the laboratory frame of reference, which is the simulation box, and have to be normalized, so that $|\vec{U}^{(i)}| = 1$ and $|\vec{u}^{(i)}| = 1$. Time averages are calculated as a sum over the time frames of the simulated trajectory.

If bonds retain their orientation through time, the instanteneous and the mean orientations will remain identical: $\vec{U}^{(i)} \approx \vec{u}^{(i)}$, resulting in the order parameter being close to one, $S \approx 1$. Such a situation is observed in molecular crystals at low temperatures or other dense self-restrained environments. On the other hand, $S = 0$ is obtained for uniformly rotating vectors (in a solid angle 4π), and would be typical for small molecules in the gas phase. Parameter S is defined in the interval $[0, 1]$ and reflects the time-averaged degree of orientation order of a system.

It is worth mentioning that S can take negative values as well. This is possible in case of uniaxial precession for angular values $\phi > 55°$. Such a motion is typical for CH_3 bonds of the terminal moieties of the alkyl side-chains. This effect has a purely topological origin, and cannot be observed in case of two-dimensional continuous trajectories.

Often, parameter S is compared to the experimental data obtained from the solid-state NMR measurements [104]. Though the calculated and measured values are correlated, the two quantities are not the same. This can be seen from the fact that the experimental value S_{NMR} can be positive only, while the calculated parameter S can be negative as well. For this reason a generalized order parameter $\mathcal{S}$ is introduced. Physically, it reflects the orientation decoupling of the two neighboring spins, as it is measured in the NMR experiments. In the following section, I introduce the generalized order parameter $\mathcal{S}$ and show how it can be calculated from MD trajectories.

2.3.2 Generalized order parameter

In NMR experiments, the spin dynamics is followed through measuring the decoupling of two precessing spins as a function of time. The result is an autocorrelation function (ACF), that represents the dynamics of two coupled dipoles, located on two neighboring nuclei, with a separation comparable to a C-C bond length. The measured generalized order parameter $\mathcal{S}$ is then defined as a long-time limit of the autocorrelation function and is always positive or zero. The generalized order parameter is sensitive to the local environment and provides an insight into the dynamics of systems at a semi-atomistic resolution and can be compared to the atomistic MD simulations. The resolution of NMR measurements decreases, when several spin pairs have similar environments, and their signals cannot be distinguished. In this case, the generalized order parameter value becomes a group-averaged quantity.

To extract the generalized order parameter from MD trajectories, we follow the formalism, developed by Lipari and Szabo [109, 110]. The interaction between a pair of dipoles is described by the autocorrelation function

$$C(t) = \left\langle D_{q0}^{(2)\dagger}(\Omega(\tau)) D_{q0}^{(2)}(\Omega(t+\tau)) \right\rangle_{\tau}. \tag{2.44}$$

Here, $D^{(2)}_{nm}(\Omega)$ is a Wigner D-matrix, defined for a vector $\vec{u}$ on a unit sphere ($|\vec{u}| = 1$). It is uniquely defined by its angular coordinate $\Omega = (\theta, \phi)$. The vector $\vec{u}$ is the normalized displacement vector that connects the two nuclei, $\vec{u} = \vec{r}_{ij}/|\vec{r}_{ij}|$, measured in the global frame of reference, i.e. the simulation box. Applying the addition theorem for spherical harmonics, one can re-write the autocorrelation function in terms of the second Legendre polynomial, $P_2(x) = 3/2 \cdot x^2 - 1/2$:

$$C(t) = \frac{1}{5} \left\langle P_2 \left[\vec{u}(\tau) \cdot \vec{u}(t+\tau) \right] \right\rangle_\tau . \tag{2.45}$$

The scalar product $\vec{u}(\tau) \cdot \vec{u}(t+\tau) = \cos(\theta_t)$ is the instanteneous orientation of the bond with respect to a reference time τ. Time averaging $\langle \dots \rangle_\tau$ is conducted over all initial times τ. In the case of isotropic motions of a molecule as a whole, the total autocorrelation function rigorously factorizes

$$C(t) = C_W(t) \cdot C_I(t). \tag{2.46}$$

The two factors, $C_W(t)$ and $C_I(t)$, are the correlation functions of the overall and the internal molecular motions, respectively. The overall motion of the molecule can be modeled by a single exponential decay, $C_W(t) = 1/5 \cdot \exp(-t/\tau_W)$, where τ_W is the correlation time of the global molecular motion. In this case, the internal autocorrelation function simplifies to

$$C_I(t) = \left\langle P_2 \left[\vec{u}(\tau) \cdot \vec{u}(t+\tau) \right] \right\rangle_\tau , \tag{2.47}$$

which is the expression that is routinely used in MD simulations of biomolecules. The parameter $\mathcal{S}_{LS}$ for an arbitrary bond is then defined as the long-time limit of the derived autocorrelation function

$$\mathcal{S}^2_{LS} = \lim_{t \to \infty} C_I(t). \tag{2.48}$$

The subscript LS stands for Lipari-Szabo method, so one can distinguish it from the dynamic order parameter S originating from liquid crystal theory, as described previously.

Effect of bond vibrations

In the previous derivations the bond distances were considered to be static. One may wish to introduce a bond-dependent order parameter $\mathcal{S}_{LS}{}'$ defined as

$$\mathcal{S}^2_{LS}{}' = \left\langle r^{-3} \right\rangle^{-2} \lim_{t \to \infty} \left\langle \frac{P_2 \left[\vec{u}(\tau) \cdot \vec{u}(\tau+t) \right]}{r^3(\tau)\, r^3(\tau+t)} \right\rangle . \tag{2.49}$$

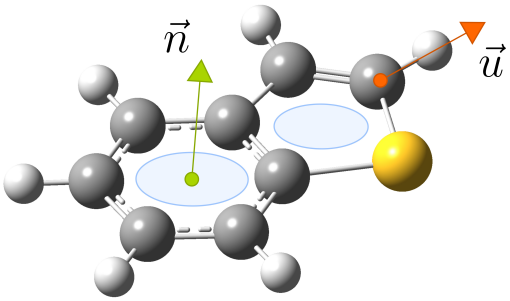

Figure 2.3: Vectors used for order parameter calculations: the unit vector $\vec{u}$ along the bond for dynamic order parameter S, and a norm to the molecule's conjugated core $\vec{n}$ for calculations of nematic order parameter Q. Blue circles mark the plain of the conjugated core.

This expression is useful to assess the errors due to bond restraints, which are often used in MD simulations (such as LINCS algorithm). The effect of the bond vibrations is found to be insignificant as bonds decorelate fast (fs). These times modify early values of the ACF and have no significance for the order parameter, calculated as a long-time limit of the ACF. The original generalized order parameter $\mathcal{S}^2_{LS}$ is contained in eq. 2.49 as the limiting case of a constant distance between the two dipoles.

Practical considerations

In practice, the precision of the autocorrelation function $C_I(t)$ is limited by the length of an MD trajectory. To assess the asymptotic behavior of the data, one can fit a truncated polynomial or exponential series to the tabulated autocorrelation function as

$$C_I(t) = \sum_{n=0}^{N} a_n \exp(-t/\tau_n). \tag{2.50}$$

In the limit of large times, the generalized order parameter is the zero-order coefficient of the expansion, that is $\mathcal{S}^2_{LS} = a_0$. This approach, however, may result in large numerical errors due to fluctuations in the plateau region of the autocorrelation function.

An alternative approach is to identify the converged region of the function $C_I(t)$ and average over it. In this way the error bars of calculations are significantly reduced, and the error-prone fitting can be avoided. The downside of the approach is that long, converged ACFs are required, which in turn require long production runs. When simulating molecular crystals the ensemble average leads to an additional error reduction. In cases where the dominant part of the autocorrelation function is a converged region, one can use the following time average

$$\mathcal{S}^2_{LS} = \frac{3}{2}\left(\langle u_x^2\rangle^2 + \langle u_y^2\rangle^2 + \langle u_z^2\rangle^2 + 2\langle u_x u_y\rangle^2 + 2\langle u_x u_z\rangle^2 + 2\langle u_y u_z\rangle^2\right) - \frac{1}{2}. \tag{2.51}$$

Here, $\{u_i\}, i = \overline{1,3}$, are the corresponding projections of the vector $\vec{u}$ onto the simulation box axes. The results obtained with this expression, are identical to those obtained from tail averaging, in the case of infinitely long trajectories.

As a general note, it should be pointed out that the simulated dynamic order parameter is always higher than the value measured in the SS-NMR. The more time passes, the more conformations are sampled and the lower values of S are observed. Hence, measuring the order parameter is subjected to sampling problems. It can be seen from (eq. 2.50) that the value of the order parameter is defined by the largest relaxation times. Due to the finite size and time of the MD simulations, certain regions of the configuration space are explored poorly (or not explored at all). Moreover, slow motions are typically associated with larger molecular fragments, which may be excluded due to the finite size of the simulation box. The lack of this contribution causes overestimation of the order parameter and underestimation of the dynamics. To assess the effects of limited simulation times and finite size effects, one should check the convergence of the autocorrelation function $C_I(t)$. In order to do this, a combination of larger system sizes and longer simulation times must be considered, which is often not feasible.

Simple models

The generalized order parameter can be interpreted in terms of certain motions. Diffusion of the vector in a cone with an opening angle θ is a reasonable model for a fast motion of a C-H bond attached to the backbone or C_n-H bonds grafted on side-chains. In this case the parameter takes the following functional form

$$\mathcal{S}^2_{cone} = \left[\frac{1+\cos(\theta)}{2}\cos(\theta)\right]^2. \tag{2.52}$$

For an ideal methyl group with three equivalent C-H bonds, rotating about the stationary axis, the order parameter for a single CH bond is given by

$$\mathcal{S}^2_{rot} = \left[\frac{1}{2}\left(3\cos(\beta)^2 - 1\right)\right]^2 = {S_{rot}}^2. \tag{2.53}$$

Here, β is the angle formed by the vector $\vec{u}$ and the symmetry axis. This expression is valid for any shape of the dihedral potential. Also it is identical to the value obtained from the liquid crystal order parameter S. For a CH_3 group the angle β takes the value of $109.5°$, and leads to $\mathcal{S}_{rot} = 0.33$.

Another characteristic value is the angle at which the order parameter becomes zero. It is a well known value in NMR experiments, namely the "magic spinning" angle, $\beta = 54.74°$. If the axis is diffusing itself, a correction should be made

$$\mathcal{S}^2_{total} = \mathcal{S}^2_{rot}\mathcal{S}^2_{axis}. \tag{2.54}$$

Unfortunately, this factorization is only valid if the two motions are uncorrelated and is found, for example, in a terminal CH_3 group of a side-chain. Due to stiff bonded potentials between the carbons within the chain, the motions between them are strongly correlated. The longer the chain becomes, the more complicated motions it exhibits. This can be seen from a model of a short chain with four repeat units, C_1-C_2-C_3-C_4, for which the order parameter of the terminal bond, C_3-C_4, is given by

$$\mathcal{S}^2{}_{34} = \mathcal{S}^2{}_{12} \left[1 - 3 \left\langle \Delta\psi^2 \right\rangle \sin^2 \phi\right] . \tag{2.55}$$

Its dynamics is influenced by the dynamics of the first bond $\mathcal{S}^2{}_{12}$ and a stiff dihedral, characterized by the angle ψ with a small angular variance $\left\langle \Delta\psi^2 \right\rangle$. With a growing complexity of the analytical models, one has to use the original expressions, such as eq. 2.48, to asses the order parameter $\mathcal{S}^2$. For this reason, the direct interpretation of the motions of the molecular fragments becomes impossible.

2.3.3 Nematic order parameter

Similarly to the dynamic order parameter, one can define a nematic order parameter Q which tracks the orientation variation of a molecular ensemble in a simulation box. It is typically defined as a three-dimensional rank-2 tensor $\hat{Q}$ with the components

$$Q_{\alpha\beta} = \left\langle \frac{1}{N} \sum_{i=1}^{N} \left(\frac{3}{2} n_\alpha^{(i)} n_\beta^{(i)} - \frac{1}{2} \delta_{\alpha\beta} \right) \right\rangle . \tag{2.56}$$

Here, $\vec{n}$ is defined as a norm to the plane of the molecule's conjugated fragment. The value $n_\alpha^{(i)}$ is the α-component of the norm vector $\vec{n}$ to the surface of the conjugated fragment. $\vec{n}$ must be a unit vector, $|\vec{n}| = 1$. The symbol $\delta_{\alpha\beta}$ stands for the Kronecker delta and the angular brackets $\langle \dots \rangle$ denote the time average. A summation is conducted over N equivalent molecules and gives an ensemble average. Due to time discretization of MD trajectories, a similar sum is introduced for time-averages as well.

The largest absolute eigenvalue of the matrix $\hat{Q}$ then defines the scalar nematic order parameter Q that can take values in the range of $[0, 1]$. The lowest value $Q = 0$ depicts the complete absence of the orientation order at any given time, and $Q = 1$ represents perfect alignment of given molecules or their synchronous motion. As a result, intermediate values of Q correspond to an intermediate degree of orientation disorder in the simulation box. Since the temperature increase promotes defect formation, the parameter Q decays with increasing temperature.

Finally, we address the relationship between the two parameters, S and Q. Despite the observed correlation between two parameters, they are independent. This can be seen from an example of two toy system trajectories in two dimensions, shown in (fig. 2.4). In the first case, the molecules are rotating uniformly about their centers of mass. Each molecule explores all available orientations with time, leading to $S = 0$. However at any given time all molecules are all oriented in the same direction, and therefore $Q = 1$. A completely

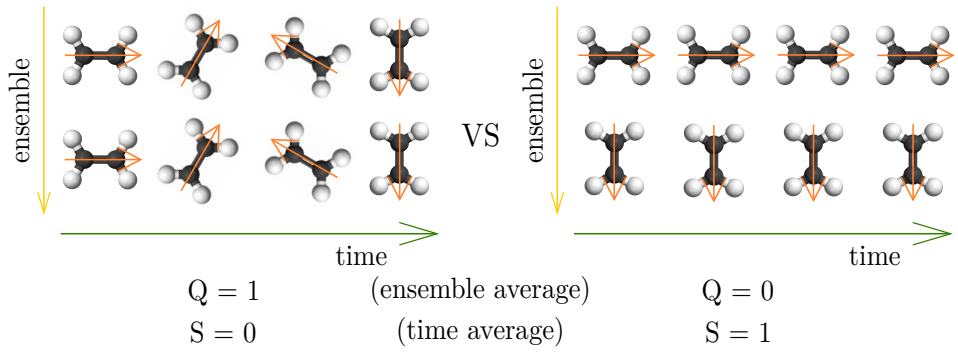

Figure 2.4: Independence of the dynamic and nematic order parameters. The two limiting cases are: A simultaneous rotation of molecules around their centers of mass, where $Q = 1$ and $S = 0$ (left), and a frozen morphology, in which $Q = 0$ and $S = 1$ (right).

opposite situation is observed in the second case, where the morphology is frozen and $S = 1$. Yet every molecule has a different direction, and $Q = 0$ on average. These two examples are the limiting cases, and intermediate values of Q and S can be adopted independently as well. The often observed correlation between the two order parameters stems from the restricted motions due to the local morphological confinement and a similar temperature dependence.

2.3.4 Paracrystallinity

When working with molecular crystals and semi-crystalline polymers at finite temperature, one would like to asses the "ideality" of such a crystal. This can be done through the calculation of a paracrystalline order parameter, g_{hkl}, which is defined as

$$g_{hkl}^2 = \frac{\langle {d_{hkl}}^2 \rangle}{\langle d_{hkl} \rangle^2} - 1 \tag{2.57}$$

Here, indexes (hkl) set the crystallographic direction of interest, d_{hkl} is the distance between the centers of mass of two molecules or repeat units in polymer chains, projected on the chosen direction (hkl), the averaging $\langle \dots \rangle$ is a sum over all equivalent molecular pairs in a neighborlist, and the neighborlist is defined via a cut-off, typically defined to be between the first two peaks of the distance distribution function $p(d_{hkl})$. If the first and consecutive peaks of the $p(d_{hkl})$ function are not fully separated (i.e. overlapping), the cut-off is applied at the minimum between the first and the second peak. The typical choice for (hkl) in semi-crystalline samples of conjugated polymers would be the π-stacking direction, defined along the direction of the lamellar growth.

If the Gaussian distribution is assumed for the distance distribution (and is indeed often observed in simulations), one can rewrite the equation simply as

$$g_{hkl}^2 = \frac{\mathrm{Var}(d_{hkl})}{\mathrm{E}(d_{hkl})^2} \tag{2.58}$$

where E(d_{hkl}) and Var(d_{hkl}) are the mean and the variance of the first peak of a distance distribution, thus clearly revealing the meaning of the g^2_{hkl}, which is a mean-normalized variance of the first peak of a $p(d_{hkl})$ function. In the case of a perfect crystal at low temperatures it is close to zero, and increases with temperature due to defect accumulation.

The paracrystalline parameter can be also assessed from peak broadening in scattering experiments, such as XRD. The lower paracrystallinity values, calculated in the MD simulations, are typically attributed to over-idealized simulated morphologies. In reality, material morphologies are much more disordered due to polydispersity of polymers, imperfect self-organization, grain boundaries and more.

2.4 Charge transport simulations

Provided a realistic, compound-specific morphology, one can proceed with simulations of charge dynamics in it. In the following sections, existing theories and simulation techniques are presented. A brief overview of charge localization effects is followed by rate-based approaches to charge dynamics, including Marcus charge transfer theory. The key ingredients of Marcus theory are discussed, as well as the ways to simulate them. Finally, an equation of motion for charges, known as Pauli's Master equation and ways to solve it, such as Kinetic Monte Carlo, are discussed. The resulting KMC trajectories can then be used to calculate observables, in particular the mobility μ, which is an important macroscopic parameter for a solar cell performance.

2.4.1 Role of localization

At the beginning, it is useful to understand the difference between a crystalline (such as silicon) and an amorphous semiconductor in terms of energy states. Solids are well described by a model of an ideal crystal at low temperatures. It is characterized by highly delocalized states, high electronic coupling elements ($J > 1$ eV), and consequently a coherent transport, with high transport coefficients, like mobility μ or conductivity σ. This type of transport is known as band transport and is qualitatively described by the Drude-Lorentz model. Introducing impurities and phonons (high temperatures) leads to an effective localization of the states (an effect known as Anderson localization [111, 112]) and a decrease of the transfer integrals, which in turn decreases the corresponding transport coefficients.

On the other hand, in organic semiconductors energy states are naturally localized. This often results in rough energy landscapes and small transfer integrals $J < 10^{-1}$ eV. In systems with such properties, charges exhibit a hopping-like transport, slowed down by small couplings and broad energy distributions, with mobilities typically varying in the range $10^{-9} - 10^{-2}$ cm^2/Vs. To overcome the problem of small transfer integrals and rough energetics, novel materials with large conjugated cores are investigated. The notable example is the polymer semiconductor PCDTPT [113], holding the hole mobility record of 23.7 cm^2/Vs for organic light emitting diode (OLED) devices. In the following, the key ideas of the hopping transport are presented.

2.4.2 Time-scale separation in molecular systems

Though the coupling between the electronic and nuclear degrees of freedom is strong in organic semiconductors, one assumes the following ladder of time-scales, $\tau_{er} << \tau_{ct} << \tau_{nr}$, according to which the charge transport times τ_{ct} are much faster than the nuclear relaxation times τ_{nr}, and yet much slower than the polarization time τ_{er} of the electronic degrees of freedom in the environment. For this reason, a frozen morphology approximation is often used, and the charge dynamics depends only on the electronic density of states and the probabilities to hop between two molecules in a sample. This set of assumptions is often used to simulate charge transfer in small molecules [114] and polymer semiconductors [107, 108], and produces simulated mobilities in good agreement with experimental data.

2.4.3 Marcus rates

To obtain the charge dynamics one should solve the time-dependent Schödinger equation. Though this can be done, this approach is impractical and a simpler, rate-based approach is adopted. In it, the information about the system is represented by a directed graph and the transition probabilities between the nodes of this graph. One can impose rates on the basis of generic physical ideas.

An example is the correlated Gaussian disorder model (CGDM) [115], where site energies are distributed normally and spatially correlated. An important result is that within the model, one can correlated the energetic disorder σ to the randomly-oriented dipole moment of a molecule $\vec{p}$, i.e.

$$\sigma = 2.35 \frac{qp}{\epsilon a^2}, \tag{2.59}$$

where ϵ is the dielectric constant and q is the electric charge of the charged site. Hence, compounds with larger dipole moments should exhibit higher energetic disorder. It also links carrier mobility μ to an external field F as $\mu \sim \exp(\alpha\sqrt{F})$, where α is a dimensional prefactor. This is known as the Poole-Frenkel behavior and is often observed in organic semiconductors. If one also considers a finite charge density in the system, (an extended Gaussian disorder model [116]), one obtains a dependence of mobility on the energetic disorder

$$\mu \sim \exp(-C\hat{\sigma}^2). \tag{2.60}$$

It states that higher energetic disorder reduces the mobility in the system. However, these are lattice models and they do not establish a link to the chemical structure. Models' parameters must be parameterized from simulations or experiments.

Alternatively, one can derive the Marcus rate, an expression based on the molecule's atomic structure, i.e. linked to its electronic structure and environment. Introducing such details, however, comes at a price of substantially larger simulation times.

In classical charge transfer theory, one can derive the Marcus rate [117, 118]: The high-temperature limit where all vibrational modes of molecules are treated classically. To derive an expression for the rate, one begins with the Fermi's Golden rule, where a state 0 is coupled to the manifold of states α. The rate of transition to the manifold is then (for small couplings)

$$k = \frac{2\pi}{\hbar} \sum_{\alpha} |J_{0,\alpha}|^2 \delta(E_0 - E_\beta). \tag{2.61}$$

Here, $V_{0,\alpha}$ are interstate couplings and E_α are energy levels. If there are only two levels A and B, coupled to the classical thermal bath, one can write the rate [119] as

$$k_{ij} = \frac{2\pi}{\hbar} \int dq\ f(q) |J_{ij}|^2 \delta(U_i(q) - U_j(q)), \tag{2.62}$$

where $U_{i,j}(q)$ is the potential energy surface (PES) of donor/acceptor states, q is a set of coordinates, $f(q) \sim \exp(-U_i(q))$ is a distribution of configurations. If there is only one "reaction" coordinate q and the PES $U_{i,j}(q)$ are treated as parabolas, one can evaluate the integral analytically and arrive at the Marcus rate expression

$$k_{ij} = \frac{2\pi}{\hbar} \frac{J_{ij}^2}{\sqrt{4\pi\lambda_{ij} k_B T}} \exp\left[-\frac{(\Delta E_{ij} - \lambda_{ij})^2}{4\lambda_{ij} k_B T} \right]. \tag{2.63}$$

Here, ω_{ij} is a rate (probability per unit time) for a charge to hop from site i to site j, and a site represents a small molecule or a polymer chain fragment. Parameter J_{ij} is the electronic coupling between two localized monomer states, λ_{ij} is the reorganization energy due to a charge transfer event and ΔE_{ij} is the difference between the charge energies in the initial and final states, $\hbar$ is the reduced Planck constant, $k_B T$ is a thermal energy. These parameters are sensitive to the local and global ordering of organic compounds, and so atomistic morphology is an important ingredient shaping other parameters considerably.

As a side note, it should be mentioned that in addition to the classical Marcus rates, one can derive the semi-classical Jortner-Bixon [120, 121] or the quantum-tunneling Weiss-Dorsey [122–124] rates. The Marcus and Jortner-Bixon rates were compared previously and, though the two rates have notably different behavior in the inverted region, they produce similar rates and mobilities, since sufficiently large energy differences are never obtained. The Weiss-Dorsey rates are expected to deviate from those of Marcus at low temperatures, where nuclear tunneling is the dominant hopping mechanism. In the following, the Marcus rate expression will be used for charge transport simulations. Ways to derive its parameters are discussed in the following sections.

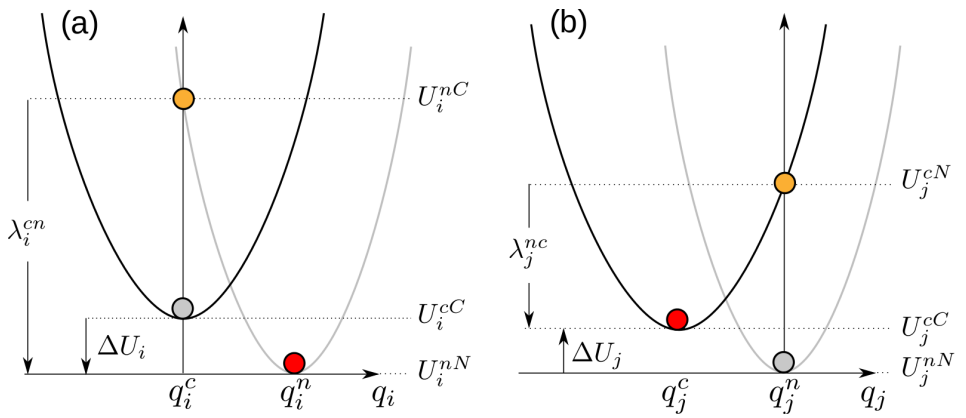

Figure 2.5: Potential energy surface, corresponding to a donor (a) and acceptor (b) molecules in charged and neutral states. The charge transfer dynamics takes place on two time scales: First the charge transfer between the two molecules occurs, and then nuclear degrees of freedom rearrange in the presence of a new potential. In a classical picture, the total internal reorganization energy is a sum of the corresponding energies on donor and acceptor molecules: $\lambda_{ij} = \lambda_i^{(cn)} + \lambda_j^{(nc)}$. The difference between the minima is the internal driving force: $\Delta E_{ij} = \Delta U_i - \Delta U_j$. Reprint from VOTCA manual [84, 125].

Reorganization energy

The first parameter required for the Marcus rate is the reorganization energy λ. It represents a response of the environment and the molecule in both nuclear and electronic degrees of freedom due to charge transfer. One can assume an additivity of the reorganization energy and factorize it into the internal and external components. The internal, the intramolecular reorganization energy, arises from the spatial adjustments of the nuclei and the core electrons in a dimer, where the charge transfer takes place. In a harmonic approximation, it can be calculated from four points of monomer geometries and charge states, which can be obtained for example from DFT calculations of the reaction's free energy profile as [107, 108, 126]

$$\lambda_{ij}^{(int)} = \lambda_i^{(cn)} + \lambda_j^{(nc)} = \left(U_i^{nC} - U_i^{nN}\right) + \left(U_j^{cN} - U_j^{cC}\right). \tag{2.64}$$

Here, U_i^{aA} is the total energy of the i-th molecule in the state a and in the geometry A, $\lambda^{(cn)}$ is the discharge energy of the first molecule (donor) and $\lambda^{(nc)}$ is the charging energy of the second molecule (acceptor) [115], as shown in fig. 2.5. The variance of the internal reorganization energies is typically much smaller compared to the energetic disorder and is often assumed to be constant for all molecules in a sample.

The external reorganization energy is a response of the surrounding molecules to a charge transfer and includes changes in the nuclear and electronic degrees of freedom. The electronic response can be accurately described by the polarizable force field applied to a frozen morphology [127]. The energy contributions due to the polarization effects will be treated in a separate section 2.4.3. The changes in the nuclear degrees of freedom are typically neglected due to frozen morphology approximation.

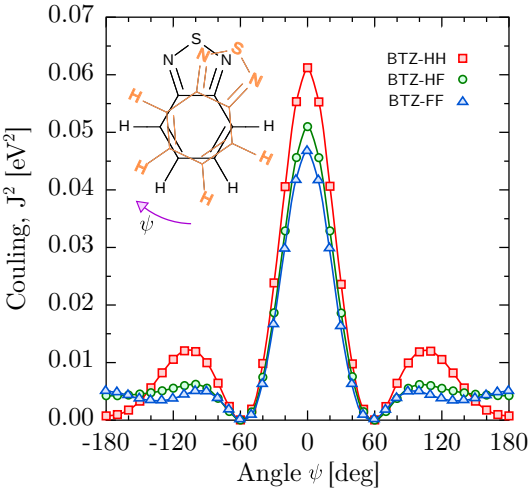

Figure 2.6: The scans of the transfer integrals $|J|^2$ as a function of rotation angle of the conjugated fragment BTZ and its derivatives. Depending on the local mutual orientation in a morphology, the transfer integrals typically vary on a logarithmic scale (i.e. by orders of magnitude) due to the nodal structure of the wave function, characteristic for the conjugated molecules.

Transfer integrals

The second component of the Marcus rate is the square of the transfer integral $|J|$, which is also known as an electronic coupling, and is defined as

$$J_{ij} = \langle \phi^{(i)} | \, \hat{H} \, | \phi^{(j)} \rangle \, . \tag{2.65}$$

Here $|\phi^{(i)}\rangle$ is a diabatic state localized on a molecule i and $\hat{H}$ is the Hamiltonian of a molecular dimer. In case of a hole transport, the state $|\phi^{(i)}\rangle$ is the highest occupied molecular orbital of a monomer (HOMO), while for the electron transport it is the lowest unoccupied molecular orbital (LUMO) within a frozen-core approximation.

It is characteristic for electronic couplings to depend strongly on the mutual orientation of two molecules that form a dimer. As an example, Figure 2.6 shows transfer integrals calculated as a function of angle ψ between two BTZ molecules in co-facial geometry, separated by $d = 0.37$ nm. Depending on the mutual orientation, an order of magnitude changes in values of $|J|^2$ are observed. Also, small changes in chemistry (fluorination of BTZ once and twice) notably modify the transfer integral values. For this reason, one must calculate couplings for each pair individually. Simulated morphologies often contain thousands of large conjugated molecules in the simulated trajectory. Therefore, the computation cost of transfer integral evaluation grows linearly with the number of molecules (provided the cut-off scheme is used to generate the neighbor list), as well as the number of atoms in them. There are several ways to calculate charge transfer integrals at various levels of theory.

Semi-empirical methods

Because integral calculations are time consuming, one can use parameterized models to speed up these calcultaions. These models are ofted referred to as semi-empirical methods. A common choice for fast integral evaluation is the ZINDO method. ZINDO (Zerner's Intermediate Neglect of Differential Overlap) [128, 129] is a variation of the CNDO and INDO methods developed in a series of papers by Pople et al. [130–134]. It is available in two variations: ZINDO/1, which was designed to perform geometry optimizations, and ZINDO/S, designed to study optical transitions. ZINDO/S is parametrized on a series of first principles calculations and can be used to estimate the overlap integrals in molecular dimers. Though the method is less accurate, one requires only a single monomer calculation in a vacuum. The resulting orbitals can be used to obtain overlap integrals for all dimers in the system by means of unitary transformations [135]. This makes the method extremely fast and suitable for charge transport simulations in large organic morphologies [107, 108, 136, 137]. On top of the accuracy issues, the method is parametrized only for a limited number of elements (first and second rows of the periodic table), and becomes inapplicable when materials contain heavier elements like silicon, germanium or metals, which are often used for substitution of the lighter atoms in order to vary some properties, like level alignment and bandgap, while preserving other properties, such as morphology and solubility. To study these materials, one should use more accurate, but computationally more expensive methods, such as DFT.

Projection of monomer orbitals

In the absence of well parametrized semi-empirical methods, such as ZINDO, one calculates the transfer integrals J_{ij} using the DFT method by projecting the monomer frontier orbitals onto the dimer Hamiltonian [138]. In this method the dimer Hamiltonian $\hat{H}$ and the overlap matrix S take the following form

$$J_{ij} = \vec{\lambda}^{\dagger}_{(i)} SDED^{\dagger} S^{\dagger} \vec{\lambda}_{(j)} \tag{2.66}$$

$$S_{ij} = \vec{\lambda}^{\dagger}_{(i)} SDD^{\dagger} S^{\dagger} \vec{\lambda}_{(j)} \tag{2.67}$$

In these matrix equations $\vec{\lambda}_{(i)}$ is an expansion coefficient of the monomer's state i in a given atomic basis set, S is the overlap matrix of the atomic basis functions, D contains the expansion coefficients of the dimer states, and E is the diagonalized dimer Hamiltonian. Solving the generalized eigenvalue problem $(\hat{H} - \hat{E}\hat{S})\vec{C} = 0$, using for example the Löwdin transformation [50], one can obtain the desired transfer integrals in the basis of the localized monomer states. It should be noted that the method can be used not only with DFT, but with any wave-function-based method.

In this approach, for each molecular pair one needs to perform two monomer and one dimer calculation, which are costly. Considering the typical scaling of the DFT method, which is

$O(N^3)$, the computation time of transfer integral evaluations scales as $(2+2^3)M \times O(N^3)$, where N is the number of monomer orbitals, and M is the number of molecular pairs in the trajectory.

Preserving the generality of the method, one may consider to parametrize a semi-empirical model, such as ZINDO [129], self-consistent tight-binding method SCC-DFTB [139], or a heuristic model, such as machine learning (a similar approach for multipoles discussed in [140]). In this case, only a fraction of the high-level calculations is needed, in order to generate a training set. Still, each new compound requires an individual parametrization.

Site energy differences

The third component of the Marcus rate is the site energy difference ΔE_{ij}, which drives the charge transfer reaction. One can evaluate these energies in a perturbative way [141]

$$\Delta E_{ij} = \Delta E_{ij}^{(vac)} + \Delta E_{ij}^{(el)} + \Delta E_{ij}^{(pol)} + \Delta E_{ij}^{(ext)}. \tag{2.68}$$

Here $\Delta E_{ij}^{(vac)}$ is the energy difference of an isolated molecule in the neutral and charged states (ionization potential I for holes and electron affinity A for electrons), $\Delta E_{ij}^{(el)}$ is the contribution that originates from the electrostatic interactions between the molecules, and $\Delta E_{ij}^{(pol)}$ is the stabilization energy due to the polarization effects. In case of an applied electric field, the corresponding term $\Delta E_{ij}^{(ext)}$ must be added. Combined with Ewald summation techniques, this approach allows to predict correct energetics at the organic/organic interfaces and, hence, V_{oc} values [127].

Internal energy differences

The internal energy difference of a molecular dimer in a vacuum can be written as

$$\Delta E_{ij}^{(vac)} = \left(U_i^{cC} - U_i^{nN}\right) - \left(U_j^{cC} - U_j^{nN}\right) \tag{2.69}$$

where U_i^{aA} is the total energy of the i-th molecule in the state a and in the geometry A, state cC corresponds to a charged molecule in the charged geometry and the nN to the neutral molecule in the neutral geometry. For a single-component morphology, this term cancels out, $\Delta E_{ij}^{(vac)} = 0$, but for multi-component systems it produces a non-zero value.

Electrostatic interactions

The electrostatic interaction between the two molecules (A and B) can be expressed in terms of multipoles, located at the nuclei positions, and derived from the calculated electron density of the molecules. The interaction term becomes

$$\Delta E_{AB}^{(el)} = \sum_{a=1}^{A} \sum_{b=1}^{B} Q_{pq}^{a} \cdot T_{pqrs}^{ab} \cdot Q_{rs}^{b} \tag{2.70}$$

In this expression, Q_{pq}^{a} is a spherical multipole moment located on the molecule A, and T_{pqrs}^{ab} is the multipole interaction tensor, that generates interaction for a pair of molecules A and B. Einstein's summation is performed over the indexes p, q, r and s. This energy corresponds to a first-order perturbation to the molecule's energy. One can obtain the expansion coefficients Q_{pq}^{a} from the distributed multipole analysis (DMA) of electron density [141]. Alternatively, one can fit molecule's total electron density to obtain partial charges only (zero-order multipoles), for example using the Merz-Kollmann method [142, 143]. Though the DMA method as a unique expansion is more robust, the two methods give similar results, hence, electron density fitting is often preferred for simplicity.

Induction effects

The third term in the site-energy expansion is the effect of the induction in the surrounding molecules on a molecular dimer, which hosts the charge transfer reaction. The energy correction due to the induction is always positive (and therefore stabilizes charges), and can be written in a symmetric form

$$U_{AB}^{(pol)} = \frac{1}{2} \sum_{a=1}^{A} \sum_{b=1,\ b>a}^{B} \left[\Delta Q_{t}^{a} T_{tu}^{ab} Q_{u}^{b} + \Delta Q_{t}^{b} T_{tu}^{ab} Q_{u}^{a} \right] \tag{2.71}$$

Here Q_{u}^{a} is a permanent and ΔQ_{t}^{a} is an induced dipole, located on the molecule A and T_{tu}^{ab} is the dipole-mediating interaction tensor. The induced multipole values are obtained through solving (eq. 2.71) self-consistently with the equation for the induced dipoles

$$\Delta Q_{t}^{a} = - \sum_{a=1}^{A} \sum_{b=1}^{B}{}' \ \alpha_{tt'}^{aa'} T_{tu}^{ab} (Q_{u}^{b} + \Delta Q_{u}^{b}). \tag{2.72}$$

Here $\alpha_{tt'}^{aa'}$ is the polarizability tensor, which is derived from the semi-empirical Thole model [92, 144] in a local dipole approximation, in which $\alpha_{tt'}^{aa'} = \alpha_{tt}^{aa}$ for polarizabilities located on a molecule A, and zero otherwise. Prime in the second sum implies $a \neq b$. A direct implementation of the Thole method, however, leads to so called polarization catastrophe. This stems from an attempt to reproduce a continuous electron density with a discrete model, and is resolved by introducing smearing of the charge distributions. Following the

implementation of the AMOEBA [145] force field, the smearing of the discretized electron density is done via an exponential prefactor

$$f(u) = \frac{3a}{4\pi} \exp(-au^3). \tag{2.73}$$

Here $u = R/(\alpha_a \alpha_b)^{1/6}$ is a dimensionless distance between the two polar sites, located on the nuclei, α_a is the isotropic atomic polarizability, and the value $a = 0.39$ has been shown to give an optimal performance of the model. In case of strongly anisotropic molecules, such as oligomers or polymer chains, one needs to rescale the polarizable volume of the molecule, $V \sim \mathrm{Det}|\hat{\alpha}|$, to reproduce the corresponding volume from first-principles calculations, where $\hat{\alpha}$ is the molecule's polarizability tensor.

2.4.4 Master equation

The dynamics of a charge can be described by a Master equation [114]. This is a memory-free approach, meaning that each new hopping event of the charge is independent of its previous history. The equation is

$$\frac{\partial P_\alpha(t)}{\partial t} = \sum_\beta \left[P_\beta \Omega_{\beta\alpha} - P_\alpha \Omega_{\alpha\beta} \right]. \tag{2.74}$$

Here $P_\alpha(t)$ is the probability of the system to be in a state α, $\Omega_{\beta\alpha}$ is a transition probability for a system to arrive to the state α from an a state β, and vice versa. The dynamics of the states is defined through a competition between transitions to and from each state. The components $\Omega_{\alpha\beta}$ form a transition matrix $\hat{\Omega}$.

One can rewrite this equation from state- to site-based picture. This is possible in the case of a single carrier dynamics, for which states $\{\alpha\}$ can be replaced with an equivalent occupation number formalism based on the set of site-based states $\{i\}$, since there is a unique map $\alpha_i = (0, \ldots, 1_i, 0, \ldots, 0)$. Within this formalism, one can write the Master equation as

$$\frac{\partial p_i}{\partial t} = \sum_j p_j \omega_{ji} - \sum_j p_i \omega_{ij} \tag{2.75}$$

This equation is similar to the initial Master equation, and represents the dynamics of a single carrier in terms of the site occupation probabilities p_i, where i is the site's index, and $\hat{\omega}$ is the transition matrix, which defines the hopping rates between the individual sites. In the case of multiple carriers, one needs to exclude double occupation of the same site due to the Pauli exclusion principle, which makes the corresponding Master equation non-linear. The Master equation, as in eq. 2.75, is a first order linear differential equation of the form $\dot{\vec{p}} = \mathbf{A}\vec{p}$ with an analytical solution

$$\vec{p}(t) = e^{\mathbf{A}t}\, \vec{p}(0). \tag{2.76}$$

Here $\vec{p}(0)$ is the initial state of the system at time $t = 0$. It can be solved using linear algebra methods. However, there are several limitations to this approach. For systems of interest, which may contain thousands of molecules, the transition matrix $\hat{\Omega}$ becomes large and difficult to diagonalize directly. Also, adding more carriers or carrier types leads to a non-linear equation that does not have a closed form analytical solution.

These issues can be resolved by using the kinetic Monte Carlo (KMC) technique [146–148]. In it, the hopping between two sites is attempted with a time τ, which is defined as $\tau = -\ln(r_1)/a$, here r_1 is a random number drawn from the uniform distribution in the unit interval. The result is simulated trajectory, that converges to a true Master equation solution for infinitely long times. The method can capture stationary and transient solutions and allows a straightforward extension to multiple carriers and carrier types. In particular, in the VOTCA simulation package, a combined variable step size (VSSM) [114] is implemented.

2.4.5 Mobility as an observable

Based on the trajectories obtained from the charge dynamics simulations using the KMC method, one can evaluate an ensemble average of an observable $\hat{A}$ with eigenstates A_α as

$$\langle A \rangle (t) = \frac{1}{s} \sum_\alpha A_\alpha s_\alpha(t). \tag{2.77}$$

Here s_α is the number of Markov states that ended up in a state α after time t, normalized by the total number of trials, s. The values must be taken after the equilibration time t_{eq}, since before this time charges are in the kinetic regime (also known as a sub-diffusion regime, in which $x(t) \sim t$). Though ergodicity is assumed, it is often not fulfilled in simulations, for example for ideal π-stacks of conjugated polymers.

It was noted in the introduction that the efficiency of the device strongly depends on the mobility of the charges in the constituent materials. One can calculate the mobility tensor directly from the KMC trajectories since $\langle \vec{v} \rangle = \hat{\mu}\vec{F}$, where $\langle \vec{v} \rangle = \Delta\vec{r}/\Delta t$ and $\Delta\vec{r}$ is the charge displacement vector, which corresponds to the simulation time Δt. In practice, individual components of the tensor $\hat{\mu}$ can be calculated by applying an electric field in orthogonal directions, which is followed by the averaging over S equivalent KMC simulations

$$\mu_{\alpha\beta} = \frac{1}{S} \sum_{s=1}^{S} \frac{v_\alpha^{(i)} F_\beta}{F^2}, \tag{2.78}$$

With this, the list of required methods and techniques is complete. In the following chapters, the outlined computational methods are used to investigate properties of polymer semiconductors: Quantum calculations are used to introduce molecule's chemistry, electrostatics. It is also used to build a classical Hamiltonian of the system, the force field, which is then used to generate atomistic morphologies of a material. Though morphologies pose interest on their own, they can also be used to study charge dynamics, when combined with Marcus charge transfer theory.

3 PCPDTBT derivatives: morphology and electronic properties

A number of conjugated semi-crystalline polymers has been successfully used as a hole-conducting material for solar cell's active layer, yielding record device efficiencies [10, 19, 21, 149]. This is due to favorable properties of these compounds: Low band gap values for efficient light absorption and suitable lamellar structures with high hole mobilities. Combined with flexibility, transparency and large-area production techniques, conjugated polymers are suitable materials for organic electronics applications. However, a complex structure of conjugated polymers polymers results in a variety of possible morphologies: Crystalline and disordered. And because charge transport is strongly influenced by these morphologies, identifying and controlling local and global packing of polymers is of great importance for creating efficient OPV devices.

PCPDTBT and its derivatives are such donor-acceptor polymers [150]. In the following, local packing, electronic and transport properties of PCPDTBT derivatives will be addressed via multiscale simulations. It will be shown that their crystalline structures go beyond the often considered π-stacking. Also, more then one π-stack packing is possible for these polymers. Another feature of PCPDTBT family is the presence of branched ethyl-hexyl side-chains, which are added to improve polymer's solubility. The disordered structure of side-chains and the electrostatics of donor units, however, cause high energetic disorder and prohibit an efficient hole transport in the lamellae.

3.1 Chemical structures

Poly[2,6-(4,4-bis-(2-ethylhexyl)-4H-cyclopenta [2,1-b;3,4-b']dithiophene)-alt-4,7(2,1,3- benzothiadiazole)], (also known as PCPDTBT)[41, 150, 151] are studied (fig. 3.1) is one of the first donor-acceptor hole-conducting polymers, presented as early as in 2006 by Brabec et al. It exhibits a low band gap ($E_g = 1.46$ eV) due to its DA architecture and high mobilities (up to $2 \cdot 10^{-2}$ cm^2/Vs) due to ability to form lamellar structures, resulting in solar cell efficiencies up to 5.5 %. The backbone contains cyclopentadithiophene (CPD) and 2,1,3-Benzothiadiazole (BTZ) units, where CPD unit is functionalized with two branched 2-ethyl-hexyl side-chains (ALK) for solubility (fig. 3.1).

Aiming at further improvements of solar cells, the chemical structure of PCPDTBT was systematically altered via chemical substitution. As a result, a family of derivatives P−X was created, where the symbol X defines the substituted atoms (fig. 3.2). In the first series, the bridging carbon of CDT (donor) unit is replaced by its heavy atom analogues Si and Ge,

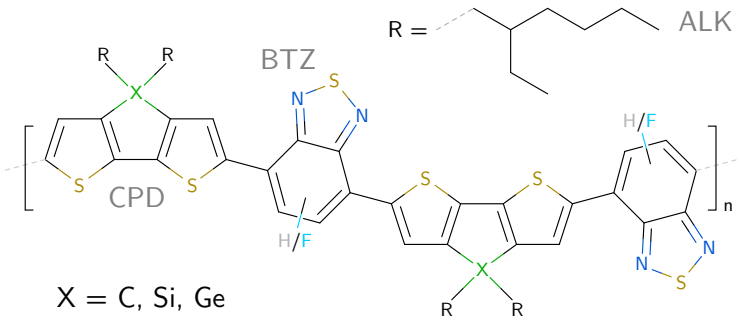

Figure 3.1: Chemical structure of P–X repeat unit and introduced residue names.

forming a sequence P–C → P–Si → P–Ge, while the BTZ (acceptor) unit is saturated with hydrogens and is the same for all three polymers. In the second series, one systematically varies the BTZ unit via fluorinaion in a sequence P–C → P–1F → P–2F, while CPD unit is identical for three compounds, and contains carbon (fig. 3.2). In both derivative families, an improved solar efficiency is observed (up to $6.5\ \%$), which is attributed to an improved morphologies [152–166], reduced band gap [21, 150–152, 154, 162, 164, 166–169] and altered mobilities [21, 41, 150, 152, 154, 156, 164–166, 168, 170, 171].

Within this setup and collected experimental data, I want to use a number of simulation techniques in a bottom-up scheme to address the following questions: How does the P–X chemistry give rise to its morphology? What is the charge transport and related properties in these morphologies? How do the substitution trends manifest themselves through morphology and charge transport?

In the following sections, accurate MD force fields are re-parameterized from first-principles calculations. They are verified through simulations of various crystals (polymorphs) of P–X polymers, which are observed experimentally. As a result, key parameters, contributing to crystal formation, are identified. The lamellar structures are then used to simulate charge energetics, couplings and hopping mobilities, which are then compared to experimental data.

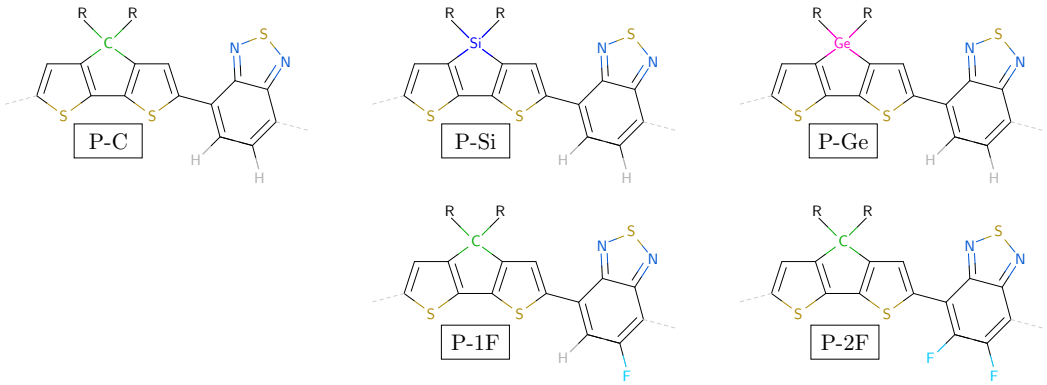

Figure 3.2: Five variations of PCPDTBT polymer and their labels.

3.2 Force field parameterization

Before one proceeds with simulations of atomistic morphologies, one needs a force field. In the case of new compounds such force fields do not exist and need to be developed (i.e. designed and parameterized). In order to simplify the procedure, one can adopt an existing force field and re-parameterize only a small number of relevant parameters. Often, they are partial charges and soft degrees of freedom (DOFs), such as dihedral potentials. In case of P−X polymers, new force fields are based on OPLS-AA, which provides functional forms of interactions and parameters for them, tuned to organic liquid simulations. In the following, the GROMACS 4.6.7 simulation package [172, 173] is used for a force field re-parameterization, as well as subsequent morphology simulations. First-principles calculations are performed in the Gaussian G09 simulation package [174].

To develop force fields for P−X polymers, their structure is subdivided into three units (i.e. residues). The two of them are BTZ and CPD (fig. 3.1), which comprise the backbone. Each has three variations due to chemical substitutions. Further, each CPD unit is grafted with two branched 2-ethyl-hexyl side-chains, which are described with a third residue, ALK. To simplify parameterization, a local mirror symmetry of CPD and BTZ units is employed via introduced symmetrized atom types (see fig. 3.3, a, fig. 3.4, a). The parameterization procedure was described previously, in Section 2.2.1.

Atom type	Si/Ge	Cα	S	N	H	F	CA	HA
σ [nm]	0.4100	0.3550	0.3550	0.3250	0.2420	0.2850	0.3500	0.2500
ϵ [kJ/mol]	0.5000	0.2929	1.0460	0.7113	0.1255	0.2552	0.2761	0.1255

Table 3.1: Lennard-Jones parameters adopted from OPLS-AA force field: Si - F for conjugated fragments and CA, HA for alkyl chains. Values for Si, Ge are obtained from CCSD calculations of small molecules.

Equilibrium geometries for P−X tetramers with truncated side-chains (R = C_2H_5 groups) are calculated at B3LYP/6-311g(d,p) level of theory and introduced into force fields. In the OPLS-AA force field, the Ryckaert-Bellemans functional form (eq. 2.16) is employed to describe torsional potentials. For P−X side-chains, this potential is insufficient for accurate parameterizations, because not one, but two side-chains are attached to the bridging atom X (see fig. 3.1). This results in a change of hybridization from SP_2 to SP_3 and in a shift of the potential's symmetry axis away from $\phi = 0$. This problem can be solved in two ways: Either to introduce the dummy atoms or to change the functional form of the potential to the one, which allows an arbitrary potential centering and form. Taking into account the molecules' structural complexity, the latter approach is adopted. For torsional potentials, Fourier expansions with an arbitrary cut-off (eq. 2.14) are employed to capture complex energy landscapes of the polymers.

Bonded potentials are complemented by the non-bonded interactions. One part of the non-bonded parameters, the Lennard-Jones constants, are adopted from the OPLS-AA force field. A complete list of van der Waals constants is given in (tab. 3.1) in two groups: Conjugated atom types (Si - F) and alkyl side-chain atom types (CA - HA), atoms $C\alpha$ represent all carbons in a backbone. Further more, the OPLS-AA force field does not contain parameters for atoms Si and Ge. Their values are fitted from distance-dependent energy profiles, calculated for small molecules (modified thiophenes) with CCSD/6-311+g(d,p) method in the co-facial

geometry. One could not fit the Lennard-Jones potential into the energy curves and obtain the corresponding parameters for Ge. Hence, parameters for Ge are set to Si values. This is a reasonable assumption, since atoms X in the bridging position exhibit mostly bonded interactions (with CPD unit and two alkyl side-chains), while the nearest non-bonded site in the π-stack is more than 0.7 nm away, where the van der Waals interactions are small, and is a consequence of alternating packing of P−X chains (see the morphology section 3.3). Electron densities, obtained from geometry optimizations, were used to fit partial charges. The missing first-shell element radius for Ge is set to 1.6 Å. For alkyl branched side-chains, bonded and non-bonded parameters are completely adopted from OPLS-AA force field.

3.2.1 Force field refinement

As was stated above, new potentials introduced into the P−X force fields need to be parameterized. These include inter-ring improper potentials and residue binding dihedral potentials. Additionally, DOFs related to substituted atoms X = C, Si, Ge (i.e. angles and impropers) are also re-parameterized.

Following the original parameterization scheme of OPLS-AA (and to reduce the computational time) a "divide and conquer" approach is used. In it, potentials are parameterized on small molecular fragments and then transferred into force fields of polymer chains. However, some potentials (connections between residues) are defined by the delocalized electron states. These potentials are optimized directly from whole-chain (tetramer) calculations.

The refinement scheme was described in Section 2.2.1. For the key degrees of freedom, QM and MD scans are performed, where MD potentials of interest are set to zero. At both levels of theory, potentials are restrained to a given DOF value, while the rest of the system is allowed to relax. The difference between two potentials is then fitted with a desired functional form and is introduced into the MD force field

$$\Delta U(q) = U_{QM}(q) - U_{MD}(q|C_\alpha = 0). \tag{3.1}$$

Here, q is an angle in angular, improper and proper potentials of P−X polymers. Fitting parameters C_α are defined by the functional form of a potential. In harmonic potentials the difference is fitted with a parabola $\Delta U(q) = \frac{k_q}{2}(q - q_0)^2$, where k_q is a spring constant and q_0 is an equilibrium value of the DOF. For dihedral potentials, the truncated Fourier series (eq. 2.14) is used, which contains C_n and $\phi_{0,n}$ fitting parameters. The scans are performed on CPD-X molecules with C_2H_5 side-chains and BTZ-Y molecules (all saturated with hydrogens; X = C, Si, Ge; Y = H/H, H/F, F/F). For each molecule a custom force field is prepared to perform the MD scan, while first-principles scans are performed at B3LYP/6-311+g(d,p) level of theory. For small molecular fragments, CPD and BTZ, harmonic potentials are shown in (fig. 3.5) and torsional potentials of side-chains are shown in (fig. 3.6).

Torsional potentials, connecting the residues are scanned on tetramer chains with B3LYP/6-311g(d,p) and fitted with an truncated Fourier series as well. During the scan, the soft dihedral potentials at equivalent positions are restrained to their equilibrium values. Obtained potentials are shown in (fig. 3.7). Fitted parameters are listed in (fig. 3.3, fig. 3.4) and

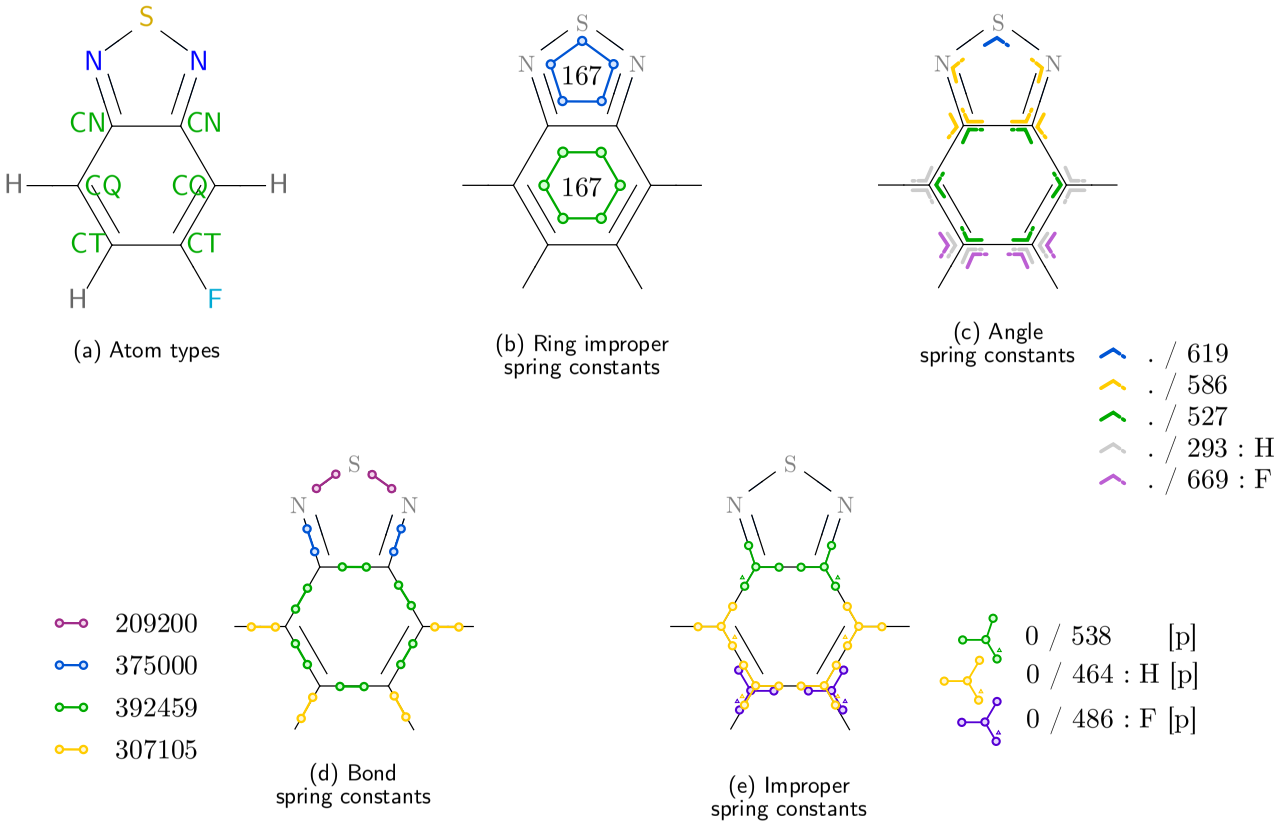

Figure 3.3: Parameters used in BTZ-Y (where Y = H, 1F, 2F) force field. Chemical structure and atom types are shown in (a). Spring constants for harmonic potentials: (b) ring impropers, (c) angles, (d) bonds and (e) other impropers. Parameters marked as [p] are re-parameterized from QM calculations. In-ring constants come from previous re-parameterizations. Values are rounded to first three meaningful digits.

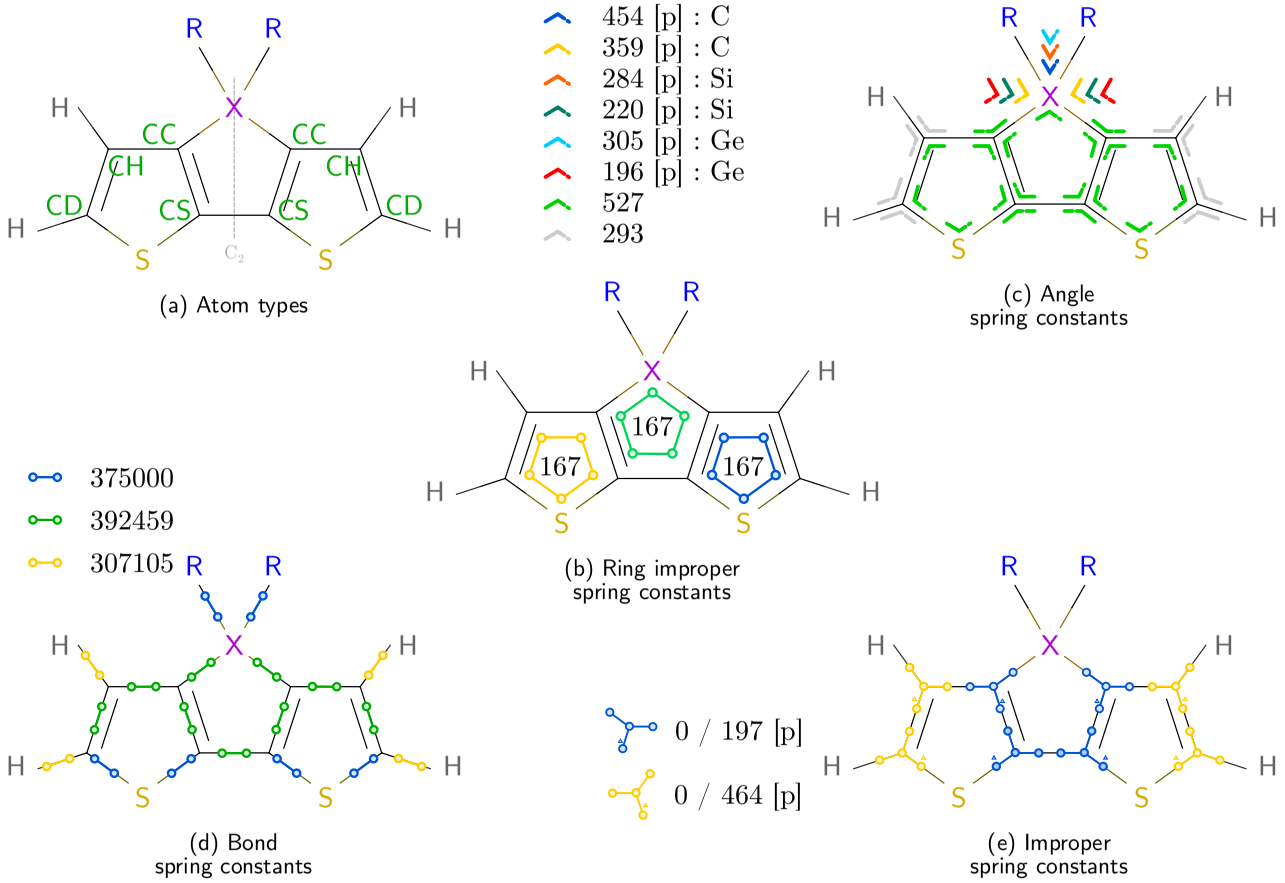

Figure 3.4: Parameters used in CPD-X (where X=C, Si, Ge) force field. Chemical structure and atom types are shown in figure (a). Spring constants for harmonic potentials: (b) ring impropers, (c) angles, (d) bonds and (e) other impropers. Parameters marked as [p] are re-parameterized from QM calculations. In-ring constants come from previous re-parameterizations. Values are rounded to first three meaningful digits.

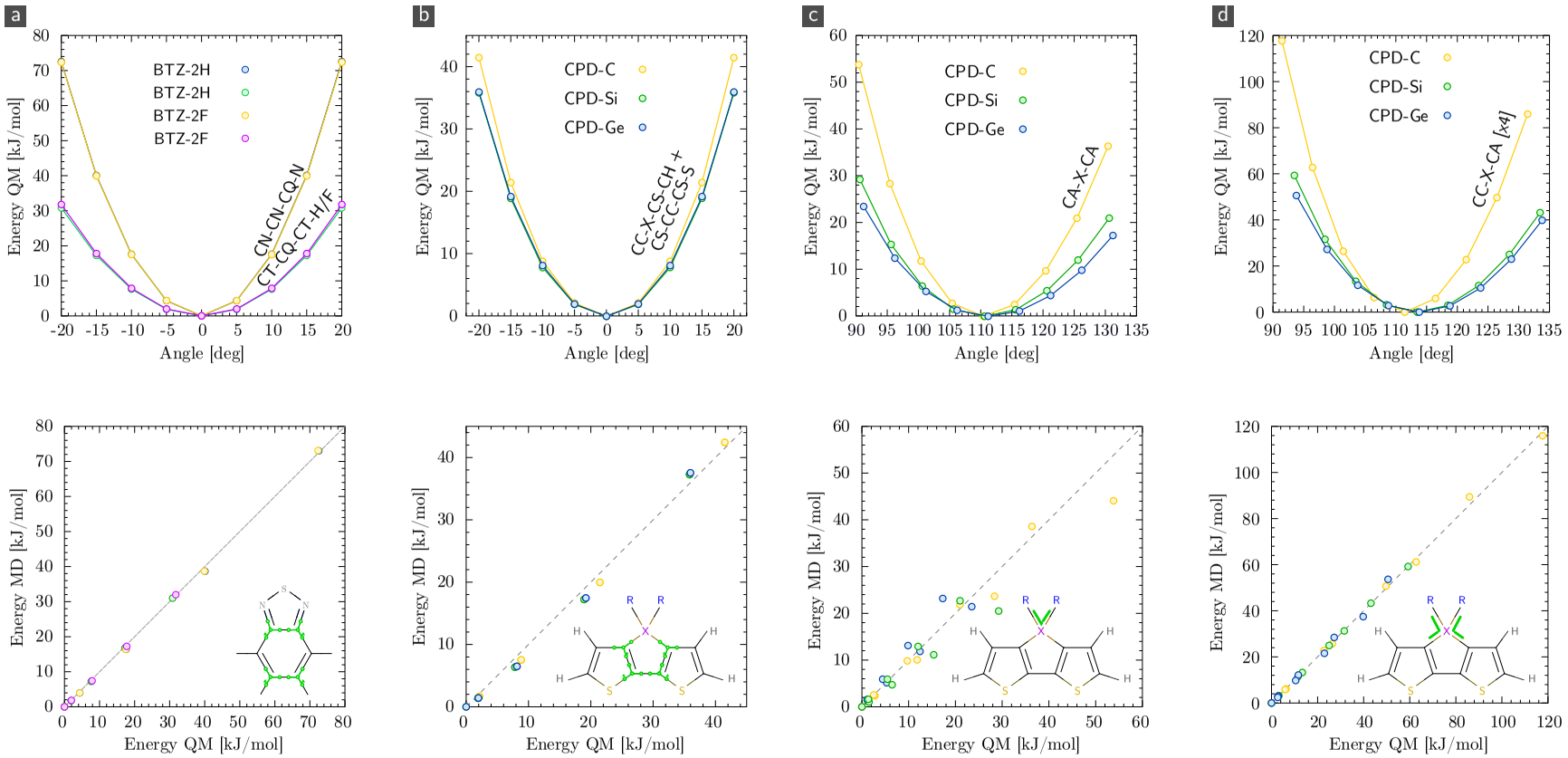

Figure 3.5: Re-parameterization of harmonic potentials: (a) improper dihedral potentials of BTZ, (b) improper dihedral potentials of CPD, (c, d) angular potentials of CPD. Top figures show potentials obtain from DFT calculations, bottom figures show correlation plots between QM and MD potentials after re-parameterization. Re-parameterized DOFs of molecular fragments are shown in the insets in green.

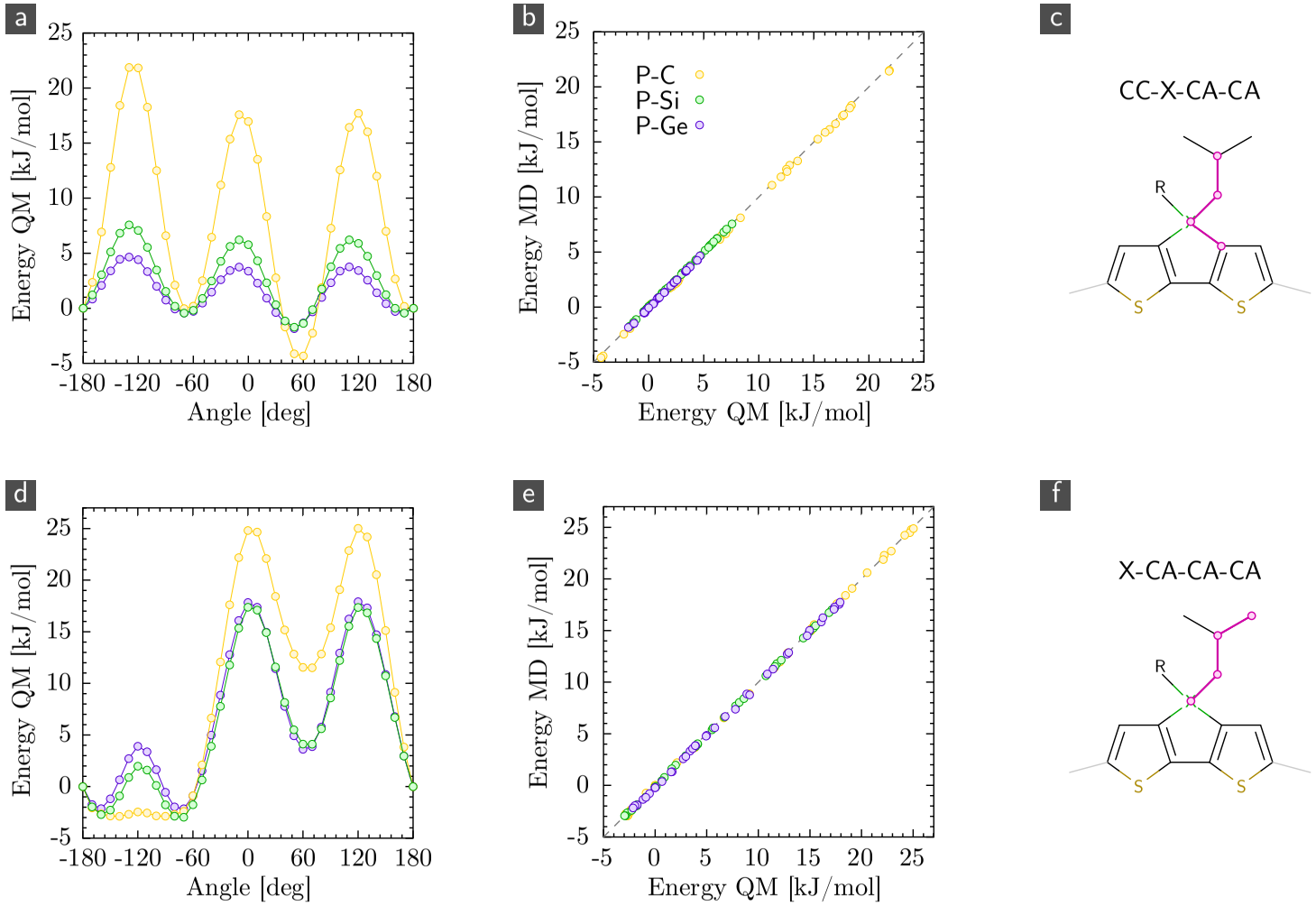

Figure 3.6: Potential energy curves from QM calculations for two bridging dihedrals: (a) CC-X-CA-CA and (d) X-CA-CA-CA; (b) and (e) are the correlation plots between QM and MD potentials after re-mapping; location of dihedrals in CPD unit are shown in figures (c) and (f).

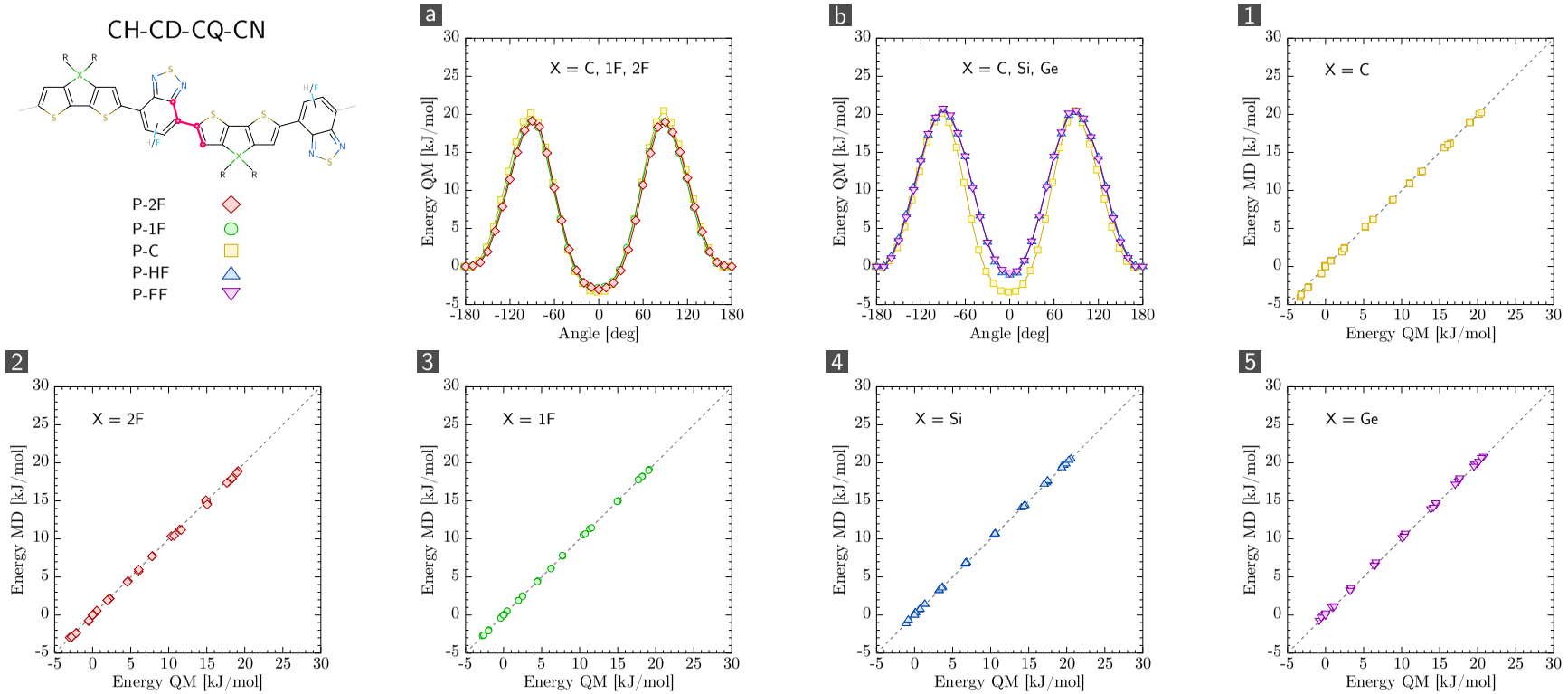

Figure 3.7: Potential energy curves from QM calculations of CH-CD-CQ-CN dihedral potentials, connecting BTZ and CPD units: (a) QM scans for X = C, 1F, 2F; (b) QM scans for X = C, Si, Ge. Panels (1) - (5) show correlation plots between QM and MD potentials after re-parameterization. Dihedral color-coding and location in the molecule is shown in the first panel.

n	(a) $\phi_{0,n}$	C_n	(b) $\phi_{0,n}$	C_n	(c) $\phi_{0,n}$	C_n	(d) $\phi_{0,n}$	C_n	(e) $\phi_{0,n}$	C_n	(f) $\phi_{0,n}$	C_n
1	55.64	-3.64	50.87	-1.28	48.98	-1.39	61.83	7.70	61.53	2.91	62.59	2.35
2	131.2	-0.51	109.3	-0.22	101.03	-0.21	126.4	-0.58	106.9	-0.31	118.2	-0.18
3	-13.59	6.57	-26.31	3.46	-390.7	2.21	8.98	3.67	7.43	3.29	6.27	3.25
4	26.10	-0.53	-16.24	-0.03	20.82	0.06	97.36	0.41	13.32	-0.06	31.02	-0.08
5	19.75	0.06	71.62	0.07	72.73	0.06	128.3	-0.40	133.0	0.15	136.3	0.51
6	1.13	0.12	-45.02	0.12	127.9	-0.06	23.32	0.29	14.26	0.21	1.12	0.12

Table 3.2: Fitted parameters for torsional potentials, connecting CPT unit and side-chains: (a) CC-CB-CA-CA, (b) CC-Si-CA-CA, (c) CC-Ge-CA-CA, (e) CB-CA-CA-CA, (f) Si-CA-CA-CA, (g) Ge-CA-CA-CA. See complementary plots in (fig. 3.6). Angles $\phi_{0,n}$ are given in [deg], constants C_n in [kJ/mol].

n	(a) $\phi_{0,n}$	C_n	(b) $\phi_{0,n}$	C_n	(c) $\phi_{0,n}$	C_n	(d) $\phi_{0,n}$	C_n	(e) $\phi_{0,n}$	C_n
1	0.03	-10.1	-0.16	-3.43	-0.20	-5.15	-0.05	-10.97	0.08	-11.44
2	0.05	-14.6	-0.17	-11.84	-0.05	-14.91	0.01	-13.69	-0.19	-13.69
3	1.72	-0.73	-5.36	-0.37	-180.9	1.03	0.36	-0.75	-0.19	-0.95
4	-0.15	1.32	-0.11	0.58	-12.16	0.18	-0.77	1.42	-2.37	1.40
5	-0.82	0.09	63.69	-0.04	41.98	-0.11	-9.91	0.07	-0.81	0.17
6	-8.36	-0.16	11.12	-0.12	-19.49	0.03	-15.03	-0.13	-190.2	0.10
7	8.12	-0.20	-37.33	-0.03	25.86	-0.10	-14.83	-0.16	-7.80	-0.16
8	-9.62	0.05	-35.10	0.11	-64.38	0.11	-1.58	0.11	10.33	0.11
9	-76.07	-0.05	-45.31	-0.01	-6.92	-0.03	-27.76	0.04	-24.59	0.04
10	47.80	0.00	-49.29	-0.02	47.77	-0.01	-64.29	-0.02	68.50	-0.04

Table 3.3: Fitted parameters for torsional potentials, connecting CPT and BTZ units: (a) X = C, (b) X = 1F, (c) X = 2F, (d) X = Si, (e) X = Ge. See complementary plots in (fig. 3.7). Angles $\phi_{0,n}$ are given in [deg], constants C_n in [kJ/mol].

in (tab. 3.2, tab. 3.3). Additionally, impropers are added to connect CPT and BTZ fragments. The force constants are similar for all five compounds: 450 kJ/mol/deg^2 for CQ-CN-CT-CD and 275 kJ/mol/deg^2 for CD-CH-S-CQ improper potentials. Provided the force fields, one can simulated atomistic morphologies of P−X polymers.

3.3 Morphology simulations: a bottom-up approach

Large elongated molecules, such as conjugated polymers, tend to form smectic phase[175, 176]. From this state, polymers can form morphologies with higher symmetry, such as crystals, by means of thermal annealing, solvent evaporation and other techniques[155, 177]. One of such morphologies, lamellae, is of particular interest for organic electronics applications[178–181]. In it, backbones stack on top of each other and form conducting channels with high charge mobilities. However, other ordered morphologies (i.e. polymorphs [182, 183]) are also possible. Their formation is strongly influenced by the side-chains [155, 165, 184–186].

After the force field is assembled, atomistic morphologies can be simulated and linked to charge transport properties[107, 108, 187, 188]. The moprhologies of P−X polymers and their consequence for charge transport properties were already addressed partially by means of QM and MM simulations [30, 156, 157, 189]. However, it is possible to go beyond the (anticipated) lamellar structures and construct morphologies in a systematic way. In the following, they are derived through analysis of single chain, dimer and tetramer interactions.

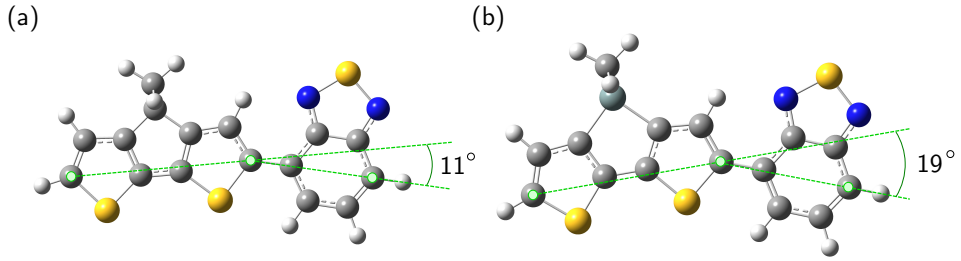

Figure 3.8: Backbone bending imposed by the bridging atom substitution: a) P−C, b) P−Si. Values are obtained from tetramer geometries, optimized at B3LYP/6-311g(d,p) level of theory.

Based on this information, various polymorphs of P−X polymers are derived and verified experimentally.

3.3.1 Monomer structure

One begins with monomer structure and interactions. Already at the level of individual monomers, one can observe the effect of heavy atom substitution. In a Si− and Ge− based polymers (see fig. 3.8) the X−C bonds are longer (1.53 Å vs 1.89 Å) due to larger size of the substituted atoms. This also causes an overall backbone bending between CPD and BTZ units. In C-bridged compounds, the bending angle is 11°, while in heavy-atom polymers it is twice as large 19°. Fluorination does not cause notable changes in polymer geometries.

Further, branched alkyl side-chains of P−X polymers are connected to the main chain via a bridging atom X and make the polymers soluble. Though conformations of side-chains are complex and extended, they can be divided into two groups with respect to how they modify interactions between two planar, co-facially aligned backbones. Such a division follows from a potential energy landscape of the bridging dihedral, which allows side-chains to rotate and take different conformations with respect to the backbone.

The energy profiles of bridging dihedrals, obtained from QM calculations and replicated in MD force fields, have three minima (see fig. 3.9, a). For different bridging atoms (X = C, Si, Ge), features of potentials remain identical, while heights of the barriers are reduced for heavier atoms. This is a consequence of elongated bonds and, hence, reduced steric hindrance between two side-chains and the backbone. The global minimum of the potential corresponds to side-chains folded onto the conjugated backbone (green side-chains in fig. 3.9, b), and the other two minima allow side-chains to be extended away from the backbone (blue side-chains in fig. 3.9, b). Because the two local minima lead to the same side-chain configurations with respect to the backbone, they are equivalent and treated as one state. This generates only two possibilities for planar backbones to interact: directly (side-chains are pushed out) or through alkyl chains (side-chains are crystallized along the chain). Here, crystallized chains imply that the majority of internal dihedrals are found in a trans state.

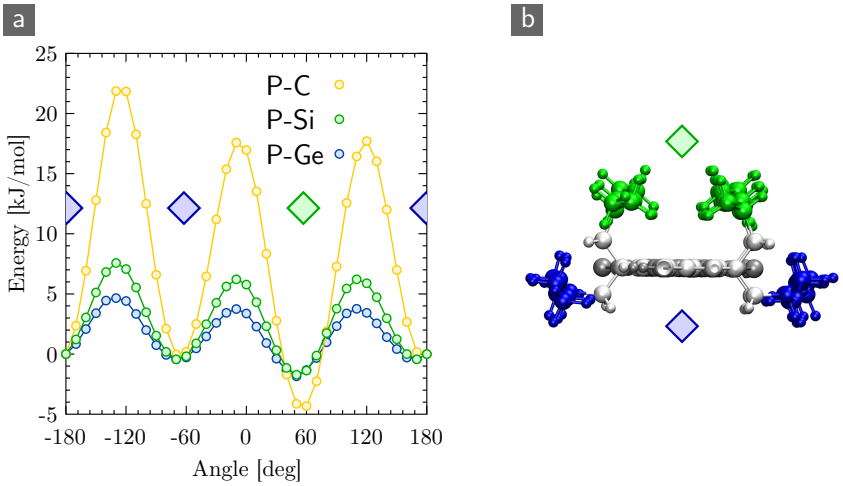

Figure 3.9: Side-chain conformations available in P−X monomers: (a) potential energy of a bridging dihedral with three minima, (b) monomer structure with two possible side-chain states. The color-coded diamonds relate side-chain conformations to energy minima.

3.3.2 Dimer interactions

Provided there are two ways for aligned backbones to stack, one can probe the potential energy of two chains as a function of their mutual position and find the energy minima, which may correspond to stable configurations.

To obtain such profiles, one considers a following setup. Molecular dimers are build out of two chains in a co-facial, alternated and aligned geometries, each having one of two possible side-chain configurations (see fig. 3.10, a, b). Here, alternation eliminates side-chain overlaps and reduces the number of calculations, as the number of points at which energies are evaluated is reduced by two. In the following, the dimer in (fig. 3.10, a) will be referred to as π-stacked dimer and the one in (fig. 3.10, b) as side-chain-mediated (SCM) dimer. Other geometries are not considered, as they are likely to lead to amorphous morphologies.

The separation (z-axis) as well as the lateral position (xy-plane) of centers of mass of two chains are varied. For a given dimer geometry in vacuum, an energy minimization and an SD simulation (for $t = 20$ ps at $T = 0.01$ K) are applied, while the backbone atoms are restrained and side-chains are allowed to relax. The goal of the SD simulations is to accelerate the equilibration of bulky side-chains and to collect statistics. Upon equilibration, one measures the non-bonded energy (i.e. Coulomb and Lennard-Jones contributions) of a dimer, as it defines the morphologies of weakly interacting organic compounds[11, 184].

In case of the π-stacked dimer, z-separation is varied between 0.24 nm and 0.5 nm (step 0.01 nm, xy-shift is 0.0 nm) and lateral shifts in the xy-plane are varied from -0.3 nm to $+0.3$ nm (step 0.05 nm, z-separation 0.4 nm) in both directions. Similarly, for the SCM dimer, z-separation ranges between 0.52 nm and 0.9 nm (step 0.01 nm, xy-shift is 0.0 nm) and lateral shifts range between -0.3 nm and $+0.3$ nm (step 0.05 nm, z-spacing 0.6 nm) in both directions. The results of such calculations are two cross-sections of a 3D interaction landscape and are shown in (fig. 3.10, c, d, e). For both side-chain configurations, only one minimum is observed. The π-stacked dimer's equilibrium geometry

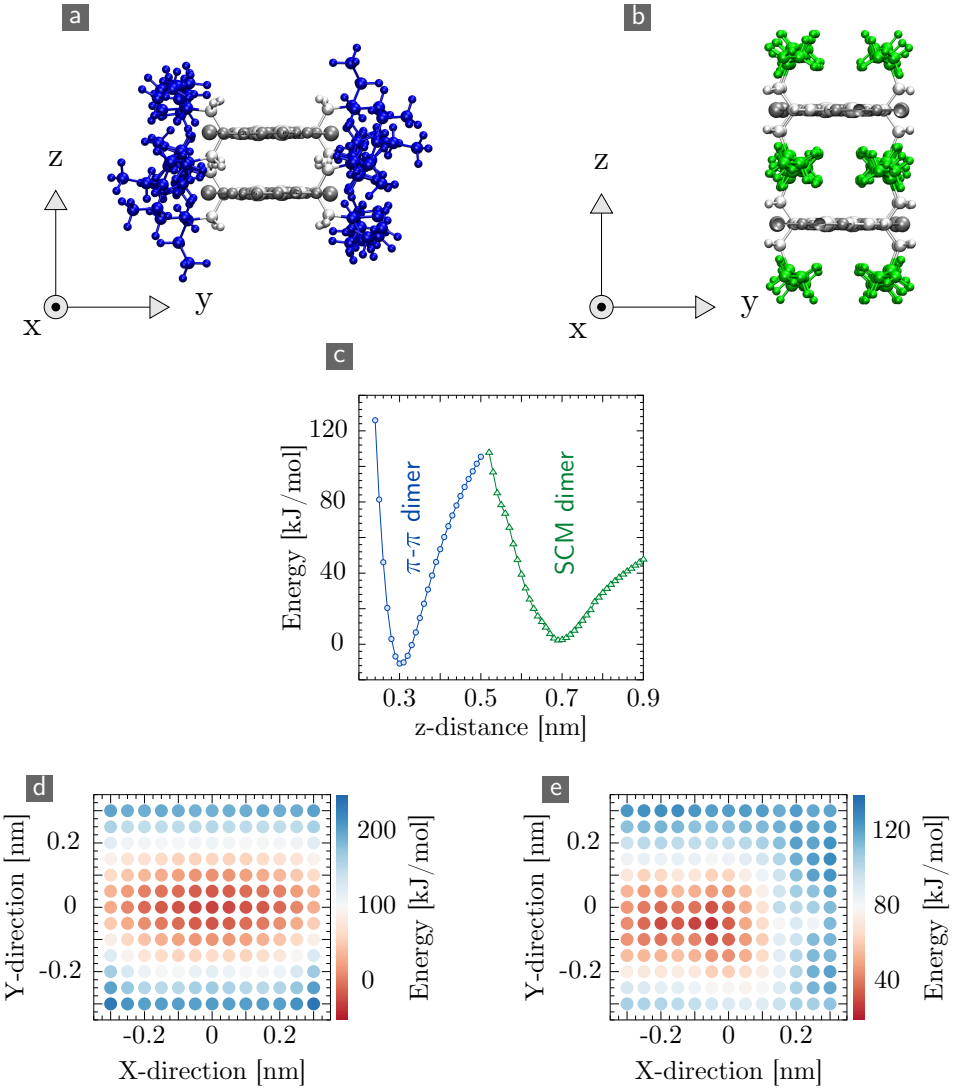

Figure 3.10: Dimers of P–X: (a) π-stacked dimer, (b) SCM dimer, (c) energy scan along z-axis at $x = y = 0$ nm (for two dimers), (d) xy-plane scan of π-stacked dimer at $z = 0.4$ nm, (e) xy-plane scan of SCM dimer at $z = 0.6$ nm. Error bars are much smaller than symbols.

is recovered at $\vec{r}_{eq} = (0, 0, 0.3)$ nm and the SCM dimer's equilibrium geometry is located at $\vec{r}_{eq} = (-0.2, -0.05, 0.7)$ nm. The shift is corrected in further calculations to reproduce $\vec{r}_{eq} = (0.0, 0.0, 0.7)$ nm equilibrium position.

The z-dependent energy of π-stacked dimer is much more narrow due to direct van der Waals interactions, while the SCM energy profile is broader due to flexible side-chains. Also, in all calculations the variation of the electrostatic contributions is small compared to the van der Waals energy of the system. Hence, in these polymers dimer morphologies are guided by the van der Waals interactions between two chains.

Equilibrium geometries provide starting conformations for further morphology construction. Using obtained data, one can build three dimers. The first two are shown in (fig. 3.10, a, b), where all side-chains are either amorphous (the π-stacked dimer) or fully crystallized (the SCM dimer). The third possibility is a π-stacked dimer with both crystalline *and* amorphous side-chains (the hybrid dimer), shown in (fig. 3.11, a). Because two backbones require side-chains in the same conformation (i.e. same color) in order to interact, the number of possible macroscopic, periodic assemblies is limited. The simplest two-dimensional structures (stacks), one can build, are [SCM-SCM]$_n$, [π-SCM]$_n$ and [π-π]$_n$ (also known as π-stack), where n is the number of repeat units in the stack. In the following, two morphologies containing crystallized side-chains are considered, and then the π-stacks (with disordered side-chains only) are discussed.

3.3.3 Morphologies with ordered side-chains

The morphologies, made of dimers with fully or partially crystallized side-chains, are examined in case of P−C polymer. A crystal, based on the SCM dimer (fig. 3.10, b), is constructed first. While it remains stable at low temperature (SD simulation), it is found in non-equilibrium state even for short simulation times (300 K, 1 ns). This is due to large fluctuations of flexible P−X backbones. Better results are obtained with the hybrid dimer (fig. 3.11, a). In this case, backbones are found in pairs, which are more stable.

Polymer-X	a [nm] sim.	exp.	b [nm] sim.	exp.	c [nm] sim.	exp.	c/b sim.	exp.
P−1F	2.40	2.32	2.20	2.06	1.17	1.10	0.53	0.53
P−C	2.46	2.36	2.08	1.93	1.25	1.24	0.60	0.64

Table 3.4: Simulated and experimental parameters of orthorombic unit cells of MSD-based crystals. Relative error $\sigma/\mu \leq 0.001$. Vectors a, b, c correspond to axes x, y, z.

Provided that equilibrium geometries in the π-stack are known from previous dimer calculations, the relative location of two stacks is not. To find it, similar calculations are done for two stacks in PBC at 300 K. The high temperature is needed to allow amorphous chains to adapt. The positions of two stacks are varied in two directions (xz-plane) between -1.2 nm and $+1.2$ nm (the length of one P−C repeat unit) and y-separation 1.2 nm. The resulting non-bonded energies are shown in (fig. 3.11, b). From the profile, one discovers four minima, symmetrically located around axis $z = 0$ nm. Because of the symmetry, the minima pairs are equivalent. The global minimum is found at $\vec{r}_{eq} = (0.2, 1.2, 0.6)$ nm. The sample geometry is then equilibrated (1 ns at 300 K, NPT ensemble). The resulting crystal is shown in (fig. 3.11, c) and labeled No. 1.

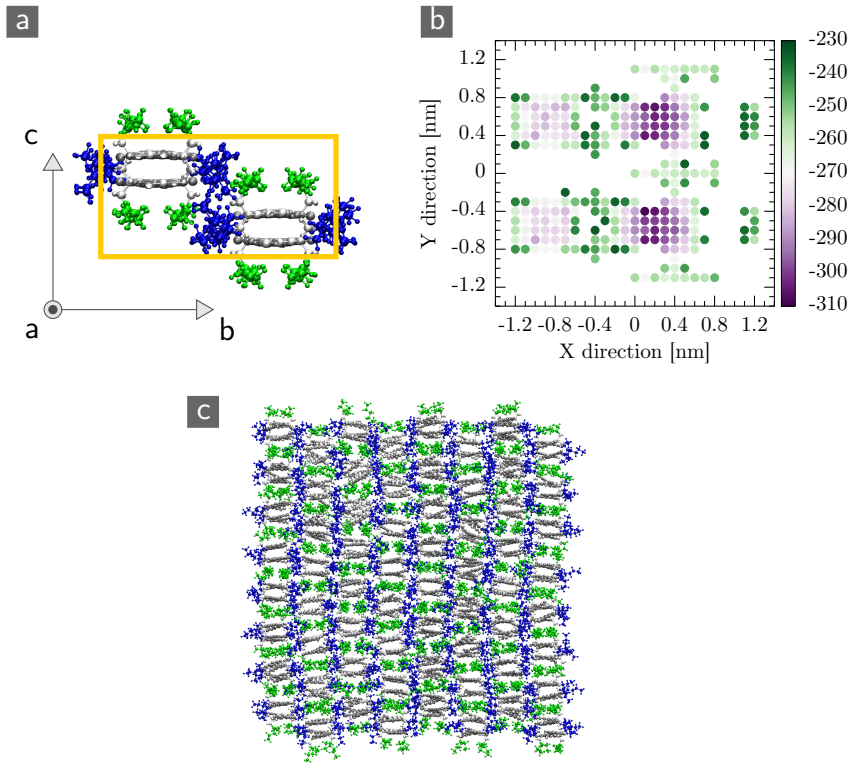

Figure 3.11: SCM-based crystal of P−C (No. 1): (a) unit cell, (b) xz-plane scan at $y = 0.6$ nm, (c) snapshot of a crystal with 128 molecules.

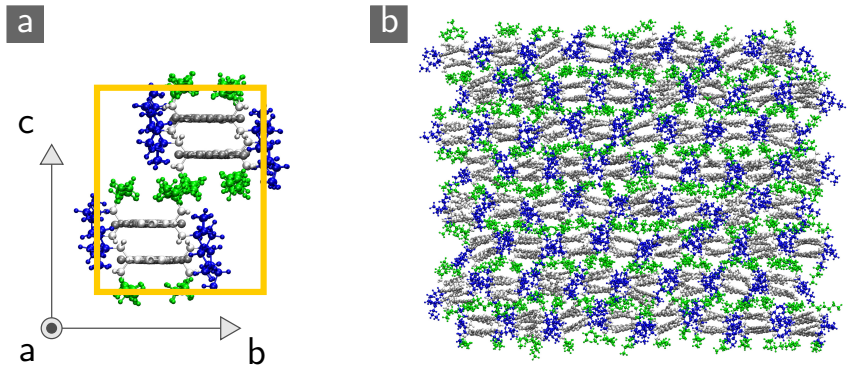

Figure 3.12: SCM-based crystal of P−C (No. 2): (a) unit cell, (b) snapshot of a crystal with 128 molecules.

The second morphology has more complicated structure due to strong dimer interdigitation in the unit cell, and cannot be obtained from energy scans, as previously. The unit cell is guided by the experimental data, where backbone positions were reconstructed from GIWAXS measurements. The side-chain positions are then set manually to minimize the volume of the cell. Resulting unit cell and equilibrated crystal are shown in (fig. 3.12, a, b) and labeled No. 2.

The unit cell parameters from two equilibrated morphologies are listed in (tab. 3.4) and compared to the experimental data[153, 155]. The simulated intermolecular distances (hence, unit cell parameters) are systematically larger than those in the experiments, due to OPLS-AA parameterization of van der Waals constants. The introduced error is of the order of $\epsilon \leq 7\%$. To compare with experiment, one compares the ratios of two box dimensions (c/b). This ratio has an order of magnitude lower error due to an error cancellation. The simulated crystal (No. 1) was observed for P$-$1F polymer, which is structurally identical to P$-$C. From a good ratio match, one concludes that the unit cell is correct. The simulated crustal (No. 2) was observed for P$-$C polymer. The ratio match is not exact, but still is well reproduced within the 7% error. A failure to reproduce exact packing of side-chains along the y-axis results in expansion in this direction and larger b value of the unit cell. A proper packing would decrease the value of b and elevate the ratio to 0.64, measured experimentally.

Once again, one should note that available scattering data for C-bridged P$-$X polymers suggest two morphologies. These two observed peaks, which are often attributed to inter-lamellar spacing, are more likely to represent the two unit cells, obtained previously. Crystals No.1 and No.2 are observed individually (depending on solvents used) and converting from one to another upon annealing [152–160]. In many publications, a unit cell vector that is greater than ≈ 4 Å is often attributed to inter-lamellar distance in a π-stack. However, one should be more careful in interpreting the available structural data, as in the case of C-bridged P$-$X polymers multiple polymorphs are present. Further improvements of side-chain packing can be obtained, for example, from biased Monte Carlo simulations to sample the configuration space of bulky side-chains more effectively [190].

An important observation is that in all experimentally verified and successfully simulated crystals not a single chain, but a dimer is a building block of the crystals[155]. Each obtained unit cell contains a pair of (π-stacked) dimers (i.e. four chains), interactions between which are modified via different side-chain packing.

The above morphology calculations are twofold. They show that polymorphs can be derived in a systematic way, following a limited number of parameters, such as mutual position and orientation between the structural blocks, as well as side-chain's dihedral state. But more importantly, they prove the capability of derived classical P$-$X force fields to reproduce a complex structure of P$-$X systems. This allows to make the next step and derive lamellae of P$-$X, which will be used for charge transport simulations. The SCM-containing structures are out of the scope of charge transport simulations, as side-chains screen the transfer integrals in all (two) directions, along which hopping transport is possible.

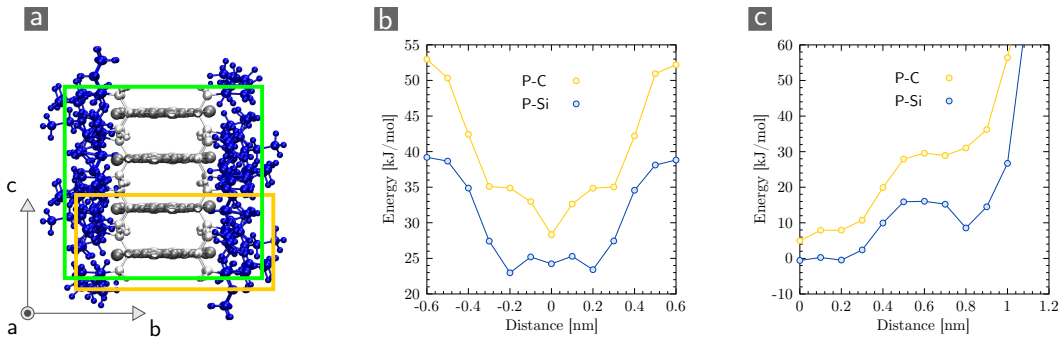

Figure 3.13: (Two) π-based crystals of P−X: (a) unit cells, (b) x-axis dimer energy profile at $z = 0.4$ nm, (c) x-axis tetramer energy profile at $z = 0.8$ nm. Error bars are estimated from ten simulation runs and are much smaller than symbols.

3.3.4 Lamellar morphologies

The idea of dimers as building blocks applies to π-stacked morphologies as well. Following the way of deriving initial conformations from energy scans of non-bonded interactions between blocks, one recovers that not one, but two π-stack conformations are possible for each P−X polymer.

To begin, one checks the interactions of two chains in vacuum (π-stacked dimer), following the protocol of dimer scans, outlined above. In this case one is interested in x-direction, as interactions in other two dimensions are known. The result is shown in (fig. 3.13, b) and is a cross-section of previous dimer calculations in (fig. 3.10, d) at $y = 0$ nm. It reveals a unique minimum within the repeat unit length (1.2 nm), which in turn corresponds to the least overlap of side-chains in an alternating dimer geometry. Two characteristic curves are shown for X = C, 1F, 2F and for X = Si, Ge. Due to larger size of heavy atoms and longer bonds, side-chains are pushed further away from backbones and allow a broader range of equilibrium backbone configurations. The region is reduced for C-bridged polymers due to strong side-chain repulsion.

Of greater interest are interactions between dimers, as they proved to play an important role in structures of SCM crystals. Similarly to a single dimer calculations, one can look at interactions of two dimers in a vacuum along the main axis (x-coordinate, separation $z = 0.8$ nm). The result is shown in (fig. 3.13, c) for two representative examples, P−C and P−Si. The global minimum corresponds to a typical π-stack, obtained from dimer stacking. However, an additional minimum is revealed for P−Si and a plateau region for P−C polymers at $x = 0.8$ nm. The barrier between two peaks is 5 kJ/mol per polymer chain, which is sufficient to trap the structure for a sufficiently long time. Similarly to SCM structures, the unit cells of all P−X lamellae contains four chains (i.e. a pair of dimers). The global minimum configuration has two chains in the unit cell, while the shifted one contains four. Two unit cells of P−X in π-stack are shown in (fig. 3.13, a).

For further discussions, structure corresponding to the *global* minimum will be referred to as *G*-stack. The other minimum, which permits *shifted* dimer conformations will be referred to as *S*-stack. Both are sketched in (fig. 3.14, a), while a snapshot of the simulation box is shown in (fig. 3.14, b).

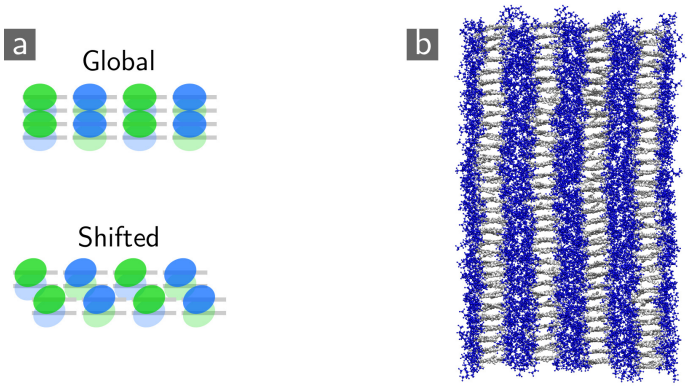

Figure 3.14: (Two) π-based crystals of P−X: (a) schematic packing of dimers in unit cells, (b) snapshot of the (G) crystal with 128 molecules. The (S) crystal is similar to (G) crystal and is not shown.

	Global			Shifted		
Polymer-X	a [nm]	b [nm]	c [nm]	a [nm]	b [nm]	c [nm]
P−2F	1.247	1.577	0.396	1.240	1.669	0.382
P−1F	1.247	1.596	0.392	1.233	1.675	0.380
P−C	1.249	1.603	0.389	1.232	1.667	0.379
P−Si	1.257	1.703	0.375	1.256	1.760	0.366
P−Ge	1.254	1.730	0.374	1.252	1.787	0.366
P−Si (exp)	–	1.680	–	–	1.680	–
P−Ge (exp)	–	1.720	–	–	1.720	–
directions	*repeat unit len.*	*inter-lam.*	*π-π dir.*			

Table 3.5: Simulated and measured parameters of orthorombic unit cells of five P−X polymers in two π-stacks: Global (*G*-stack) and shifted (*S*-stack) conformations. Relative error is $\sigma/\mu \leq 0.001$. Vectors a, b, c correspond to axis x, y, z. Experimental are taken from [164].

Hence, for five P−X systems one can construct two different π-stacked configurations (i.e. ten different configurations). Using the initial guess for unit cells of these systems, super cells of 128 chains are assembled (4 lamellae $\times$ 32 molecules), equilibrated at 300 K in NPT ensemble for 1 ns and used to generate 1 ns production runs (NVT ensemble for 1 ns 300 K). All equilibrium unit cell parameters are listed in (tab. 3.5).

In conclusion, constructed force fields are structurally accurate and reveal multiple P−X polymorphs, which include, but are not limited to, π-stacked mesophases. It was shown that all crystalline morphologies of P−X polymers are built of dimers, as single chains are too flexible and cannot facilitate the crystallization. Simulated crystals were confirmed experimentally [164], comparison is given in (tab. 3.5).

These crystallization patterns are traced back to a few key properties of P−X polymers. Side-chains are found in two states only, which dictate two types of interactions between backbones. Combined with alignment, it allows to stabilize two chains in a unique π-stacked dimer, which inherits the binary interactions of single chains. One interaction type leads to multiple π-stacked morphologies, while the other generates a number of side-chain mediated polymorphs, none of which are typically assumed for organic electronics applications.

A special remark should be made about assumptions made during the conformational search in tetramer calculations: Co-facial crystals are often observed experimentally and

are expected, while a non-cofacial packing is likely to lead to amorphous morphologies in the absence of backbone/side-chain support. Hence, the search was limited to co-facial dimer and tetramer geometries. And yet, non-cofacial crystals in P−Si polymers were observed experimentally [163]. The resulting crystals are known as cross-hatched and form an overlapping triclinic network, in which backbones of two consecutive layers form an angle ca. 50°. Since P−Ge equilibrium geometry is identical to the one of P−Si polymer, it should be capable to form such networks as well. Within the assumption of co-facial interactions, such crystals could not be obtained from simulations.

As a next step, one proceeds with charge transport simulations. In the following, only (G) and (S) π-stacked atomistic morphologies will be used. In simulated crystals No. 1 and No. 2, side-chains screen backbone pairs. Because transfer integrals scale as $\exp(-\alpha r)$ with the distance between two molecules, their values will be extremely low, making hopping charge transport in these crystals unlikely.

3.4 Charge transport simulations

The charge transport in P−X lamellae is studied within Macrus charge transfer theory, which introduced previously in Section 2.4.3. Within this approach on needs to evaluate rates of the charge transfer events as [117, 118]

$$\omega_{ij} = \frac{2\pi}{\hbar} \frac{J_{ij}^2}{\sqrt{4\pi\lambda_{ij} k_B T}} \exp\left[-\frac{(\Delta E_{ij} - \lambda_{ij})^2}{4\lambda_{ij} k_B T} \right], \tag{3.2}$$

which relies on microscopic parameters, such as reorganization energies λ_{ij}, transfer integrals J_{ij}, site energy differences E_{ij}. In the following, one calculates and analyzes these parameter for 10 systems (five P−X polymers in two stacked morphologies). Simulations are done in the VOTCA simulation toolkit [84, 125], while related quantum-chemical calculations are performed in the Gaussian G09 simulation package [174].

3.4.1 Reorganization energies

Reorganization energies and ionization potentials are calculated in a harmonic approximation from four single point QM calculations for five tetramers in vacuum. Upon geometry optimization at B3LYP/6-311+g(d,p) level of theory, one calculates four energies (using the same method), i.e. E_0^0, E_1^1, E_0^1, E_1^0 . Here, E_g^c is the energy of a molecule in state c, while its optimized geometry corresponds to state g. Indices c, g can take two values: State 0 (the ground state) and state 1 (the cation state with charge $+1$). Using these four values, one calculates relevant parameters for charge transport simulations: ionization potential I, reorganization energies upon charging $\lambda^{(ch)}$ and discharging $\lambda^{(dc)}$. They are obtained as

$$I = E_1^1 - E_0^0, \quad \lambda^{(ch)} = E_0^1 - E_0^0, \quad \lambda^{(dc)} = E_1^0 - E_1^1, \tag{3.3}$$

From small molecule simulations, such as AlQ_3, it is expected that the distribution of reorganization energies has much smaller width (0.03 eV) than the energetic disorder (width of side-energy distributions)[84]. It will be shown that in P−X polymers energetic disorder is ≥ 0.13 eV. Hence, reorganization energies can be replaced by their mean. In this case it is approximated by a value, obtained from first-principles calculations. The calculated values are listed in the table (tab. 3.6).

System	P−C	P−1F	P−2F	P−Si	P−Ge
I	5.2465	5.3239	5.4672	5.3373	5.3028
$\lambda^{(dc)}$	0.0947	0.0941	0.0876	0.1001	0.0996
$\lambda^{(ch)}$	0.0886	0.0875	0.0820	0.0947	0.0944

Table 3.6: Ionization energies and reorganization energies, evaluated for P−X polymers. Values are given in units of [eV].

The calculated reorganization energies are similar for five P−X systems and are close to 0.1 eV. Highest λ values are found in heavy atom polymers P−Si and P−Ge, which is attributed to the largest changes in their wave functions and geometries upon charging. The observed values for five systems fall into a general trend, observed for conjugated semi-crystalline polymers (such as P3HT and PBTTT [107, 108]) with reorganization energies ca. 0.1 eV, which is typically smaller than analogues quantities for small molecules ($0.2 - 0.4$ eV) [191].

3.4.2 Transfer integral distributions

The second component, required by the Marcus rate expression are transfer integrals, also known as electronic coupling elements. The transfer integrals are calculated using the dimer projection method [138], described in the Simulations methods chapter. The transfer integral is calculated as a projection of a dimer Hamiltonian onto two localized monomer orbitals as

$$J_{ij} = \langle \phi_i^{(m)} | H_d | \phi_j^{(m)} \rangle \,, \tag{3.4}$$

where H_d is a dimer Hamiltonian and $\phi_i^{(m)}$ is a localized monomer single-particle state. Hence, for each coupling, one requires two monomer and one dimer calculations. For hole transport one is interested in couplings between two localized HOMO (highest occupied molecular orbital) levels. The transfer integral evaluation time scales as $O(N)$ with the number of molecules in the system. Due to linear packing of polymer chains in a π-stack the scaling prefactor is unity. Even then, calculations are time consuming since couplings are sensitive to the local environment and must be calculated for each pair individually, where each molecule contains hundreds of atoms. Because of the required quantum chemical calculations, transfer integral evaluation is the bottle neck of the method.

First, one is interested in transfer integral values between two P−X bacbkones as a function of a relative shift. Results for two polymers are shown in (fig. 3.15), where chains are planar and optimized at B3LYP/6-311g(d,p) level of theory, while transfer integrals are calculated with a reduced basis set (B3LYP/6-31g). Couplings of P−1F and P−2F are similar

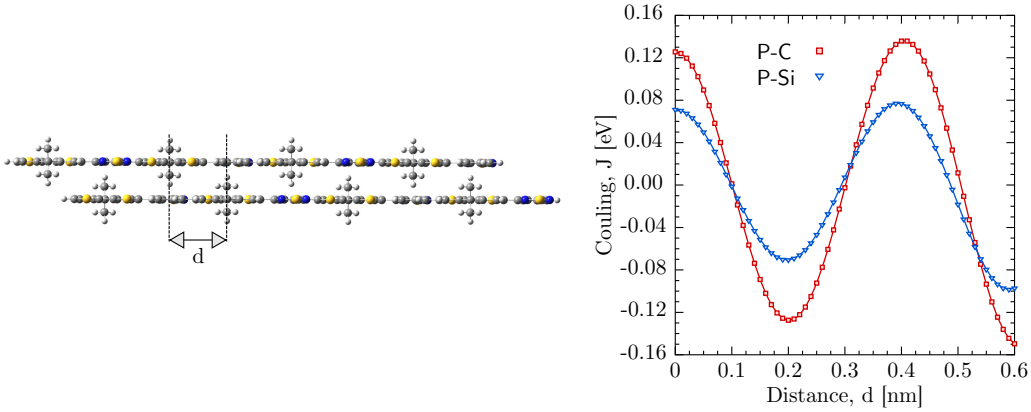

Figure 3.15: Transfer integrals as a function of relative shift of two P−X chains in a co-facial geometry (X = C, Si). Side-chains are replaced with methyl groups. Values for X = 1F, 2F, Ge are not shown due to similarity.

to P−C values, while couplings of P−Ge are similar to P−Si. For this reason, curves of P−1F, P−2F, P−Ge are not shown. Similar geometries of backbones result in a similar shpape of the curves. The maximum coupling value at $d = 0.0$ nm for the P−C polymer is 0.14 eV, while for P−Si it is two times smaller (0.07 eV). This decrease is explained by a stronger bending of P−Si backbone, which increases the distance between CPD units in a dimer and effectively reduces the wave function overlap. Next, one is interested in how these couplings are modulated by the polymer morphologies.

As noted before, quantum-chemical calculations are time consuming. In case of P−X tetramers, one requires ca. 7 hours of computer time on 16 core machines at B3LYP/6-31g level of theory to obtain a single J value. Assuming that one requires 12 hours to assess couplings within one snapshot of MD trajectory (i.e. 128 molecules and 128 couplings), it would take over 7 weeks to evaluate couplings for 10 snapshots within 10 systems. If one aims at quick pre-screening of compounds for various applications, such long simulation times are prohibitive. A common choice to speed up coupling evaluation would be to use semi-empirical methods, such as ZINDO [128]. However, the method is parameterized for a limited number of elements, which does not include Si, Ge, F. As a result, it cannot be used for four out of five P−X systems. Implementing and parameterizing these methods for new elements and compounds would be of great use [192, 193] and should be considered in the future work.

A compromise can be found at the border between a computationally demanding dimer projection approach and semi-empirical methods, like ZINDO. A success of semi-empirical methods holds on a number of approximations, one of which states that

$$J_{ij} = \frac{\beta_i + \beta_j}{2} S_{ij} = \beta_{ij} S_{ij}, \tag{3.5}$$

where J_{ij} is the transfer integral between states i and j localized on two different sites, S_{ij} is the overlap matrix and β_{ij} is the system specific constant, often called the resonance integral[130]. According to this expression, the distance and orientation dependence of couplings can, to a certain extent, be approximated by the overlap matrix S_{ij}. As a follow up,

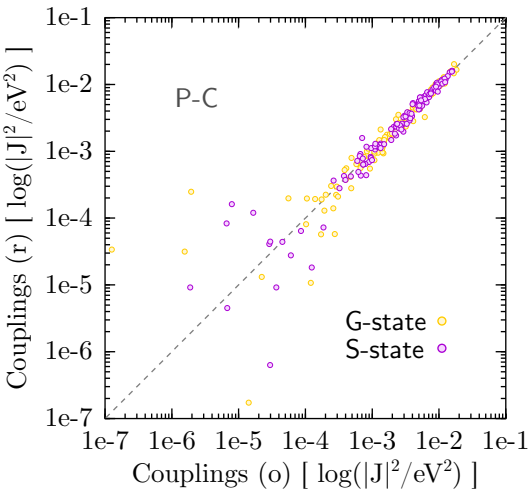

Figure 3.16: Comparison of couplings, evaluated at B3LYP/6-31g level of theory (o), and rescaled couplings, obtained from HF/3-21g calculations (r). Values are collected from one snapshot of P−C in two morphologies: *G*-stack and *S*-stack.

coupling trends obtained from two different methods should be reproduced up to a scaling constant α as

$$|J_h|^2 = |J_l|^2/\alpha. \tag{3.6}$$

Here, J_h and J_l are couplings calculated within more accurate (higher) and more rapid (lower) levels of theory. The squares are introduced to eliminate the mismatch of phases, often observed for different methods. This expression is well reproduced for small molecules [194, 195] for both electron and hole transfer reactions. In the following, it will be shown that the equation still holds for extended conjugated systems, such as conjugated polymers.

Here, I use rescaling to reduce the cost of transfer integral calculations. For each system, 11 snapshots are extracted from 1 ns production trajectories (i.e. 100 ns apart). The first snapshot is then used to calculate couplings using two methods: A chosen reference B3LYP/6-31g calculation and a much faster HF/3-21g (here, HF stands for closed shell Hartree Fock) method. Using the HF method in a lower basis set reduces the calculation time by more than a factor of 7. The resulting two sets of couplings are then used to deduce the scaling factor α via a linear fit of the correlation data. As mentioned in Section 2.1, because of the sign problem and because Marcus rates depend on $|J_{ij}|^2$, the square values are used to conduct the fits. The result of such re-scaling is shown in (fig. 3.16) for two sample distributions of P−C in *G*-stack and *S*-stack. Deviations at low coupling values can be attributed to a small basis set size and imprecise mapping, provided by the overlap matrix S. Even then, the rescaling captures trends in electronic couplings well and can be used to speed up the coupling element evaluation. A complete list of scaling constants α is given in (tab. 3.7). The quantum-chemical calculations are done in Gaussian09 simulation package, while couplings are evaluated using a DIPRO module of the VOTCA simulation package.

Parameters α have similar values for five polymers, which are larger than one, hence, rescaled couplings are always lower than those from HF calculations. For the remaining 10

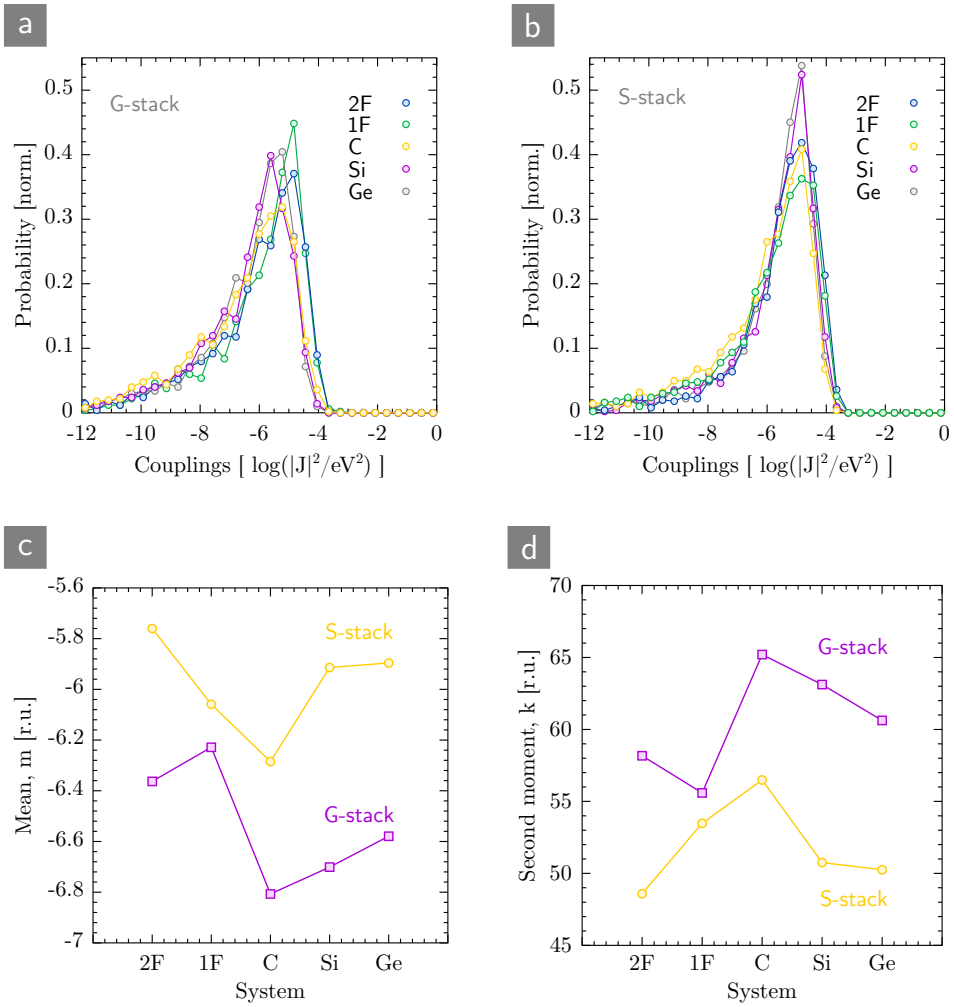

Figure 3.17: Distribution of integrals for P−X polymers in *S*-stack (a) and *G*-stack (b). Statistical properties of the distributions: Means (c) and second moments (d). See text for details.

System	P−C	P−1F	P−2F	P−Si	P−Ge
α_G	1.7892	1.5991	1.6435	1.8732	1.7422
α_S	1.9337	1.7285	1.6012	1.8210	1.7129

Table 3.7: Rescaling constants between J^2 values obtained from B3LYP/6-31g and HF/3-21g methods, subscripts G and S refer to respective π-stacked morphologies.

snapshots, transfer integrals are evaluated only at a lower level of the theory and re-scaled with established constants. The resulting coupling distributions are built for five polymers in two π-stacked morphologies and are shown in (fig. 3.17, a, b). All calculated distributions are noisy due to relatively small statistics (i.e. 1280 points from 10 snapshots per trajectory). In terms of the distributions, the introduced scaling factors result in a relative shift, while the shapes are preserved.

One compares distributions through their unique moments. In case of coupling distributions, the mean m and the second moment k are calculated as

$$m = \int_{-\infty}^{0} x f(x) dx \tag{3.7}$$

$$k = \int_{-\infty}^{0} (x - m)^2 f(x) dx, \tag{3.8}$$

where $f(x)$ is the probability distribution function, defined on the semi-infinite interval $(-\infty : 0]$. The evaluated means and second moments are shown in (fig. 3.17, c, d). In real distributions, $-\infty$ is never reached due to finite sampling and is replaced by the lowest value in a set R_{min}. Parameter k is a measure of localization (width) of the distribution.

As expected, transfer integrals in morphologies exhibit different trends as compared to ideal dimer calculations (fig. 3.15). Because of smaller inter-molecular (π-stacking) distances in the S-stacks, couplings are systematically higher than those in the *G*-stack (fig. 3.17, c). Also, distributions are more narrow in case of *S*-stack, as can be seen from second moments' data, presented in (fig. 3.17, d). From two plots one concludes that in the *G*-stack, couplings follow patters 1F $\rightarrow$ 2F $\rightarrow$ C and Ge $\rightarrow$ Si$\rightarrow$ C (with the highest couplings in P−1F). In the *S*-stack the two sequences are 2F $\rightarrow$ 1F $\rightarrow$ C and Ge $\rightarrow$ Si $\rightarrow$ C (where the highest couplings are found in P−2F polymer).

3.4.3 Site energy distributions

Site-energies of holes in P−X systems are calculated in a perturbative scheme

$$E^{(i)} = I^{(i)} + E^{(i)}_{el} + E^{(i)}_{pol}, \tag{3.9}$$

where $E^{(i)}$ is the total energy of the charge on a site i, $I^{(i)}$ is the ionization potential of a chain in vacuum, $E^{(i)}_{el}$ and $E^{(i)}_{pol}$ are electrostatics and polarization corrections due to the

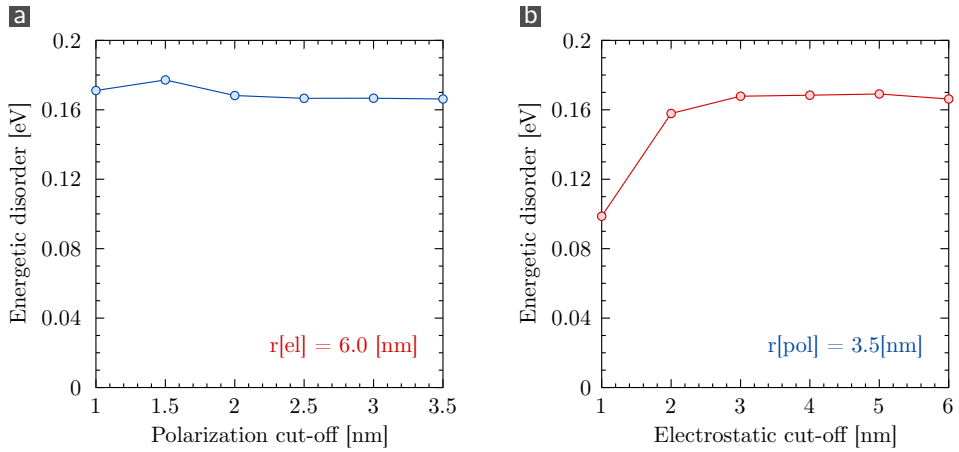

Figure 3.18: Energy disorder as a function of polarization (a) and electrostatic (b) cut-offs. Calculations are done for P−Si, assembled in a G-stack morphology. The insets show the value of second radius, which was held constant during calculations.

presence of environment (i.e. morphology). The polarization contribution is evaluated with the Thole model. Fitted partial charges are obtained as described in the force field development Section 3.2. Partial charges for the remaining side-chains are adopted from OPLS-AA force field for alkanes. At the linking point where carbon atom of the chain is replaced with a hydrogen, a sum of OPLS-AA and QM charges is used.

Isotropic polarizabilities α for elements C, N, S, H are adopted from the AMOEBA polarizable force field [83]. The missing polarizabilities for atoms F, Si are calculated from isolated atom B3LYP/6-311+g(2d,2p) single point calculations, while polarizability of Ge is set to Si value due to similar electronic structure. Additionally, a dummy atom type X with zero polarizability is introduced in VOTCA package for side-chain atoms, as their partial charges already include the polarization effects. A complete set of polarizabilities is given in (tab. 3.8). Finally, the universal damping factor of 0.39 is used in the Thole model.

Because electrostatic interactions are pair-wise, the energy calculation time scales as $O(N^2)$, where N is the number of charged sites in a system. The scaling is reduced to linear if two cut-offs for electrostatics and polarization (r_e and r_p) are introduced.

E	C	N	S	H	F	Si	Ge
$\alpha \times 10^{-3}$	1.334	1.073	2.926	0.496	0.440	3.962	3.962

Table 3.8: List of polarizabilities α used for energy calculations in P−X systems, values are given in units [nm^3].

The two cut-off values are determined from the cut-off dependent energy calculations of P−Si polymer in the *G*-stack morphology (see fig. 3.18). Because site-energies in organic materials are Gaussian distributed, cut-offs are determined from regions where the site-energy statistics does not change. Because Marcus charge transfer rates depend only on site energy differences, in single component systems the mean energy is redundant. Hence, cut-offs are determined from regions of a constant width of energy distributions (i.e. constant energetic disorder). In case of P−Si, the energetic disorder saturates after $r_e = 2.5$ nm and

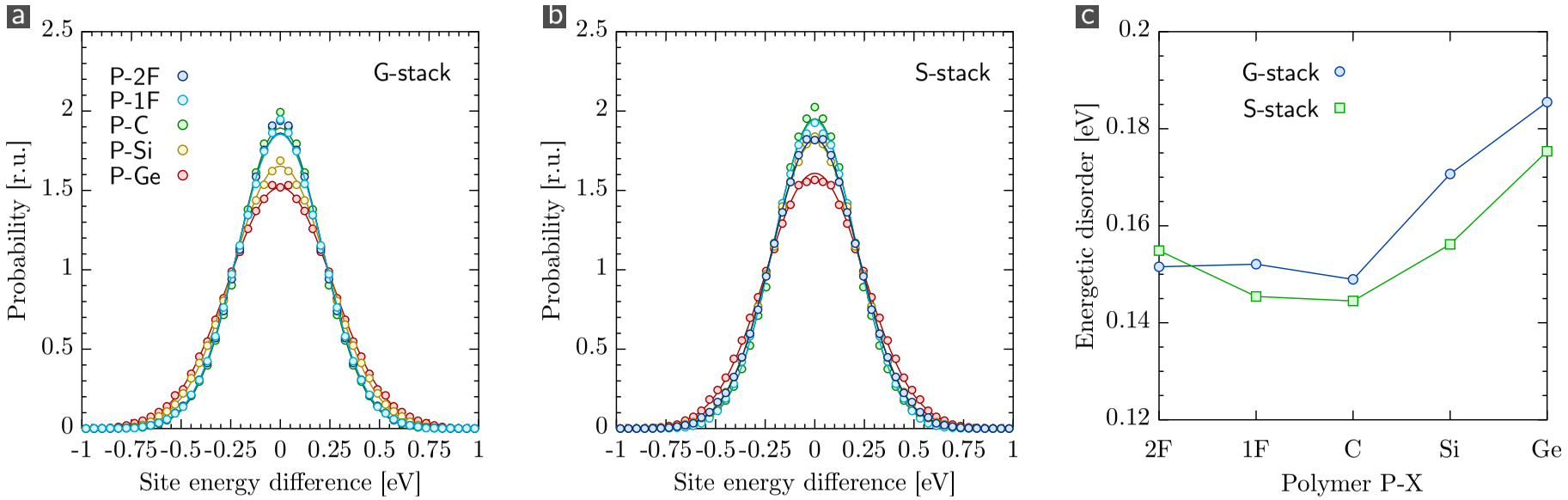

Figure 3.19: Site energy difference distributions of five P−X polymers (X = 2F, 1F, C, Si, Ge) in the *G*-stack (a) and *S*-stack (b) morphologies (as bullets), fitted Gaussian distributions are plotted as solid lines. Energetic disorder values, extracted from fits, are shown in plot (c).

$r_c = 3.0$ nm. For the following calculations higher values of $r_e = 3.0$ nm and $r_c = 4.0$ nm are chosen.

Site energies are calculated for five P−X polymer systems (X = 2F, 1F, C, Si, Ge) in two morphologies (*G*-stack and *S*-stack). For each system, ten snapshots are extracted from 1 ns production run trajectories (100 ns apart), resulting in 1280 energy point per system. To refine the statistics, energy differences are calculated and plotted in (fig. 3.19, a, b). As anticipated, energies are Gaussian distributed.

Energy disorder values (i.e. the widths of energy distributions) are extracted from corresponding Gaussian fits. In accordance with the addition law of Gaussian distributed variables, the resulting widths gain a factor of $\sqrt{2}$. Rescaled accordingly, energy disorder values in all systems are plotted in (fig. 3.19, c).

In organic electronics, one is interested in materials with low energetic disorder, which is necessary for high carrier mobilities. In case of P−X polymers, morphologies with the shifted π-stack have systematically lower energetic disorder. In both S- and G- stacks, the original P−C polymer has the lowest energetic disorder values (0.14 eV and 0.15 eV). Further, the substitution trends are clearly reflected in the energetics of P−X systems. In both cases (heavy atom substitution in CPD and fluorination of BTZ), the energetic disorder is increased upon substitution. However, the effect of heavy atom substitution is more pronounced, leading to values of 0.18 eV and 0.19 eV (up to 25%), as compared to fluorination, which generates a mild increase in the energy disorder (0.16 eV and 0.15 eV, i.e. up to 7%).

It is surprising, however, that the energetic disorder in these polymers is more than three times higher than the values observed with the same method in other semi-crystalline polymers, such as P3HT and PBTTT [107, 108]. For the two, an identical value of $\sigma = 0.05$ eV was recovered. In fact, the energy disorder of P−X polymers is close to the one of amorphous AlQ_3 (0.17 eV) [114]. The difference between these polymers and the P−X family lies in the presence of amorphous side-chains and DA-like electrostatics. Hence, it is interesting to assess the effect of these two quantities on the energetics of P−X polymers.

3.4.4 Origins of energetic disorder

From energy distributions obtained for P−X systems, energetic disorder is more than 0.14 eV. This value is three times larger than values obtained for P3HT and PBTTT crystals (0.05 eV). Because the high energetic disorder will manifest itself in low mobilities, one is interested in the origins of the energetic disorder in P−X polymers.

Energetic disorder stems from molecules' orientations, electrostatics (i.e. partial charges) and polarizabilities. Effects of polarization on energetic disorder are known and of no interest: It provides a small reduction of energetic disorder due to screening. Next, while positions of molecules in a morphology also cannot be changed, one can continuously modify partial charges on backbones and side-chains to trace the effect on charge energetics in the system.

In the following, the P−Si polymer in a *G*-stack will be investigated. To decompose the energetic disorder with respect to polymer chain components, one follows the scheme,

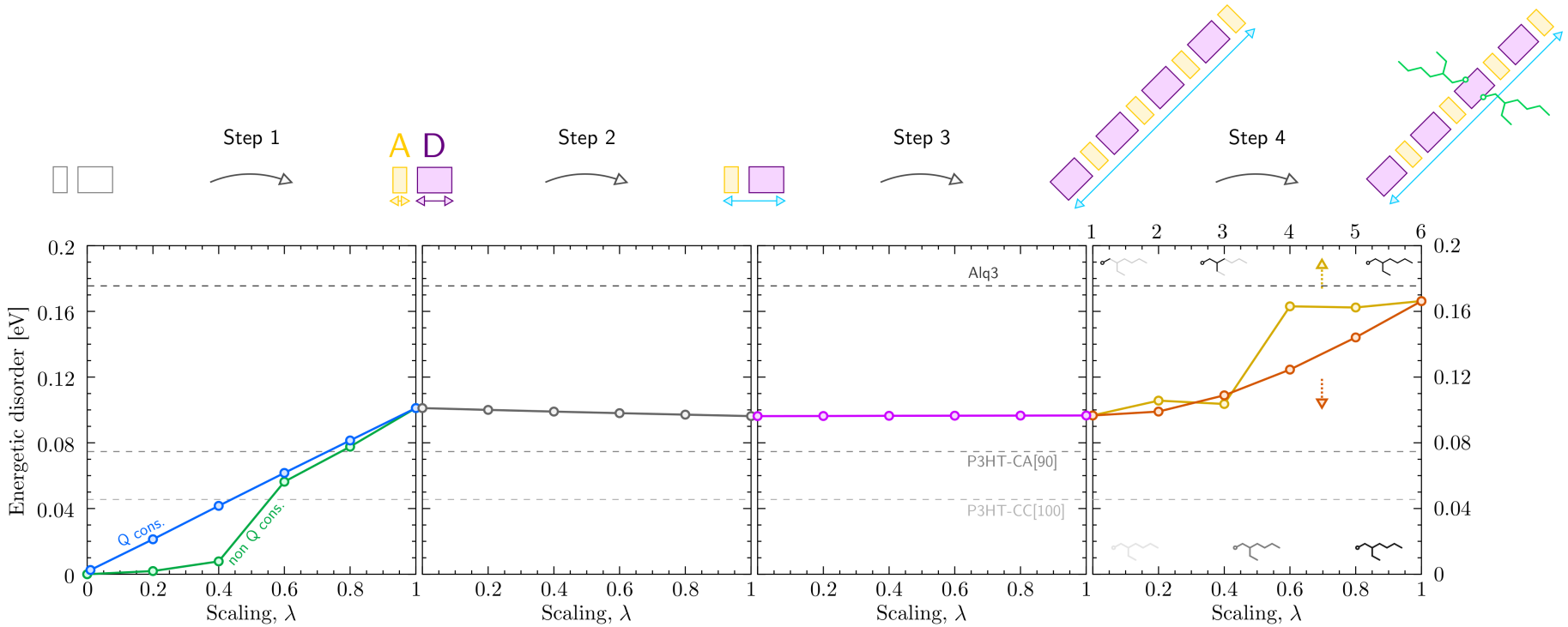

Figure 3.20: Energy disorder upon inclusion of charge transfer effects (CT): local CT (a), donor-acceptor CT (b), intra-molecular CT (c); as well as an effect of disordered side-chains (d) via scaling parameter λ. Insets in figures (a), (b), (c) show ranges of charge transfer. Upper axis in figure (d) counts the number of CH_n groups attached to the backbone in a growth scheme. Upper inset in figure (d) shows side-chains' inclusion in a growth scheme, lower inset shows side-chains' inclusion in a uniform scaling scheme. Reference values are shown for ideal P3HT crystal (P3HT-CC[100]), crystal with defects (P3HT-CA[90]) and amorphous Alq3 [114, 191].

shown in (fig. 3.20). In it, two structural parts are considered: Side-chains and backbones. On side-chains' charges are strongly localized, while on a backbone charges are delocalized, i.e. there are charge transfers and non-zero dipole moments present. Hence, the electrostatic contribution of the backbone is separated into additional steps, which include charge transfer due to DA architecture and charge transfer due to polymer conjugation (i.e. along the entire chain).

In the first step (see fig. 3.20), no charge transfer between donor and acceptor units is considered. The hole is assumed to be delocalized over the backbone, hence, each residue holds $1/8$ of a charge in the excited state (and zero in the ground state). This is done via a linear transformation of charge values, which satisfy the restraint. Partial charges of side-chains are set to zero. Then, partial charges on backbones are continuously switched on via a scaling factor λ as $q_i(\lambda) = q_i\lambda$, where $\lambda = 1$ recovers the electrostatics of individual backbone fragments. The result is shown as a green curve in (fig. 3.20, Step 1).

The used scheme has a defect: When the charges are switched off, the excited state represented by the electrostatics with the total charge $+1$ cannot exist. This discrepancy is attributed to the step-like behavior of the energetic disorder. A better way is to restrain the total charge in the excited state to $+1$ for each value of λ. As a result one obtains a continuous, almost linear behavior of energetic disorder on the scaling parameter λ.

In the absence of side-chains' electrostatics as well as charge transfer due to DA architecture and other charge transfer effects, one can see that the internal electronic structure of donor and acceptor units are responsible for up to 0.1 eV of energetic disorder. This is already twice as much, compared to values observed in P3HT and PBTTT polymers. This can be linked to the fact that on the bridging atom (where side-chains are connected to a backbone) more than $+1$ [e] of charge is localized, while in the other two polymers such high charge values are never reached.

In the second step, the charge transfer within the DA repeat unit will be introduced and continuously switched on in a scheme, similar to the previous ones. The result is shown in (fig. 3.20, Step 2): A mild decrease of the energetic disorder. Further, in step three (see fig. 3.20, Step 3), the initial charge distribution of the backbone is re-introduced, where non-nearest neighbors charge transfer is present. This leads to no changes in terms of energetic disorder.

One concludes that, in π-stacked P$-$X the local electronic structure of backbones' repeat units is responsible for half of the energetic disorder in the system. Dipole moments, stemming from local and global charge transfers in the system, seem to play a minor role for the energetic disorder in P$-$X systems.

The final, fourth step turns on the side-chain interactions (fig. 3.20, Step 4, orange curve). This causes a second increase in the energetic disorder up to 0.17 eV, which is four times larger than the values in PBTTT and P3HT crystals. In these calculations, the dependence of disorder on the scaling parameter λ is close to quadratic. The origin of such increase is a disordered structure of side-chains which generate random local electric fields. The effect was observed previously: Introduced thermal and regioregularity defects in P3HT crystals cause increase of energetic disorder from 0.05 eV to 0.08 eV [107].

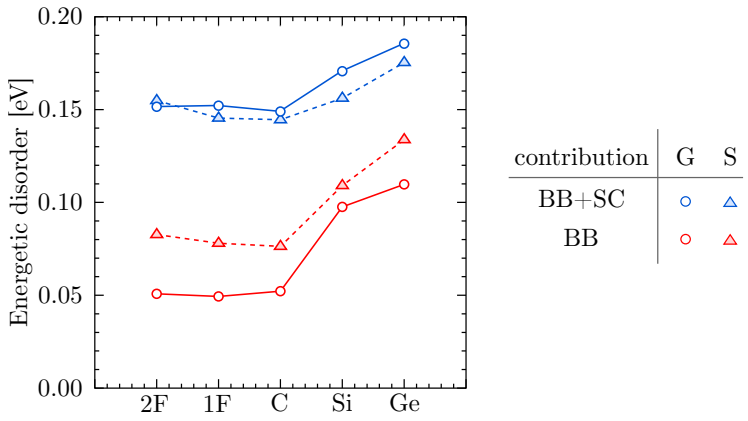

Figure 3.21: Energetic disorder in five P−X polymers in two π-stack morphologies with and without side-chains. Here, BB stands for backbone, SC for side-chain, G for *G*-stack, S for *S*-stack.

More insight can be obtained if charges of side-chains are not modified simultaneously, but in a sequential way. In these calculations interactions of the charged groups are modified along the side-chain growth direction (fig. 3.20, step 4, yellow curve). For a given n, first n side-chains moieties have proper charges, while the remaining moieties have no charges. No side-chains correspond to the case $n = 1$, while fully grown chains are $n = 6$. Within such a *growth* scheme, energetic disorder exhibits a jump after $n = 3$ of introduced moieties. This jump can be attributed to the local structure of side-chain components: The first three CH_n groups are well ordered with respect to backbones, while the remaining in-bulk parts are disordered.

The above conclusions are only qualitative. The data are collected from 10 snapshots along 1 ns production run. This time is not enough to fully sample bulky side-chains, hence sampling and contribution to the energetic disorder is incomplete. A set of energy disorders with and without side-chains is shown in (fig. 3.21), which is the last ingredient needed for charge transport simulations.

3.4.5 Mobilities

Because of broad distribution of available experimental data [21, 41, 150, 152, 154, 156, 164–166, 168, 170, 171], mobilities are calculated with and without energetic disorder, which emulates different carrier concentrations in a system. For each snapshot 128 KMC runs are conducted, and mobilities are calculated as averages over 1280 runs in ten snapshots for any given system. The external field is in these calculations is set to 10^6 V/m, which matches typical fields in organic solar cells. The results of calculations are shown in (fig. 3.22).

In the no-disorder case, mobilities are similar for all systems (ca. $1 \cdot 10^{-1}$ cm^2/Vs) and correlate with experimental data in OFET devices. This is because they are defined by transfer integral distributions, which are very similar in five systems. Trends in coupling distributions can be tracked in values of mobilities. The *S*-stack mobilities are systematically higher than those in *G*-stack due to higher couplings. Within the *G*-stack, highest mobilities are in P−1F and P−Ge, while in the *S*-stack the best mobilities are observed in P−2F and

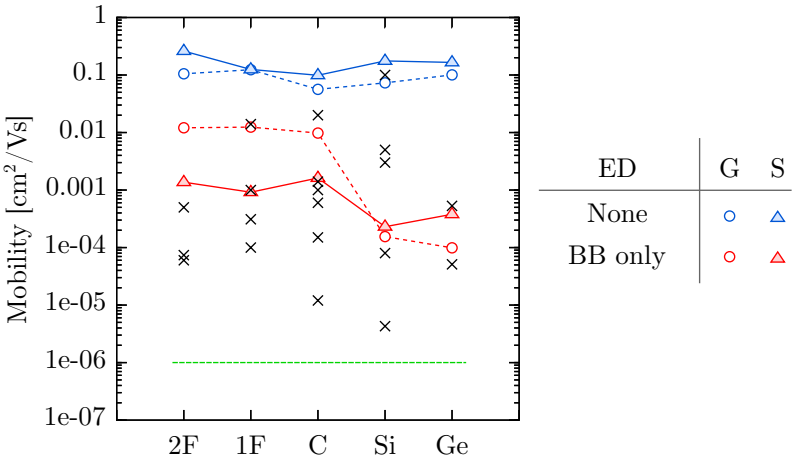

Figure 3.22: Simulated mobilities in five P−X polymers: values obtained without energetic disorder (blue) and with backbone energetic disorder (red). Simulations were performed in *G*-stack (G) and *S*-stack (S) morphologies. Horizontal line (green) marks an estimate for mobilities with backbone and side-chain contributions to energetic disorder. ED stands for energetic disorder, BB for backbone.

P−Si. In both geometries P−C polymers generates the lowest mobility values due to low transfer integrals, as compared to all other compounds.

Unfortunately, because of large energetic disorder, KMC simulations require long simulation times to converge. For this reasons, the mobility calculations are done for backbone electrostatics only, while side-chains are excluded. In the presence of disorder, mobilities are defined by charge energetics. In both G- and S- stacks, the highest mobility is found in the P−2F polymer. The lowest values are in P−Si and P−Ge polymers, for which the combined effect of backbone and side-chains electrostatics leads to the most unfavorable charge transport conditions. The deviation of P−Ge mobility in the S-stack can result from too short simulation times in KMC runs.

Because energetic disorder in P−X polymers with side-chains is comparable to those in amorphous compounds, KMC simulations give only an upper limit on mobility values in these polymers, which is $1 \cdot 10^{-6}$ cm^2/Vs.

Experimentally, mobility values range between $1 \cdot 10^{-5}$ cm^2/Vs and $1 \cdot 10^{-1}$ cm^2/Vs [21, 41, 150, 152, 154, 156, 164–166, 168, 170, 171]. Though measurements agree with simulations, without morphology measurements it is difficult to judge on a relative quality of P−X polymers for solar applications. Interestingly, in the experiment one observes same mobilities in π-stacked and SCM-based crystals, i.e. charge transport is equally effective in both crystalline morphologies. In the SCM-based crystals, it is likely that the transport is happening along the chain, while in the π-stack the dominant mechanism is hopping. In this sense, one cannot compare mobilities in various P−X systems due to their different origins.

3.5 Conclusions

In this chapter, properties of five PCPDTBT derivatives (P−X: X=C, Si, Ge, 1F, 2F) with branched 2-ethylhexyl side-chains were investigated. Upon atom substitution, observed electronic properties of the polymers are modified: band gap, mobility and overall solar cell performance. A combination of MD simulations, first-principles calculations and the Marcus charge transfer theory was used to address the relationship between the polymer chemistry, electronic properties, underlying morphologies of the polymers and mobilities, as a function of atom substitution.

An accurate molecular force field was based on the OPLS-AA and derived from first-principles calculations. A proper dihedral parametrization was shown to be crucial for proper morphology simulations, including the role of chiral symmetry of bridged side-chains.

Atom substitutions P−C $\rightarrow$ P−1F $\rightarrow$ P−2F do not cause significant changes in the molecular geometry. In systems P−Si and P−Ge, large atoms cause bond elongation between backbone and side-chains. This enhances the bending within the backbone and pushes the side-chains away from the conjugated core.

Through analysis of inter-molecular interactions, multiple crystalline morphologies were obtained in a systematic way. At the level of individual molecules, the two-state bridging dihedral was linked to two unique interactions mechansims: Direct backbone-backbone and side-chain mediated. This allows a construction of two unique dimers. These dimers are found to be the building blocks of all P−X crystalline morphlogies, as single chains are too flexible and cannot facilitate the crystallization. The key points of P−X crystallization are (in order of morphology formation): presence of two-state bridging dihedrals, chain dimerization and second-to-nearest neighbor (i.e. dimer-dimer) interactions.

From *side-chain* based dimer interaction, one arrives at two crystal structures. Each contains two dimers in a unit cell, i.e. four molecules. The *backbone-based* interactions allow two π-stacked morphologies, whose unit cell contains one and two dimers. All four polymorphs were verified against the experiment and are in excellent agreement with available data. The fifth, cross-hatched polymorph of P−X could not be obtained due to restricted setup of the search protocol.

Interactions between molecules, dimers, tetramers and higher-level structures were probed through finite temperature energy scans, which provided good initial guess for the following level of morphology building.

Though all P−X polymers are capable of derived crystalline morphologies, experimentally polymers P−C, P−1F, P−2F are mostly found in side-chain mediated crystals, while P−Si and P−Ge for π-stacks only. This can addressed to the effects of the bridging atom: C-based polymers exhibit high steric hindrance between side-chains, which prevents the formations of structures higher than the dimer. On the other hand, ideal side-chain length allows them to crystallize along the backbone and form the above mentioned side-chain based morphologies. In the heavy substituted compounds, a combination of broad backbones and low barriers in a dihedral favors the lamellar structures.

In order to study charge transport, transfer integrals and energy differences were calculated for P−X polymer in two π-stack morphologies. One stack promotes high couplings in P−1F and P−Ge polymers, while the other in P−2F and P−Ge.

The energy distributions are calculated for all polymers and correspond to high energy disorder values, $\sigma > 0.14$ eV. This is much higher than in typical semi-crystalline polymers, such as P3HT and PBTTT, and is comparable to values in amorphous compounds such as AlQ_3. Such high disorder originates the electrostatics of CPD-BTZ repeat units, as well as disordered structure of side-chains. Further atom substitution leads to energy disorder increase. Bridging atom substitution amplifies the electric field fluctuations, with P−Ge producing the highest possible disorder of 0.19 eV. Fluorination leads to a mild increase of the energetic disorder with P−2F polymer reaching 0.16 eV.

As a result of high energy disorder, overall mobilities of P−X compounds are estimated at $1 \cdot 10^{-6}$ cm^2/Vs. Such low value is a direct concequence of the high energetic disorder in the systems. In the absence of side-chains, where energetic disorder is decreased, highest mobilities are obtained in fluorinated compounds and lowest in P−Si and P−Ge, which is a direct consequence of their energetics. In the absence of disorder, one finds similar mobilities in all five compounds $\mu = 1 \cdot 10^{-1}$ cm^2/Vs due to similar coupling distributions.

Though simulated mobilities fall within the observed experimental values, one should note that the origin of mobilities can be different. In π-stacks of P−Si and P−Ge it is due to inter-chain charge hopping. In compounds P−C, P−1F, P−2F, where side-chain mediated crystals are more likely, charge transport takes place either along the chains or is defect assisted.

4

PBTTT: dynamics and macroscopic composition

Though conjugated polymers, such as PBTTT, are routinely used in organic electronics devices [196], their morphologies are still not fully understood. Though these materials are comprised of crystalline, amorphous and other mesophases, only the crystalline part is often considered, when studying transport properties of PBTTT for organic electronics applications [108, 197–200]. A detailed study and analysis are required to understand, control and improve morphologies of polymers in order to achieve better device properties. In the following, I simulate and analyze three morphologies of PBTTT. The simulated data are then combined with a derived analytical model and the solid-state NMR measurements to assess the *macroscopic* composition of the PBTTT-C16 semi-crystalline polymer.

The PBTTT polymer (fig. 4.1) is comprised of a conjugated backbone and linear alkyl side-chains. The backbone contains two thiophene (TH) and a thienothiopehene (TT) units. The C_{16} linear alkyl side-chains are attached to thiophene rings in a regular fashion. Such an attachment [201] allows PBTTT chains to form fully crystalline lamellar structures, in which backbones are forming π-stacks, while side-chains are interdigitated and crystallized in the inter-lamellar space. High PBTTT crystallinity, and good π-stacking in particular, are often linked to high hole mobilities in this polymer and its high performance in organic electronics devices. This also extends to other polymers, as they are observed to perform better upon improved crystallization [167, 202–204].

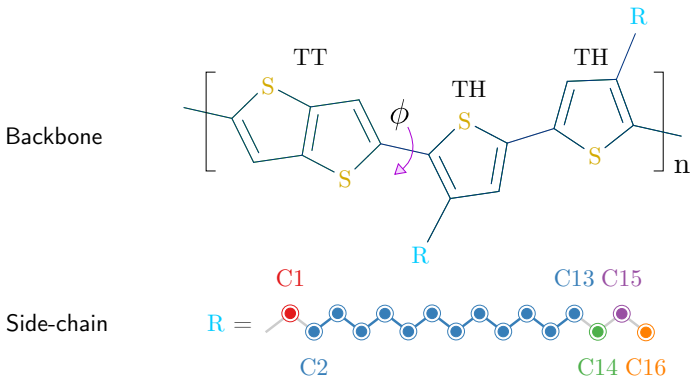

Figure 4.1: Chemical structure of PBTTT-C16 repeat unit, which contains two thiophenes (TH), a thienothiopehene (TT) and two C_{16} linear alkyl side-chains. Angle ϕ is a torsional angle between TT and TH units. Side-chain's color coding is introduced to interpret the experimental data.

4.1 Experimental data

The NMR methods are sensitive to the local environment of molecules and allow to deduce information about structure, dynamics and mesophase composition of soft matter materials. These methods are useful as they provide short range information about the system, in addition to routinely used scattering techniques, such as X-ray and GIWAXS [197–200], which provide long-range ordering data. Also, NMR can give additional information about amorphous regions, which is not available through scattering techniques. Here, I recap the experimental data that were obtained from the solid-state NMR (SS-NMR) measurements of PBTTT-C16 sample, and data from simulated NICS maps, used to interpret the data. Figure 4.2 shows the resulting spectrum for PBTTT side-chains and assignment of peaks to individual atoms in a chain.

4.1.1 Local packing

Because spin-spin couplings are distance dependent [205] (and decay as r^{-3}), they are used to deduce local intermolecular distances in a material. One finds that the d-spacing in the crystalline PBTTT-C16 (shortest distance between two backbones in a π-stack) is 0.352 nm. Combining the NMR data with calculated NICS maps for main chains reveals that the torsion angle ϕ between TT and TH units (see fig. 4.1) is less than $25°$ in a crystal. Also, due to high crystallinity and strong interdigitation of side-chains, the terminal CH_3 groups are in a direct contact with backbones of neighboring stacks. The measured distance between hydrogens of a backbone and terminal CH_3 group is 0.34 nm. This data is useful for verification of force fields used for MD simulations.

4.1.2 Dynamics

Further, NMR deals directly with spin decoupling as a function of time [206, 207]. This allows to probe dynamics of molecular fragments with atomistic resolution. In case of similar environments, the resolution becomes more coarse. Dynamics in NMR is represented by an order parameter, S. It is routinely calculated for C-H bonds [208] as a ratio

$$S = \frac{D^{(e)}}{D^{(i)}}. \tag{4.1}$$

Here, $D^{(e)}$ is the coupling of the bond measured in the NMR experiment and $D^{(i)}$ is the theoretical maximum calculated for an idealized case of static C-H bond [208], in particular $D^{(i)} = 21.0$ kHz. Upon this definition of a dynamic order parameter, one finds that $0 \leq S \leq 1$, where $S = 0$ refers to isotropic rotation (un-restrained bond dynamics), $S = 1$ corresponds to a static bond, while intermediate values correlate with a partial mobility of C-H bonds, modified by the local environment.

In crystalline regions of PBTTT-C16, backbones exhibit highly constrained dynamics with measured $S = 0.9$ for TT and TH units. In side-chains, SS-NMR provides only partially resolved data for atoms C_2–C_{13}, C_{14}, C_{15}, C_{16}, which are 0.71, 0.65, 0.49 and 0.39, respectively.

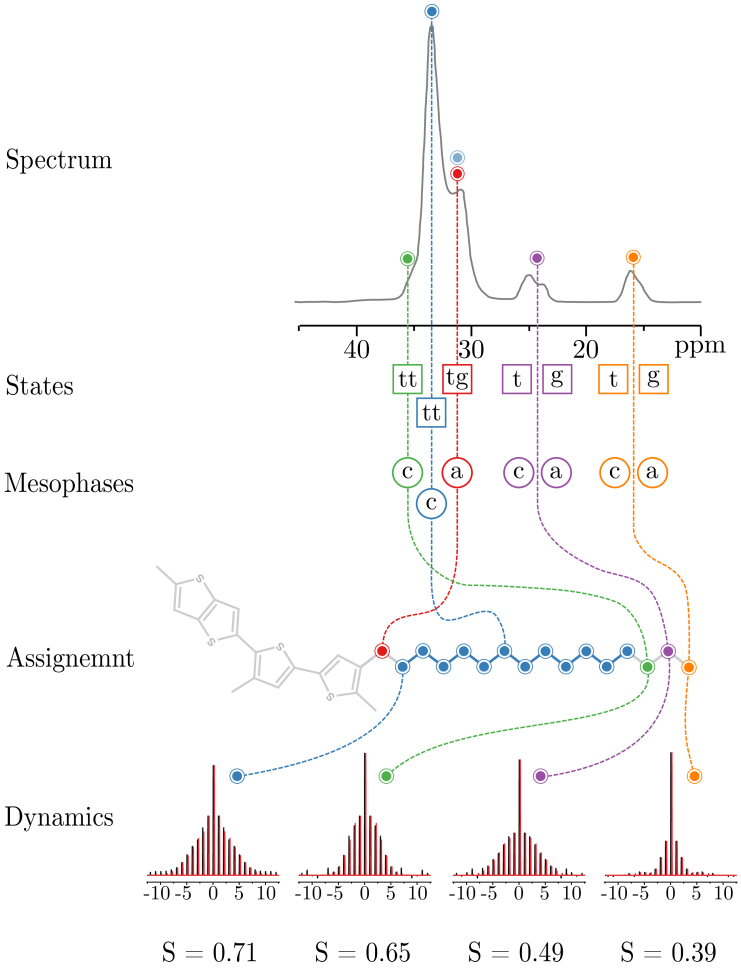

Figure 4.2: Decomposition of the NMR spectrum into trans/gauche conformer contributions, crystalline/amorphous mesophases, assignment to individual atoms in a side-chain and extraction of dynamic order parameters.

Because of morphological constraints and an attachment to the immobile backbones, a large portion of side-chains remains close to static, while the last three carbons at the free end of a side-chain gain more mobility.

In the disordered mesophase, the measurements are less resolved, i.e. less peaks are observed and the signal-to-noise ratio is smaller. The dynamic order parameters for disordered backbones could not be extracted due to insufficient signal intensity. As for the disordered side-chains, order parameters for C_2–C_{13}, C_{15}, C_{16} are 0.34, 0.32 and < 0.4. Such low values signalize a dramatic increase of mobility in amorphous side-chains, as compared to the crystallized ones.

4.1.3 Macroscopic composition

Finally, because various (i.e. ordered and disordered) environments produce signals at different frequencies, one can decompose the NMR spectrum and estimate the ratios of the integrated signal intensities and relate them to macroscopic properties of a material.

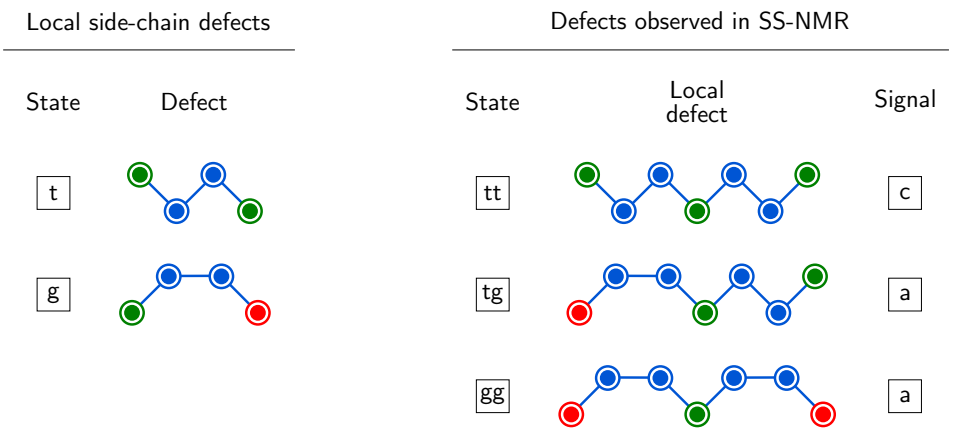

Figure 4.3: Local side-chain conformers (left): Trans (t) and gauche (g); conformers measured in the SS-NMR experiments (right): Doubly-trans (tt), trans-gauche (tg) and doubly-gauche (gg). The (tt) conformer is attributed to ordered side-chains, while the other two are associated with disordered chains in the sample.

In the case of backbones, the change in a signal frequency results from different backbone environments. PBTTT in solution produces signal at 7.1 ppm, while in bulk it generates two signals at 6.9 ppm and 6.1 ppm. The first value is close to the value in a solution and is attributed to disordered backbones. The second, much lower value is generated by ring currents of conjugated fragments [209] and arises from π-stacked morphologies. From the area ratio of these two signals, one can deduce the fraction of chains in a π-stack.

In case of side-chains, the change in spectrum comes from the γ-gauche effect. In it, different frequencies are associated with trans and gauche conformers (see fig. 4.3, left). This allows one to decompose the spectrum and assess conformer concentrations quantitatively [210]. The trans conformers (t) are found in highly crystalline polymer samples, for example PBTTT or P3HT crystallites. The gauche conformers (g) correspond to defects that appear in ideal side-chains. In NMR, these conformers are detected in pairs, in particular from a carbon in the γ-position to a given atom (see fig. 4.3, right). The (tt) conformer is linked to the crystalline side-chains, while (tg) and (gg) conformers represent disordered regions.

For the PBTTT-C16 sample the signal decomposition reveals that 50% of backbones are π-stacked and 50% are disordered. In the side-chains, one finds that 55% of chains are in the crystalline and 45% are in the amorphous state.

Taking into account this correlation between backbone and side-chain values, one concludes that roughly 50% of the material is fully crystalline, and 50% is amorphous. The small discrepancy between the two mesophases can be attributed to a small fraction of the third, intermediate mesophase (possibly an interface between the other two). This result is remarkable on its own, as PBTTT is thought to be a highly crystalline polymer, and its high performance in organic-based devices is often linked to this property.

One should note that the observed spectrum is measured from a single sample. Moreover, side-chain and backbone related signals are obtained independently, i.e. without correlations to each other and to the respective mesophases. In this sense, the decomposition is incomplete.

In the following, MD simulations and a derived model are used to gain more insight into the PBTTT morphology: its local packing, dynamics and macroscopic composition, resolved with respect to individual mesophases.

4.2 Molecular dynamics of PBTTT mesophases

Molecular dynamics simulations are used to simulate atomistic morphologies of PBTTT. In order to run MD simulations of a material, one requires a reliable force field. I adopted the OPLS-based [73] force field of PBTTT-C14, developed earlier [108]. It is re-parameterized from DFT calculations using B3LYP functional and 6-311g(d,p) basis set and reproduces unit cell parameters and the melting temperature of side-chains in the crystalline PBTTT-C14 sample. This force field is extended to PBTTT-C16 and is used in the following MD simulations. Here, C14 and C16 refer to the number of carbon atoms in linear alkyl chains, i.e. fourteen and sixteen carbons per side-chain.

The initial super cell is constructed using an extended PBTTT-C16 force field and available unit cell parameters for the PBTTT-C14 polymer [108]. The super cell is built such that it contains 4 lamellae $\times$ 16 tetramers (64 chains and 512 side-chains in total). It is equilibrated at 300 K in the NPT ensemble (1 atm.) for 1 ns using velocity resclaing thermostat [99], Berendsen barostat [100], 1 ps time step, Ewald summation for electrostatics and 1.2 nm cut-off for van der Waals interactions. Simulations are performed using the GROMACS 4.6.7 simulation package [172, 173]. This setup is used in all following simulations. The equilibrium box values are $a = 2.223$ nm, $b = 0.460$ nm, $c = 1.386$ nm and $\alpha = 129°$, $\beta = 90°$, $\gamma = 90°$. These numbers are close to those of PBTTT-C14 unit cell, apart from longer inter-lamelar distance a, which reflects an elongation of side-chains. The resulting unit cell is shown in (fig. 4.4, a′).

The equilibrated box with crystalline PBTTT-C16 chains is then used to generate the other two morphologies: intermediate and amorphous mesophases. The intermediate mesophase is comprised of crystallized (π-stacked) backbones combined with disordered side-chains. To obtain these two phases, the initial crystalline mesophase is annealed between 300 K and 700 K at the rate 0.25 K/ps in the NPT ensemble for 3.4 ns. Additional steps of constant temperature are added to improve equilibration at auxiliary temperatures (every 50 K). The side-chain melting is observed at 425 ± 25 K, while the backbone packing is destroyed at 575 ± 25 K. The side-chain melting temperature is higher than observed in PBTTT-C14 [108] and can be explained by longer, more restrained chains, which require higher temperatures to alter the packing. The amorphous sample was extracted from 700 K simulation and exposed to an additional equilibration at 2000 K for 2 ns to remove residual anisotropy of chain orientations in the sample. The intermediate mesophase could not be obtained from simulated annealing and was prepared separately using positional restraints of backbone atoms. Inability to extract the intermediate mesophase is due to a direct contact of side-chains with backbones of neighboring lamellae. Because of this, side-chains provide additional stabilization to the π-stack. They also provide additional source of disorder during annealing, which induces backbone melting. After side-chain equilibration restraints are removed, the prepared morphology remains stable.

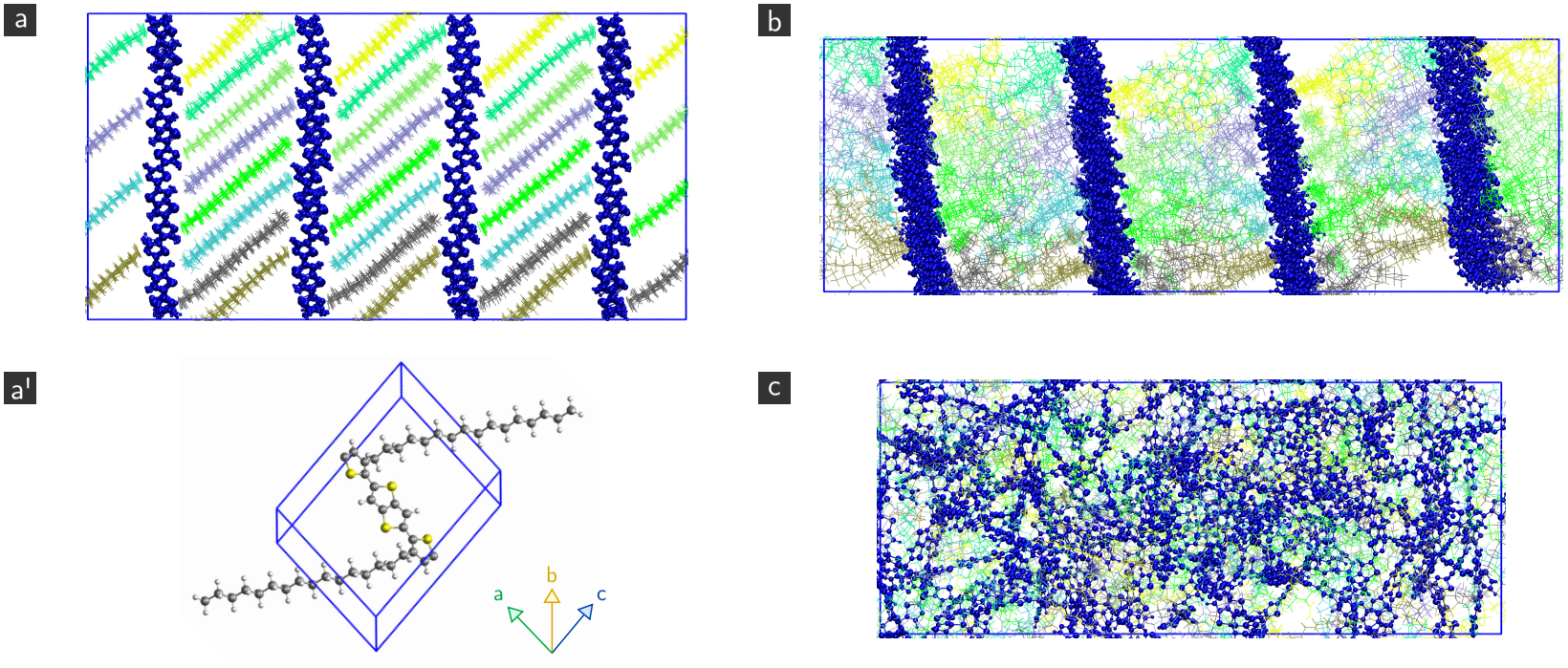

Figure 4.4: Three simulated morphologies of PBTTT: crystalline (a), intermediate (b), amorphous (c). For crystalline PBTTT, a unit cell is shown in (a').

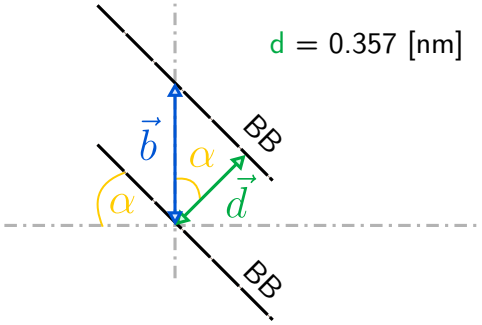

Figure 4.5: Separations in MD simulations and NMR measurements of PBTTT crystals: $\vec{d}$ is the d-spacing vector, $\vec{b}$ is the unit cell vector, and α is an angle between the two vectors. Here, BB stands for backbone.

Resulting three mesophases are quenched to 300 K (1 ns, NPT), simulated for 2 ns in NPT and for 2 ns in NVT ensembles. A production trajectory in the latter run is used for further analysis. Snapshots of all three mesophases are presented in (fig. 4.4, a, b, c). The resulting production trajectories are used to calculate observables of interest. Also, from now on, one will refer to PBTTT-C16 polymer simply as PBTTT. For the sake of completeness, one should mention that more morphologies of PBTTT have been observed, for example π-stacks with partially melted side-chains [108]. In the following, only three mesophases, presented above, will be investigated.

4.3 Local structure of backbones and side-chains

As a first step, one is interested in validity of three simulated morphologies. To do this, one can compare the local packing (i.e. distances and angles between residues) obtained from MD simulations to those recovered from the SS-NMR measurements, as outlined in Section 4.1.1. Two separate data sets are available for backbones and side-chains.

Ordered backbones form π-stacked structures and can be found in crystalline and intermediate mesophases. One can calculate the d-spacing as the smallest distance between two polymer backbones. The visual representation of the d-spacing in given in (fig. 4.5). Its value can be obtained as $d = b\cos(\alpha)$, where b is a length of the unit cell vector along the π-stacking direction and α is the angle between vectors $\vec{d}$ and $\vec{b}$. In simulated crystalline and intermediate mesophases the d-spacings are $d = 0.357$ nm and $d = 0.347$ nm. The two numbers are in excellent agreement with the experimental value of 0.352 nm and suggest a 1:1 ratio between two mesophases, since the measured value is a linear combination of two distances, weighted by the respective mesophase concentrations. However, taking into account small difference between the two simulated values, as well as errors in non-bonded inter-atomic potentials of a force field, any ratio of two mesophases can be realized in the macroscopic sample.

One moves on to torsional angles between PBTTT backbone residues. The simulated mean torsional angles ϕ between TT and TH units of the backbone (see fig. 4.1) have similar values of $12°$ and $11°$ in the crystalline and intermediate mesophases. These angles fall into the angle range of $\phi \leq 25°$ measured in the SS-NMR experiments and reproduce values in

Mesoph.	d-spac. (sim)	d-spac. (exp)	tors. ang. (sim)	tors. ang. (exp)	SC-BB (sim)	SC-BB (exp)	S (sim)	S (exp)
cry.	0.347	0.352	12	≤ 25	0.345	0.34	0.95	0.90
inter.	0.357	0.352	11	≤ 25	-	-	0.90	0.90
amor.	–	> 0.4	–	> 25	-	-	0.83	–

Table 4.1: Local structure within three PBTTT mesophases: Simulated/experimental d-spacing values (d-spac., [nm]), mean torsional angles between TT and TH units of backbones (tors. ang., [°]), distances between side-chain's CH_3 groups and backbone's C-H bonds (SC-BB, [nm]). Additionally, order parameters for C-H bonds of main chains are listed (S, [r.u.]).

earlier simulations of PBTTT crystals [198]. Such broad angle range in the experiment stems from imprecise NICS maps (Nucleus Independent Chemical Shift [209]) that were used to interpret the NMR data. In simulations, angle means are obtained from angle distributions, that are extracted from production trajectories, and fitted with Gaussian functions. A flat angle distribution in the amorphous mesophase reflects the disordered state of backbones.

The last analyzed property is the distance between side-chain's terminal CH_3 groups and backbone's hydrogens of adjacent lamellae. In the crystalline mesophase its value 0.345 nm, which is in a good agreement with the experimental value 0.34 nm. Separations are larger in case of amorphous side-chains (i.e. in intermediate and amorphous mesophases), since introduced defects effectively reduce the side-chain's length in the direction of interest. Exact mean values could not be extracted for the same reason as in the case of amorphous backbones.

The above mentioned simulated distances and angles are summarized in (tab. 4.1) together with the available experimental data. Overall, these calculations prove that the adopted force field is suitable for simulations of three PBTTT mesophases and reproduces the local ordering of chains in them.

4.4 Dynamics of PBTTT

From static properties one continues to studies of PBTTT dynamics in terms of the generalized order parameter (GOP) [145, 211–222]. It can be evaluated from molecular dynamics simulations in a number of ways [223–229] (as outlined in Section 2.3.2). Here, I follow the original definition, outlined by Liapari, Szabo and others [109, 110, 206, 207] and calculate the generalized order parameter directly from the angle auto-correlation function (ACF) as

$$C(\tau) = \langle P_2 \left[\vec{u}(t+\tau)\vec{u}(t)\right]\rangle_{t,e} . \tag{4.2}$$

Here $\langle \dots \rangle_{t,e}$ is a combined time and ensemble average. The ACF is non-negative (i.e. $C(t) \geq 0$) and the order parameter S is calculated as a long-time limit

$$S = \left[\, C(\infty) \,\right]^{1/2} \tag{4.3}$$

In practice, an ACF converges at a finite time τ_c, and one can calculate S as an average over its plateau region

$$S = [\ \langle C(\tau > \tau_c)\rangle_\tau\ ]^{1/2}\,. \tag{4.4}$$

In dense polymer systems, such as PBTTT morphologies, after ensemble, time and plateau averages, the relative errors of calculated order parameters are drastically reduced. In case of PBTTT simulations, the largest relative GOP error is less than 10^{-3}.

Following this protocol, parameters S are calculated for conjugated C-H bonds in backbones and C-H bonds in alkyl chains. These values are then compared to NMR observables, presented in Section 4.1.2. Both simulated and experimental data are summarized in tables (tab. 4.1, backbones) and (tab. 4.2, side-chains). In alkyl chains, parameters S are averaged over atoms $C_2{-}C_{13}$ in order to match the resolution of NMR data. Examples of auto-correlations functions, calculated for side-chains in three mesophases at normal conditions, are shown in (fig. 4.7). For PBTTT $t_c = 1.5$ ns, i.e. last 500 ps of the auto-correlation functions are used to calculated the order parameters. In case of not converged autocorrelation functions, the resulting order parameter is an upper limit of its true value.

For backbones, simulated order parameters are in a good agreements with available NMR data ($S \approx 0.9$). In side-chains, all simulated order parameters are systematically higher than those recovered from NMR measurements in all three mesophases. Still, the data are in good qualitative agreement with experiment and reproduce the observed trend of gaining mobility while approaching the free end of a side-chain.

Yet, simulated dynamics is much slower and more restrained, as compared to the experiment. This discrepancy is explained by short simulation times and, hence, insufficient sampling [230]. This was observed in simulations of proteins, where the generalized order parameter S is linked to the configurational entropy of side-chains E via an empirical expression $E = a + b \cdot S^2$ (where $a, b > 0$), i.e. side-chains with lower S have lower entropy and vice versa [227, 231–233]. Extending this concept further, at short measurement times (be it in experiment or in simulation) side-chains explore only a small portion of available configuration space, resulting in lower entropy and higher order parameter numbers. This is the case, as the simulation times (1 ns) are much shorter than the averaging times (130 μs) of the NMR experiments.

Another hint is gained from the exponential time-series of the ACF. Typically, one considers only one or two terms of the expansion [109, 110], but in general an arbitrary number of exponents can be used

$$C(t) = \sum_{i=0}^{N} a_i e^{-t/\tau_i}, \tag{4.5}$$

where τ_i are the characteristic transition times of processes in the system, and in particular a_0 is the generalized order parameter, $a_0 = S^2$ for $\tau_0 = \infty$. One can link longer transition times τ_i to higher energy barriers that need to be crossed. Therefore, during short simulation

Mesoph.	C_1 (sim)	(exp)	C_2–C_{13} (sim)	(exp)	C_{14} (sim)	(exp)	C_{15} (sim)	(exp)	C_{16} (sim)	(exp)
cryst.	0.96	–	0.91	0.71	0.80	0.65	0.80	0.49	0.25	0.39
int./am.	0.77	–	0.53	0.34	0.34	–	0.34	0.32	0.12	<0.40

Table 4.2: Partially resolved values of generalized order parameters S for side-chains extracted from MD simulations and SS-NMR experiments in three mesophases.

times, the system remains confined to a small region of a configuration space, thus effectively truncating the series and yielding higher values of S. This suggests that in our case one needs more than five orders of magnitude longer simulations in order to observe such low order parameters as in experiment, which is not feasible.

Interestingly, S values for the disordered side-chains in the intermediate and amorphous mesophases have similar values. This shows that side-chain's dynamic properties have small dependence on the state of the attached backbones (rigid π-stacks or mobile disordered chains). For this reason, these data are listed as a single entry in (tab. 4.2).

4.5 Dynamics extrapolation

It was shown that the reason for a mismatch between measured and simulated GOP values (the S parameter) comes from different times, at which side-chain dynamics is observed. To reproduce experimental values, one has a number of possibilities. The brute force approach to run long simulations (even for a small system) is not feasible as one needs to increase the simulation time by at least five orders of magnitude (from 1 ns to 130 μs). Alternatively one can tune the Hamiltonian such that it reproduces the desired values of GOP [234], which is tedious to implement.

Here, one follows an ad-hoc approach, often used for simulations of polymer melts. It is motivated by a property of polymer melts: the dynamics of chains at higher temperatures can be rescaled to dynamics at normal conditions at a larger time. It is known as time-temperature superposition principle. For example, from MD simulations of polyethylene [235, 236] it was shown that Vogel–Fulcher equation holds

$$-\ln \tau = A - \frac{B}{T - T_0}, \tag{4.6}$$

that is one can build a smooth map between a given relaxation time τ in a system and a temperature T. Here, T_0 is reference temperature, A, B are the fitting parameters.

Because disordered side-chains exhibit the largest mismatch compared to experimental data and because their dynamics is weakly coupled to the backbone state, one can try to use high temperature MD runs to extrapolate the dynamics of PBTTT side-chains [237].

To do this, three equilibrated mesophases are simulated in the NVT ensemble at various temperatures (between 300 K and 500 K, step 50 K). The constant volume simulations ensure that the available configuration space of side-chains is not changed and extra temperature

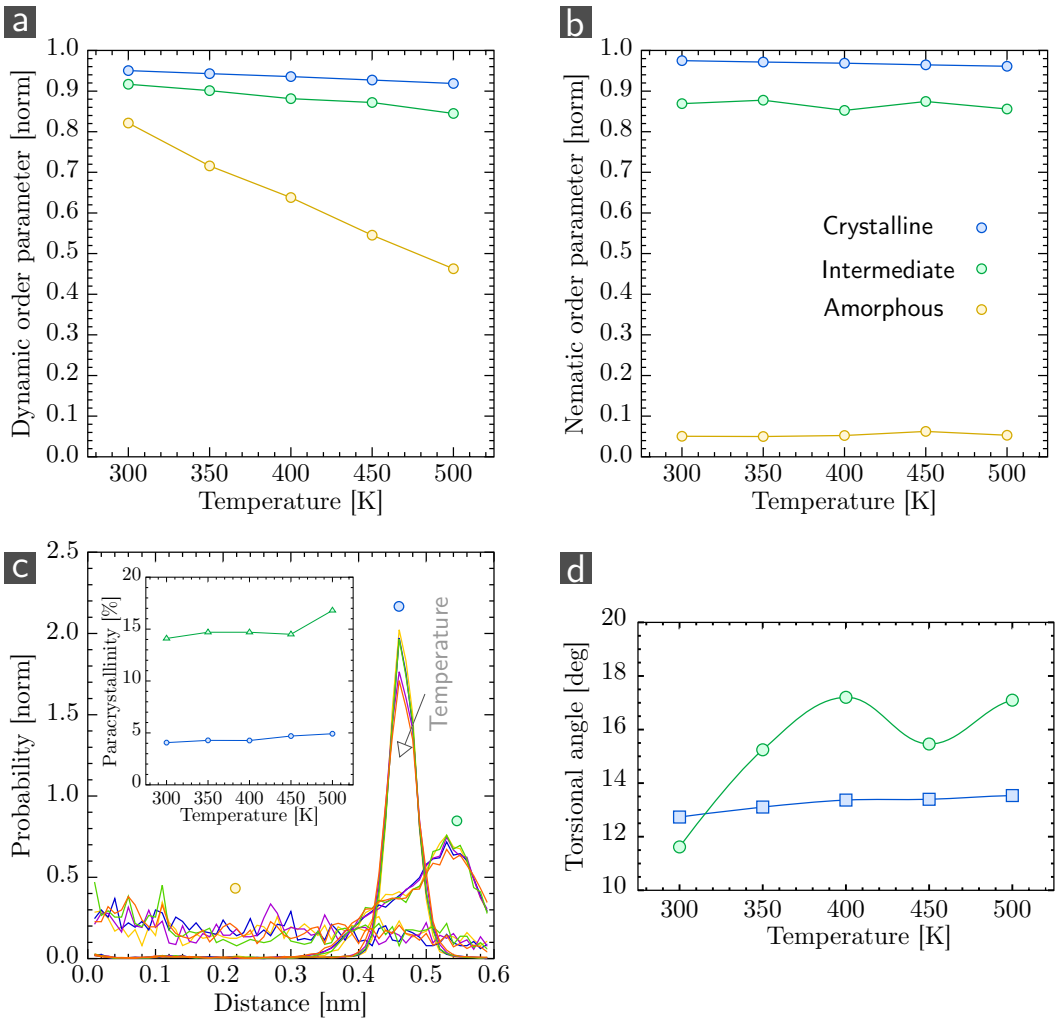

Figure 4.6: Dynamic order parameter (a), nematic order parameter (b), paracrystallinity (c) and backbone's torsional angles (d) calculated in three mesophases in the temperature range 300 K to 500 K.

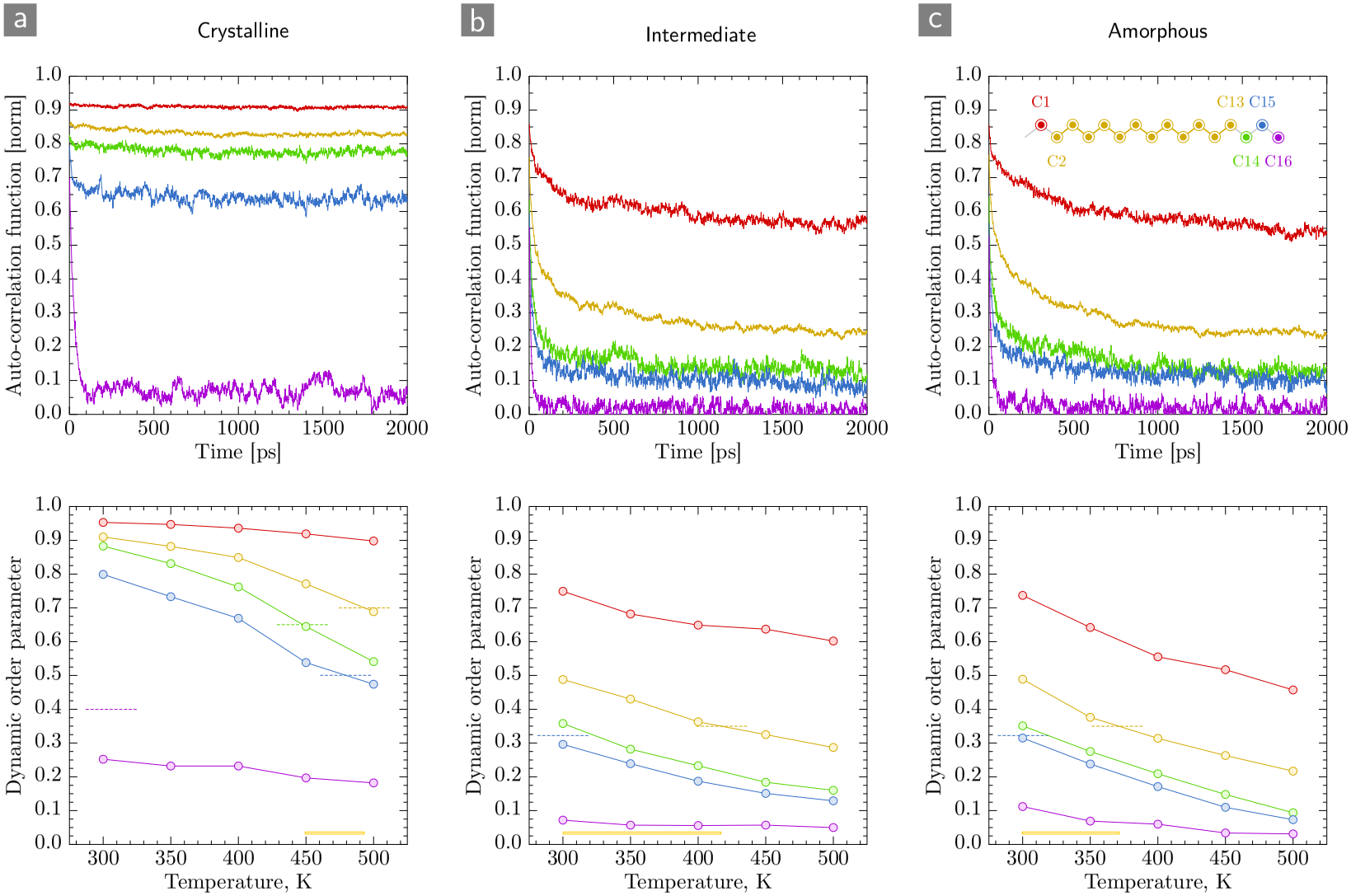

Figure 4.7: Auto correlation functions at 300 K (top) and GOP values for all temperatures (bottom) in crystalline (a), intermediate (b) and amorphous (c) mesophases. GOP values are extracted from corresponding ACFs. Color coding is explained in the inset. Horizontal intersections correspond to experimental data and mark temperatures, at which the simulated dynamics is matched in the experiment.

only affects the transitions between the barriers and accelerates the side-chain diffusion. Because one aims at the slowest processes, bond-angle vibrations and other fast degrees of freedom are of small concern. To check that the backbone structure is not changed during the run (i.e. phase transitions did not take place), the dynamic, nematic and paracrystalline order parameters are calculated in three mesophases.

Order parameters are calculated as presented in Section 2.3. Dynamic order parameter reflects on orientation of molecules in a system through time. It takes values between 0 and 1, where lower values correspond to a frozen morphology and higher values are obtained for freely rotating molecules. Nematic order parameter characterizes spatial order in the system. If it takes values close to zero, the morphology is disordered in each moment of time, while values close to one reflect high degree of backbone alignment in a simulation box. Also, the paracrystallinity parameter is used to assess the ideality of a crystal in a given direction: The lower the value, the more disorder is present in the sample. These three order parameters as well as torsional angles between TT and TH units are shown in (fig. 4.6).

The dynamic and nematic order parameters of backbone's C-H bonds in the crystalline and intermediate mesophases remain constant at all temperatures (see fig. 4.6, a, b). This shows that in two mesophases beckbones are well aligned in the simulation box and maintain this orientation through time. This is additionally supported by the angle distributions of the TT-TH dihedrals (fig. 4.6, d) and paracrystallinity values (fig. 4.6, c), calculated along the z-axis (i.e. the unit cell's vector b). An introduced side-chain disorder in the intermediate mesophase results in a systematic lowering of the dynamic and nematic order parameters, while paracrystallinity and mean torsion angle values are increased.

One should note, that a factor of three increase of the paracrystaline parameter in the intermediate mesophase is an artifact, as it is based on a distance distributions with multiple peaks, which effectively have larger width, hence, larger paracrystalinity values. In fact, paracrystallinity is only meaningful within one crystalline mesophase and is not suitable for a cross-comparison of periodic structures.

As opposed to partially ordered mesophases, the amorphous system is characterized by a decreased dynamic order parameter. This is a direct consequence of a larger volume of the simulation box. The nematic order parameter is close to zero, reflecting a homogeneous distribution of backbone orientations. As a result of homogeneity, parameters, such as paracrystallinity and backbone torsional angles, cannot be evaluated for the amorphous mesophase.

Upon confirming that backbone structure is not changed in the course of high temperature simulations, one looks into the side-chain dynamics. At elevated temperatures, side-chains diffuse more efficiently. They explore larger regions of an available configuration space and show lower GOP values. To estimate the temperature, at which simulated dynamics of disordered side-chains corresponds to the observed dynamics with $t = 130$ μs, one can match the corresponding generalized order parameters. One calculates GOP values in three systems as a function of temperature and compares them to the experimental values. The result is shown in (fig. 4.7). Once again, the dynamics of disordered side-chains in intermediate and amorphous mesophases is very similar and does not depend on a state of the backbones. In the crystalline mesophase, the experimental GOP values are well clustered

Mesoph.	cry.	int.	amo.
T [K]	475 ± 25	425 ± 25	375 ± 25

Table 4.3: Rescaling temperatures, which re-map ns, high temperature dynamics to μs dynamics at 300 K. These temperatures are obtained from matching S parameters in simulations and NMR experiments.

around $T = 425 \pm 25$ K. In the other two mesophases containing disordered side-chains, the GOP values are more scattered. The reason for this is a uniform energy distribution along side-chain moieties due to high temperature dynamics. The temperatures are chosen by matching the GOP of in-bulk C_2-C_{13} atoms. They are $T = 475 \pm 25$ K and $T = 375 \pm 25$ K, respectively, and are summarized in (tab. 4.3).

To summarize, high temperature MD runs allow to assess the side-chain dynamics of three PBTTT mesophases. Simulated order parameters are compared to the SS-NMR values in order to estimate the temperature at which side-chain's diffusion is equivalent to the one in experiment. As a result, simulated ns dynamics can be effectively treated as the one at μs timescale. Though high temperature runs and characteristic temperatures could not be directly compared to the experiment, they will play an important role when assessing the macroscopic composition of the PBTTT sample.

4.6 Macroscopic composition

The third set of observables, obtained from the SS-NMR experiments is of the most interest and addresses the macroscopic composition of PBTTT (see Section 4.1.3). From the ratio of NMR integral signals produced by backbones, one can deduce the fraction of disordered chains in the sample, which is 50%. The γ-gauche effect provides an estimate the concentration of side-chains in a crystalline state: It is 55% for PBTTT. Combining the two data sets, one concludes that 50% of the PBTTT sample is crystalline and 50% is amorphous. In the following, I will link MD simulations of three PBTTT mesophases to their macroscopic concentrations in a sample via a derived model and verify the proposed material composition.

4.6.1 Balance equations for side-chain conformers

Similarly to the NMR decomposition, one can link side-chain defects to the macroscopic composition of a sample by means of an analytical model. Let one assume a macroscopic sample that is comprised of N identical polymer chains, grafted with alkyl side-chains. The total number of states, in which the side-chains can be found, is s. In this case it is sufficient to use the coarse-grained representations, i.e. follow the local minima in the free energy curve. Those minima correspond to local trans/gauche conformers. Because polymer chains are identical, the number of conformers per molecule is the same and is equal to S. Then, the total number of conformers in the system is proportional to the number of molecules, i.e. $s = NS$.

One of possible ways to track conformers is via dihedral minima of side-chains. An example of dihedral distribution $H(\phi)$ is shown in (fig. 4.8), which is calculated for a short alkyl chain (7 repeat units) in vacuum using Langevin thermostat at T = 300 K for 100 ns. From it, one can see three conformers that a dihedral can visit. Additionally, a potential energy curve is calculated from this distribution via the Boltzmann inversion as

$$U(\phi) - U(180) = -k_B T \cdot \log\left[H(\phi)\right], \tag{4.7}$$

and is shown in (fig. 4.8), where k_B is the Boltzmann constant and $U(180)$ is an energy offset. The global minimum of the potential (t) corresponds to trans conformer of a dihedral, while two (g) minima correspond to gauche conformers.

Alternatively, these conformers can be represented through unique minima pairs: Doubly-trans (dd), trans-gauche (tg) and doubly-gauche (gg). The total numbers of conformers within a molecule are T, G and D. This representation matches the signal interpretation in the NMR experiment. And so, one can write a microscopic *balance* equation

$$T + G + D = S \tag{4.8}$$

From the macroscopic perspective, out of the total N molecules in the sample, N_c are found in the crystalline regions, N_i in the intermediate, and N_a in the amorphous. Naturally, the total number of molecules in the system is conserved

$$N_a + N_i + N_c = N. \tag{4.9}$$

In each of these regions, the number of conformers T, G and D in the side-chains is different due to local environment within each mesophase. Consequently, one can introduce mesophase-specific parameters T_α, G_α and D_α, where index α can take values c, i and a (referring to the *crystalline*, *intermediate* and *amorphous* mesophases). The equation for all available conformers (eq. 4.8) can then be re-written as

$$SN = S\sum_{\alpha}^{c,i,a} N_\alpha = \sum_{\alpha} \left(T_\alpha + G_\alpha + D_\alpha\right) N_\alpha. \tag{4.10}$$

Summation over three mesophases $\alpha = c, i, a$ is assumed from now on. Next, one introduces the relative fractions, such as a fraction of molecules within the α-th mesophase (i.e. $n_\alpha = N_\alpha/N$) and relative conformer fractions in this mesophase (i.e. $t_\alpha = T_\alpha/S$, other fractions are introduced in a similar fashion).

As a result, equations (4.8, 4.9, 4.10) become a set of normalization conditions

$$t + g + d = 1, \tag{4.11}$$

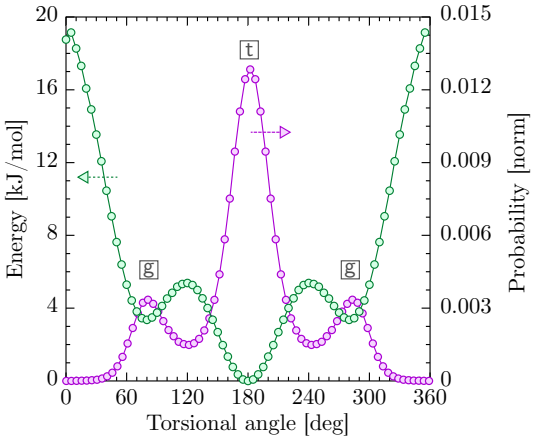

Figure 4.8: The distribution of dihedral in a isolated chain (purple) and the corresponding Boltzmann-inverted potential. Letters (t) and (g) mark trans and gauche local conformers in a side-chain.

$$t_\alpha + g_\alpha + d_\alpha = 1, \tag{4.12}$$

$$n_c + n_i + n_a = 1, \tag{4.13}$$

where t, g and d are sample-averaged conformer fractions, defined as

$$\sum_\alpha n_\alpha t_\alpha = t, \tag{4.14}$$

$$\sum_\alpha n_\alpha g_\alpha = g, \tag{4.15}$$

$$\sum_\alpha n_\alpha d_\alpha = d. \tag{4.16}$$

These variables, as fractions, are naturally non-negative and restrained

$$0 \leq n_\alpha \leq 1,\ 0 \leq t_\alpha \leq 1,\ 0 \leq g_\alpha \leq 1,\ 0 \leq d_\alpha \leq 1. \tag{4.17}$$

At this point, one has a set of fifteen unknown parameters (local concentrations of side-chain conformers t_α, g_α, d_α, their averages t, g, d, and global mesophase concentrations n_α). Only six variables are independent, while the remaining nine *parameters* have to be provided. In the following sections, *macroscopic* parameters t, g, d will be taken from the SS-NMR measurements and *microscopic* parameters t_α, g_α, d_α will be extracted from MD simulations of three PBTTT mesophases, which were conducted previously. This is sufficient to decouple equations and solve them with respect to variables n_α, i.e. obtain the macroscopic composition of the PBTTT sample.

4.6.2 Introducing the NMR data

A number of simplification can be made, when NMR data are incorporated. First, the ratio of NMR signals can be used. In terms of the above equations, these fractions are exactly the introduced parameters t, g and d. One can use sample-averaged data derived from the experiment to decouple equations and solve them independently.

Second, in the SS-NMR spectra, doubly-gauche conformers are not observed in the PBTTT sample. This is taken into account by setting the sample-averaged parameter d to zero. As a result, parameters $d_\alpha = 0$ and equations (4.11 − 4.17) simplify to

$$\sum_\alpha n_\alpha t_\alpha = t, \tag{4.18}$$

$$\sum_\alpha n_\alpha g_\alpha = g, \tag{4.19}$$

$$t_\alpha + g_\alpha = 1, \tag{4.20}$$

$$n_c + n_i + n_a = 1, \tag{4.21}$$

$$0 \leq n_\alpha \leq 1,\ 0 \leq t_\alpha \leq 1,\ 0 \leq g_\alpha \leq 1, \tag{4.22}$$

Here, t, g are now parameters, given by the experiment. Because parameters t_α and g_α are linked by the normalization (eq. 4.20), only two equations need to be solved. They are

$$t_c n_c + t_i n_i + t_a n_a = t, \tag{4.23}$$

$$n_c + n_i + n_a = 1, \tag{4.24}$$

$$0 \leq n_\alpha \leq 1,\ 0 \leq t_\alpha \leq 1, \tag{4.25}$$

Such decoupling reduces the number of independent parameters to four (i.e. six unknowns t_α, n_α with two equations, t is an empirical parameter). Further, parameters t_α are microscopic and can be extracted from MD simulations, so there is only one independent variable.

The last simplification relies on observations concerning disordered side-chains. It was shown that in simulations side-chains' structure and dynamics have similar properties. Hence, it is useful to introduce an averaged *disordered* conformer density $\tau = (t_a + t_c)/2$. Upon such definition the two concentrations become $t_a = \tau + \Delta t$ and $t_i = \tau - \Delta t$, where $\Delta t = (t_i - t_a)/2$ is the difference between two concentrations. For any PBTTT sample, this difference is no

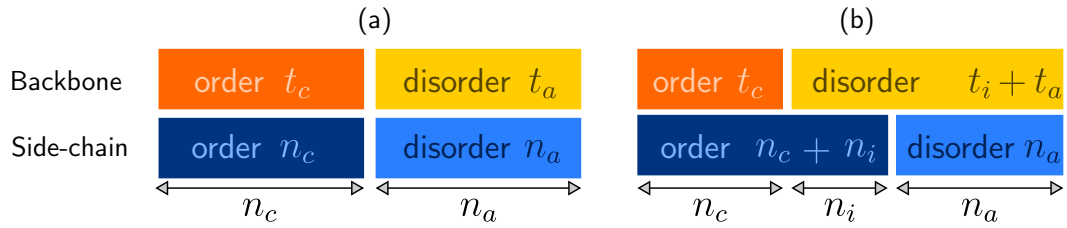

Figure 4.9: Two possible cases of PBTTT composition: (a) two-mesophase composition, suggested in NMR, (b) a proposed three-mesophase composition. Parameters t_α are fractions of side-chains in "trans" conformation, n_α are concentrations of mesophases, indeces c, a, i represent three mesophases.

more than 0.02 and is much smaller than any of three concentrations or differences between them

$$\Delta t \ll t_c - t_a,\ t_c,\ t_a \tag{4.26}$$

This small parameter will allow further simplifications of equations.

Two cases of composition

Because the generic equations are under-defined and contain free parameters, one needs to introduce more information to solve them. In the following, two cases of morphology composition will be considered.

From the experiment, it is suggested that the PBTTT sample is half crystalline and half amorphous. This is observed for both backbones and side-chains. Possibly, the third mesophase is present in small quantities. This suggests that $n_c \approx n_a \approx 0.5$ and $n_i \approx 0$, as well as $t_c \approx 1$ and $t_i \approx t_i \approx 0$. This composition is schematically shown in (fig. 4.9, a). However, it will be shown that the assessment of parameters t_α in NMR is incorrect. To demonstrate this, one can write a more general model that includes this result. For example, $n_c = 0.5 - x$, $n_a = 0.5 - x$ and $n_i = 2x$, where x should be small. Here, the normalization for n_α is satisfied by construction and the original assumption is recovered for $x = 0$. Then the fraction of the intermediate mesophase is

$$n_i = 2x = \frac{t_c + t_a - 2t}{t_c + t_a - 2t_i}. \tag{4.27}$$

After employing the similarity between side-chains in the intermediate and amorphous mesophases, i.e. introducing the averaged quantity τ, one can rewrite this expression as

$$n_i = \frac{t_c + \tau - 2t}{t_c - \tau}. \tag{4.28}$$

It will be shown that this mesophase composition cannot be realized since parameters t_α are, in fact, far from NMR estimates. In the model, the case $n_i = 0$ can never be achieved within the range of possible values for t_α.

A more generic model is required, which includes all three mesophases and allows their arbitrary concentrations. In particular, the third, intermediate mesophase contributes to the conformer fractions of ordered backbones and disordered side-chains (see fig. 4.9, b). To begin with, the generic expression (eq. 4.23) for convenience can be transformed to

$$n_c = \frac{t - t_i}{t_c - t_i} + n_a \frac{t_i - t_a}{t_c - t_i} \tag{4.29}$$

It was mentioned that the equation is under-defined and n_c explicitly depends on the other macroscopic variable n_a. If the small parameter Δt is introduced

$$n_c = \frac{t - \tau}{t_c - \tau} + \frac{1}{2}\frac{\Delta t}{t_c - \tau}(2n_a - 1) + \frac{1}{2}\frac{\Delta t}{t_c - \tau} n_c. \tag{4.30}$$

The main contribution comes from the first term, while the last two are proportional to Δt and can be neglected. Hence, with good accuracy

$$n_c = \frac{t - \tau}{t_c - \tau}. \tag{4.31}$$

This is a remarkable result: The fraction of the crystalline mesophase in the sample can be determined from the ratio of two integral NMR peaks t and the simulated local side-chain configuration densities t_α.

Though the small parameter Δt allows to decouple macroscopic variables n_c from the other two, it prevents such decoupling for variables n_i and n_a. Hence, additional information needs to be provided to obtain the two concentrations. One can use the available SS-NMR data for backbone concentrations (i.e. $n_c + n_i \approx n_a \approx 0.5$) and obtain the intermediate mesophase concentration n_i from the normalization condition

$$n_i = 1 - n_c - n_a = 0.5 - n_c. \tag{4.32}$$

The error that was introduced in (eq. 4.30) by neglecting the two terms is small. The middle term is exactly zero for the PBTTT sample as $n_a = 0.5$ (though it remains small for the cases $n_a \neq 0$ as well). The largest error last term can produce does not exceed 2.5%. For the mesophase concentrations of PBTTT that will be obtained later, this error is 0.3%.

To summarize, concentration n_c of the crystalline mesophase can be obtained from the model. Parameters of the model are derived from microscopic MD simulations and taken from NMR measurements of side-chains. The NMR data for backbones provide a value of the amorphous mesophase concentration n_a. As a result, concentration n_i can be assessed.

The proposed model resolves a composition of a three-mesophase mixture. To extend the model and include more mesophases, one needs to introduce additional equations and

parameters. Consequently, more experimental data as well as morphology simulations are required.

4.6.3 Analysis of the model

Before I estimate any numbers from MD simulations, it is useful to analyze the derived expressions. The two composition cases behave similarly, hence only the second case (eq. 4.30) is analyzed. The crystalline fraction is completely defined through microscopic variables as

$$n_c = \frac{t - \tau}{t_c - \tau} \tag{4.33}$$

Here, one recovers an intuitive result: Concentration of the crystalline mesophase is proportional to the total trans-trans signal t generated by the sample. Also, this equation shows limits, in which the total signal t can be varied in this model, that is $\tau \leq t \leq t_c$. Otherwise the molecule's concentration becomes unphysical. Note that without knowing the microscopic parameters t_α, one can have any concentration n_c between 0 and 1. Next, one uses the validity ranges for n_c, t_c and τ. They are

$$0 \leq n_\alpha \leq 1,\ 0 \leq t_\alpha \leq 1,\ 0 \leq \tau \leq 1. \tag{4.34}$$

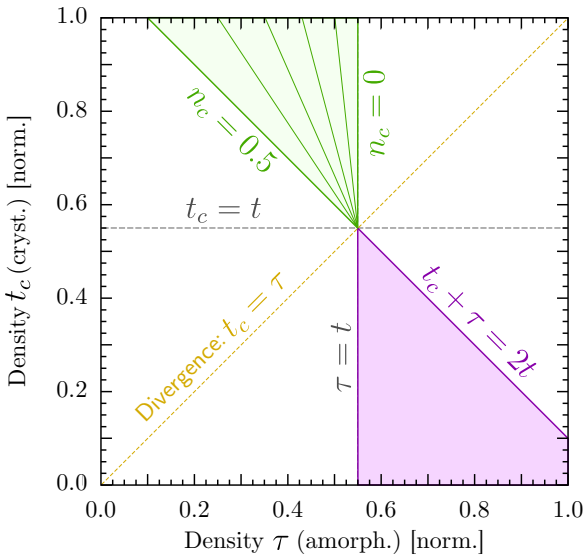

Figure 4.10: A 2D map of possible n_c concentrations in the semi-crystalline PBTTT sample as a function of (tt) conformer concentrations in amorphous / intermediate mesophases (τ) and crystalline mesophase (t_c). The colored areas are a graphical representation of the derived restraints on n_c: True values of n_c are shown in green and range between 0 and 0.5; physically impossible areas are shown in purple and white. The two areas are separated by a line $t_c = \tau$. Empirical parameter t is set to its experimental value 0.55.

In particular, $0 \leq n_c \leq 0.5$, since $n_a \approx 0.5$ and is known. These are combined with a constraint

$$\tau \leq t_c \ . \tag{4.35}$$

The last inequality reflects a physical fact that side-chains in the crystalline mesophase are more ordered than in the amorphous ones, hence should contain more (tt) conformers. Applying these limits to the parametric solution (eq. 4.33), one obtains

$$\tau \leq t \leq t_c, \tag{4.36}$$

$$2t \leq t_c + \tau \tag{4.37}$$

where the two inequalities should be fulfilled simultaneously to ensure meaningful conformer fractions. Without physically intuitive limitation $\tau \leq t_c$, one arrives at the second option for parameter ranges

$$\tau \geq t \geq t_c, \tag{4.38}$$

$$2t \geq t_c + \tau, \tag{4.39}$$

which is separated from a physical region by a line $t_c = \tau$, on which the concentration of the crystalline mesophase n_c is infinite. The two regions, defined by the inequalities, are shown in (fig. 4.10). In it, simulated parameters t_α and resulting n_c values should fall within the green area.

4.6.4 Trans-gauche effects in MD simulations

After the model analysis, one returns to the molecular dynamics simulations, in order to assess the missing parameters t_α. Following the NMR definition, one requires cross-correlation plots of $P(\phi_i, \phi_{i+3})$ dihedral angles (as defined in fig. 4.12, e), to assess conformer fractions directly. Here, i is the bond index. The corresponding distribution are shown in (fig. 4.12, a-d) for ordered and disordered side-chains at 300 K and 500 K. Data in the amorphous and intermediate mesophases are similar, hence the latter is not shown.

The global minimum in the potential energy surface of the C-C-C-C dihedral is the trans conformer, and is found at $180°$ in the OPLS force field (fig. 4.12), while the remaining local minima correspond to less favorable gauche conformers of the chains and are found on a grid at $180 \pm 70°$. Apart from the expected thermal broadening, one can clearly see that the dominant side-chain conformer state is “trans”, even in the melted side-chains at 500 K. This means that a significant portion of the “ordered” NMR signal comes from disordered side-chains, and not only from the crystalline part.

The 2D dihedral angle maps are then used to calculate (tt), (tg) and (gg) conformer fractions in related samples. Numerical values of these fraction are shown in (fig. 4.13) as a function of temperature. As expected, the highest fraction of (tt) conformers is observed in the crystalline mesophase at all temperatures. It is followed by the intermediate and amorphous samples, which have almost identical trends. The opposite picture is seen for (tg) and (gg) conformers, as they represent defects. The (gg) fraction is the smallest in all three samples and is close to zero in the crystalline mesophase. One should note that, though small, the contribution of (gg) conformers is notable in a total statistics.

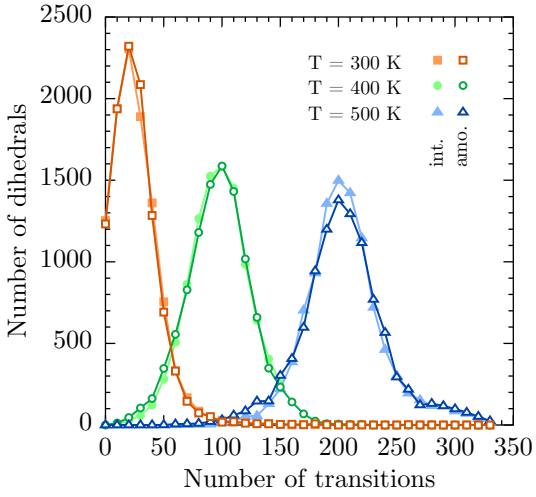

Figure 4.11: Distributions of transitions in alkyl side-chains at $T = 300$ K, $T = 400$ K, $T = 500$ K in intermediate (full symbols) and amorphous (empty symbols) mesophases.

Additionally, statistics is calculated for a short alkyl chain in vacuum, simulated in SD at 300 K for 1 μs. The corresponding cross-correlation plot is shown in (fig. 4.12, f). The analysis of its trajectory gives the distribution of (tt), (tg) and (gg) conformers as 0.45, 0.45, 0.1. This parameter set is very close to values obtained for melted side-chains at 500 K. One may suggest that at this temperature, the resulting numbers represent a fully equilibrated system, i.e. $t = \infty$. Another times scale is defined by the side-chain diffusion, which obtained from matching the order parameter in simulations and an experiment. In this way one defines three simulation times: 1 ns, 130 μs and infinitely long runs. The last two times are extrapolated from high temperature simulations. The respective values of local side-chain conformer concentrations are extracted for these times are presented in (tab. 4.4).

From the analysis of MD simulation of PBTTT mesophases, one observes that correlated dihedral angle distributions $P(\phi_i, \phi_{i+3})$ can be factorized, with good accuracy, into a product of two individual dihedral angle distributions $p(\phi)$, i.e. $P(\phi_i, \phi_{i+3}) \approx p(\phi_i)p(\phi_{i+3}) = p(\phi)^2$, where ϕ is the dihedral angle. One consequence of such factorization is that one can estimate the number of (tt) conformers as $x_{tt} = x_t^2$. Here, x_{tt} is the fraction of doubly-trans conformers and x_t is the fraction of individual trans conformers in disordered side-chains. In current notation $t_c = x_{tt}$. This result was observed in earlier simulations of bulk polyethylene (PE) melt [235, 236], in which conformer transitions $(i, i \pm 3)$ are almost independent of each other, since the corresponding conditional probability $P(i \pm j | j = i + 3) \leq 0.05$ at $T = 300$ K and decreases further at higher temperatures, where i, j are relative positions of dihedrals along an alkyl chain.

This simplification allows to estimate (tt) conformer fractions from other simulations of PE melts, in which trans/gauche conformer population was calculated. In MD simulations of bulk PE at $T = 413$ K (above the melting point) [238], the observed concentration of trans conformers is $x_t = 0.6$, hence, $x_{tt} = 0.36$. Same result is obtained from MD simulations of united atom PE in bulk [239]: $x_t = 0.6$ ($x_{tt} = 0.36$) at $T = 450$ K, and from MD/Monte Carlo simulations of PE at $T = 450$ K on a graphene substrate [240], where $x_t = 0.63$ ($x_{tt} = 0.37$). Also, almost no pressure dependence was observed. Finally, a direct evaluation of trans/gauche conformers was done with the solid-state NMR measurements [241] in

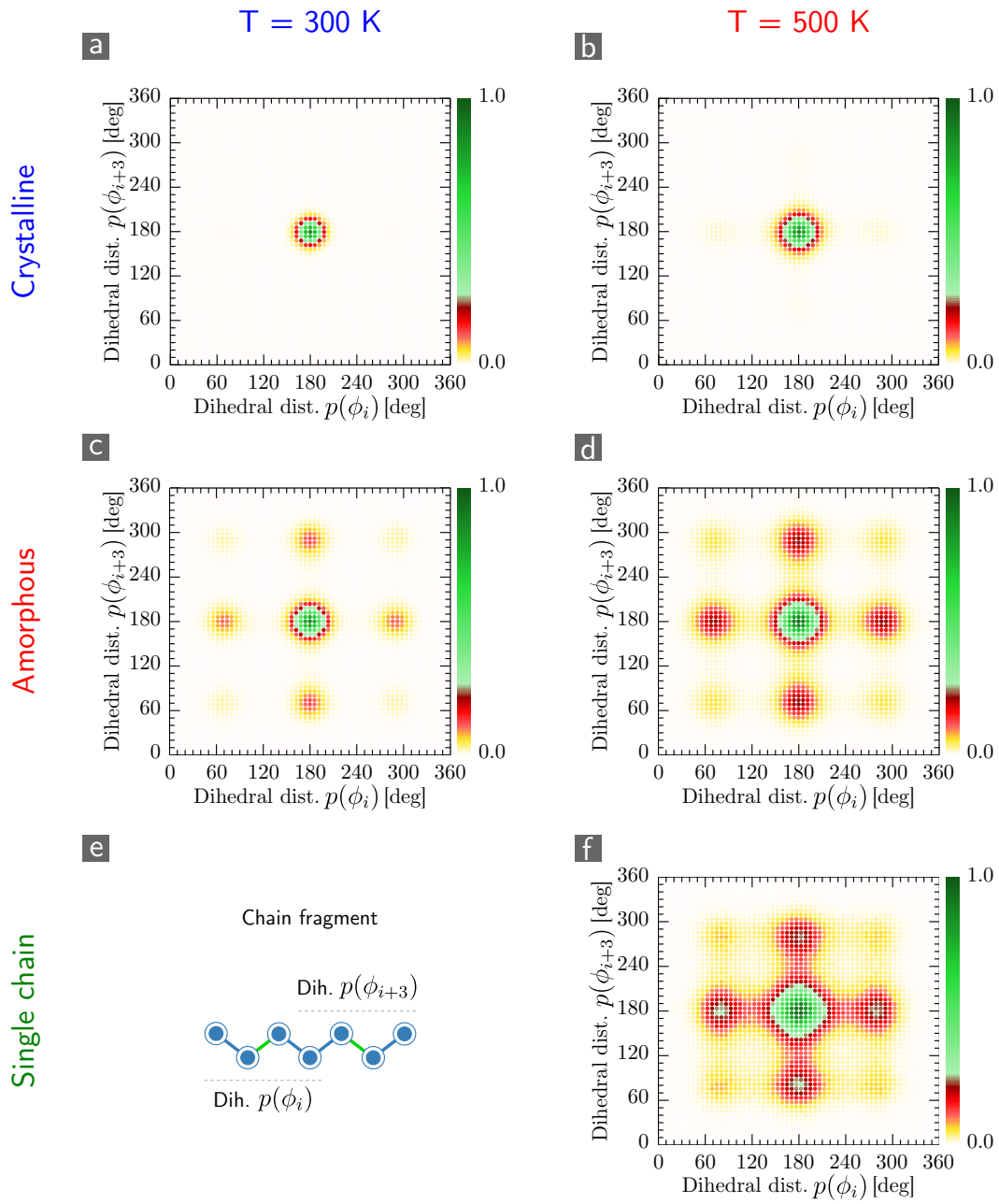

Figure 4.12: Angle distributions of dihedrals in γ-positions in ordered (a,b) and disordered (c,d) side-chains at 300 K (a,c) and 500 K (b,d). The same plot for a single chain in vacuum at 300 K is shown in figure (f), while chain fragment used for the calculation is shown in figure (e).

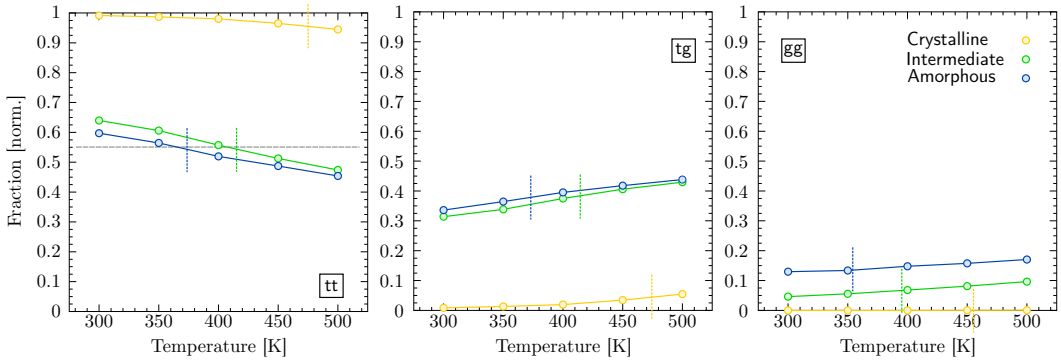

Figure 4.13: Concentrations of (tt), (tg) and (gg) side-chain conformers in three PBTTT samples as a function of temperature. Vertical marks are the values obtained from GOP-temperature rescaling. Horizontal dashed line marks the condition $\tau = t$

semi-crystalline PE at $T = 300$ K. From the analysis of chemical shifts, the value of $x_t = 0.6$ ($x_{tt} = 0.36$) is extracted, which is in good agreement with previous simulation results.

Simulated trans/gauche populations in PBTTT, presented in this chapter, are notably different ($x_{tt} \approx 0.5$ at $T = 450$ K). One possibility for this discrepancy is poor equilibration of side-chains due to short simulation times. To check this, one can calculate the number of transitions between conformers (see fig. 4.11) in intermediate and amorphous mesophases at various temperatures. Even at $T = 300$ K, more than half of side-chains have more than 25 transitions between trans and gauche conformers, which should be sufficient to reach an equilibrium. Further, though two mesophase are prepared independently, the observed dynamics is identical. This shows that disordered side-chains have similar properties in two mesophases and are equilibrated. This is additionally supported by previous simulations of PE, [235, 242], where the characteristic transition time between two conformers was found to be of the order of $\tau = 0.1$ ns. This relaxation time is much smaller than the simulation time of PBTTT mesophases (2 ns).

Another possibility is that the OPLS-AA force field parameterization does not reproduce the conformer statistics, hence, it is not suitable for such side-chains simulations. In fact, recently, a new OPLS parameterization for dihedral potentials of long hydrocarbons was obtained [243], which focuses on reproducing the energy barriers between conformer states, and may give better trans/gauche populations. Simulations with new dihedral parameters are left for future investigation. Even in this case, the protocol employed in Section 4.5 is valid, as it partially corrects the population of trans/gauche conformers, since in equilibrium the Boltzmann factor holds: $x_t/x_g \approx \exp(-\Delta E/k_B T)$. Here, ΔE is the difference between two energy levels, k_B is the Boltzmann constant and T is the temperature.

Even so, it is clear now, how solid-state NMR overestimates the crystalline mesophase concentration. One can equate disordered "gauche" signals with the amorphous side-chains in the sample, yet one cannot judge about the ordered chains only from the ordered part of the NMR spectrum. From (tab. 4.4) one can see that (tt) conformers are dominant in all three mesophases, including the two with disordered side-chains. As a reminder, in NMR the following values were assumed: $t_c \approx 1$ and $t_a \approx t_i \approx 0$. However, judging from simulations, these values are never met. The observed *crystalline* peak in the NMR spectrum is unresolved as it contains contributions from all three mesophases. Also, it does not take into account

Time [ns]	1.0			1.3×10^5			$t \to \infty$		
Conformers	tt	tg	gg	tt	tg	gg	tt	tg	gg
cryst.	0.992	0.008	0.000	0.955	0.045	0.000	0.944	0.055	0.001
inter.	0.640	0.314	0.046	0.513	0.406	0.081	0.474	0.430	0.096
amorph.	0.597	0.336	0.067	0.503	0.407	0.090	0.454	0.438	0.108

Table 4.4: Conformers populations, calculated for three timescales of side-chain dynamics in three mesophases. Two timescales are extrapolated from high temperature re-mapped dynamics.

the connection of main chains and side-chains within those mesophases. The initial 1:1 crystalline/amorphous mesophase composition is only one possible interpretation of the NMR data where $\tau = 0$. Yet, according to simulations (tab. 4.4) and further analysis, this scenario is unrealistic. Here, MD simulations provide the missing link, and the conformer analysis plays a key role in resolving the composition problem.

4.6.5 Qualitative estimates of the composition

Finally, it is interesting to look at the numerical quantities of mesophase fractions, that come out of two proposed models, provided the missing parameters t_α.

The first case follows the lead of the NMR experiment and suggests that there are only two mesophases (crystalline and amorphous), mixed in a proportion, close to 1:1. In terms of the model, this translates to concentrations of crystalline and amorphous mesophases as $n_c = n_a = 0.5 - x$ while $n_i = 2x$ and is expected to be small. Within this setup, the concentration of the intermediate mesophase takes the form

$$n_i = \frac{t_c + \tau - 2t}{t_c - \tau}, \tag{4.40}$$

where t_α ($\alpha = c, i, a$) are side-chain (tt) conformer probabilities, estimated from MD. Concentration n_c is then calculated as $n_c = 0.5 - n_i/2$ for three simulation times: short runs (1 ns), runs with experiment-like dynamics (130 μs) and fully equilibrated runs ($t \to \infty$). Each simulated timescale provides useful information about the system. The results are summarized in (tab. 4.5).

At short simulation times ($t = 1$ ns), calculated concentrations of the crystalline and amorphous mesophases are $n_c = n_a = -29.1\%$ (i.e. $n_c < 0$). This was already demonstrated in Section 4.6.3: Since $\tau > t$, the negative values of n_c are expected. The origin of the problem has a number of sources.

Rescaled μs runs recover a positive value $n_c = n_a = 8.5\%$. This is a result of a controlled high temperature dynamics, which allows side-chains to diffuse and approach their equilibrium distributions. Yet, there is still a number of concerns. The small values of n_c and n_a are in direct contradiction with the initial assumption about mesophase composition: 83% of the sample is occupied by the intermediate mesophase (and not the other two). Additionally, because material composition is an equilibrium property, it is possible that one still has not reached the equilibrium.

Previously, one suggested that the equilibrium values are recovered from 500 K runs and generate the highest possible number of defects. This is directly linked to the highest possible value of the crystalline and amorphous mesophases, $n_c = n_a = 16.9\%$. Consequently, the smallest portion of the intermediate mesophase, which is consistent with the model and experimental measurements, is $n_i = 66.2\%$ and cannot be further reduced to zero. Even when the equilibration problem is resolved, still, the two-mesophase picture is inappropriate. The expected composition value $n_i \approx 0\%$ cannot be reached within the physical range of available parameters of the model. The next step is to introduce mesophases without restraints.

The model is revised to allow arbitrary fractions of mesophases, which still satisfy the experimental observations. This is achieved through a set of constraints: $n_c + n_i = 0.5$ and $n_a = 0.5$. As a results, the crystalline mesophase fraction is given by

$$n_c = \frac{t - \tau}{t_c - \tau}, \tag{4.41}$$

It is then calculated for three simulation times. The short simulations yield negative probabilities for some mesophases due to bad equilibration. The rescaled μs run provides a better value $n_c = 9.5\%$ and the fully equilibrated run gives $n_c = 18.3\%$.

The final adjustment comes from another NMR observation: The (gg) conformers are not observed in the experiments. This effect was already taken into account when the model was derived, but parameter distributions, used until now, were not adjusted. Such rescaling systematically reduces equilibrium concentrations by more then a factor of two down to 6.4% and 8.0% in two scenarios (see tab. 4.5 for a complete set of changes).

As a side note, it was shown in Section 4.6.4 that side-chain conformer populations may not be well reproduced in current PBTTT mesophase simulations. Using the estimates from PE melt simulations, one arrives at higher number of 30%. Further simulations and analysis are required to check this result.

This leads to the conclusion, that within the proposed model and conducted MD simulations, simulated microscopic parameters and experimental data, the highest possible concentration of a crystalline mesophase is limited by 8%. The final distribution for crystalline, intermediate and amorphous mesophases is 8%, 42% and 50%. Not only PBTTT is far from crystalline, but also the fraction of crystallites in the sample is not enough to form the percolation network (around 50%) required for an efficient charge transport via hopping. Further more, from the organic electronics perspective, one needs to consider other mesophases and suitable charge transfer mechanisms to explain high efficiencies of PBTTT-based devices.

As a consequence of this finding, it is useful to decompose the NMR signal with respect to its mesophase origin. Taking into account the calculated defect fractions of side-chains, one obtains that out of total 55% (tt) conformers contained in the sample, only 7.5% come from fully crystalline mesophase, while 22% are located in intermediate mesophase and 25.5% are in amorphous mesophase (majority). This shows that each portion of a sample possesses a relevant amount of (tt) conformers (not only crystallites). In the case of PBTTT, similar fractions of crystallized backbones (50%) and “crystallized” side-chains (55%) is merely

time	case 1		case 2	
Statistics	Full	Reduced	Full	Reduced
$t = 1$ ns	-29.1%	-41.7%	-19.5%	-32.9%
$t = 1.3 \times 10^5$ ns	$+8.6\%$	-2.0%	$+9.5\%$	-1.4%
$t = \infty$ ns	$+16.9\%$	$+6.4\%$	$+18.3\%$	$+8.0\%$

Table 4.5: Fraction of the crystalline mesophase n_c obtained for two scenarios: Case 1 with the two-mesophase composition, and Case 2 with the three-mesophase composition. Results for full and reduced statistics are included.

a coincidence. Consequently, (tt) to (tg) ratio of side-chain conformer cannot be directly converted to the ordered/disordered mesophase ratio. The derived expression (eq. 4.41), however, partially resolves this issue and provides an estimate for the crystalline mesophase in the sample. This approach could work for other polymers with similar structure, since simulated microscopic parameters are local in nature, hence, should be transferable. Further investigation of the above statements is left fors the future work.

4.7 Conclusions

In this chapter, a number of properties of the semi-crystalline PBTTT-C16 polymer are studied, such as local packing, backbone and side-chain dynamics, and macroscopic composition. These properties are investigated using NMR measurements and MD simulations.

The simulated local packing in three mesophases is in good agreement with partially resolved NMR data and includes unit cell parameters, d-spacing between polymers, methyl-to-backbone distances and mean torsion angles of backbones. The absence of experimental data in amorphous regions is mirrored by observed flat distributions of parameters in simulated disordered morphologies.

Dynamics of PBTTT mesophases is revealed through Lipari-Szabo generalized order parameters via both NMR experiments and MD simulations. While simulated chain dynamics agrees with experimental data qualitatively, the dynamics of side-chains is slowed down by a factor of two. To enhance sampling, the PBTTT dynamics is extrapolated from short (ns) high temperature production runs. Matching generalized order parameters from SS-NMR and simulations, allows to reproduce the side-chains dynamics, which corresponds to the μs-long averages. In particular, elevated temperatures induce diffusion in a controlled fashion due to a more effective barrier crossing and defect formation.

In the macroscopic PBTTT sample, two mesophases are observed experimentally: Crystalline and amorphous. In these mesophases, side-chain defects and backbone disorder are related to macroscopic properties of the sample. Fitting of the resolved NMR spectrum suggests the $1:1$ ratio of these two mesophases.

An investigation through MD simulations revealed that three mesophases can be simulated: Crystalline, intermediate and amorphous. The intermediate mesophase is comprised of π-stacked backbones and disordered side-chains. It was shown that the *two-mesophase* composition, proposed in NMR, is inconsistent within the derived model. The *three-mesophase* model combined with the NMR-based macroscopic parameters and microscopic parameters

from MD simulations leads to significant changes in the initial concentration assessment: 50% of material is amorphous, 42% is intermediate and 8% is crystallized.

A simple analytical formula is derived to assess the crystalline fraction in a sample. Because simulated microscopic parameters are independent of the backbone packing, the derived model and its microscopic parameters can be used to estimate the crystalline fraction in other semi-crystalline polymers with a similar structure.

High temperature MD simulations, used for controlled equilibration of amorphous side-chains in two mesophases, play an important role in macroscopic composition assessment. Short simulation times (1 ns vs 130 μs) lead not only to a restrained dynamics, but also to unbalanced defect concentrations, which can result in an unphysical mesophase fractions. Alternatively, incomplete force field parameterization could be responsible for an incorrect conformer statistics.

Even in well equilibrated systems, MD simulations reveal that the majority of trans-signals, measured in the sample, come from disordered chains. Out of total 55%, attributed to the crystalline peak, only 7% originates from side-chains in the crystalline mesophase, while the remaining 48% (i.e. $22\% + 26\%$) arise from disordered chains in the intermediate and amorphous mesophases.

5 Summary and outlook

Polymer solar cells have the potential to become an economically viable, environmentally friendly alternative to fossil fuels. Multiple solar cell types are spawned by a vast choice of materials that can be used in the active layer of photovoltaic devices. One possibility is to use conjugated polymers. They combine good light absorption, high mobilities, chemical flexibility, low specific weight, transparency, large-scale printing techniques and, potentially, low production costs.

Current efficient polymers, however, have complex chemistry and structure. This results in a large number of degrees of freedom, which lead to multiple ordered (crystalline) and disordered (melts) packing motifs. Local packing has a strong influence on the electronic and transport properties of a polymer. In order to improve the solar cell efficiency, one needs to understand the effect of morphology, as well as be able to control morphology formation.

In this thesis, I used a number of simulation techniques to study the morphology effects in two conjugated polymers. Since the processes of interest are microscopic in nature, a multiscale approach was used to link the local properties to a macroscopic observable, that is mobility. These techniques include first-principles calculations, molecular dynamics simulations, perturbative energy calculations, and Marcus charge transfer theory. With these simulation methods, two polymers, PCPDTBT and PBTTT, were investigated.

In PCPDTBT, it was shown that the possible morphologies of the polymer go beyond the two typical motives: amorphous and π-stacked. In fact, four crystalline polymorphs have been observed. In this work, I attempted to use molecular dynamics simulations to derive these polymorphs systematically in a bottom-up approach, through analysis of monomer, dimer, and tetramer interactions. Not one, but two π-stacked structures were discovered in PCPDTBT. Two more crystals are side-chain mediated, i.e. their side-chains are folded on the backbones. Such side-chain packing results in different charge transport pathways in the system. Furthermore, charge transport was investigated using Marcus charge transfer theory. It was shown that the energetics of charges is generated by the electrostatics of the donor unit CPD, as well as a disordered structure of side-chains. Large variation of site energies results in low mobilities. Moreover, atom substitution was considered: Heavy atom substitution (Si, Ge) of the bridging atom in the donor unit, as well as fluorination of the acceptor unit. Both substitution patterns favor higher energetic disorder and reduce mobilities.

A number of improvements can be proposed. In this work, in order to find possible crystal structures, the total energy was used. However, the morphology formation is driven by the free energy of the system. It would be interesting to perform free energy calculations and compare the results of two approaches. Additionally, one should check if these calculations would be able to predict metastable conformations of other complex conjugated polymers. Also, it was demonstrated that the transfer integral evaluation is the bottleneck of the charge

transport simulations, which is a consequence of time-consuming DFT calculations. One could attempt to re-parameterize semi-empirical quantum chemistry methods in order to reduce the computation time.

PBTTT is a typical donor material for organic solar cells due its high crystallinity, hence, good charge transport. As a result, often only the crystalline part is considered when its properties are investigated. However, the solid-state NMR measurements show that half of the PBTTT sample is, in fact, amorphous. This result is not resolved with respect to its mesophases, so I combined microscopic molecular dynamics simulations of PBTTT with the available NMR data to resolve the composition. A simple equation was derived, which allows one to assess the fraction of crystalline domains. It contains *microscopic* concentrations of side-chain trans conformers, obtained from simulations, and the *macroscopic* average of the same quantity, measured in the solid-state NMR. For a given PBTTT sample, a three-mesophase composition results in the crystalline domain concentration of 8%, i.e. the disordered mesophase and the interface are dominant. Hence, disordered regions define the physical properties of PBTTT sample. This result should be further investigated for other polymer systems with similar structure, such as P3HT, and compared to other methods.

Bibliography

[1] D. M. Chapin, C. S. Fuller, and G. L. Pearson. „A New Silicon p-n Junction Photocell for Converting Solar Radiation into Electrical Power“. In: *Journal of Applied Physics* 25.5 (May 1954), pp. 676–677. DOI: 10.1063/1.1721711.

[2] K. L. Chopra, P. D. Paulson, and V. Dutta. „Thin-film solar cells: an overview“. en. In: *Progress in Photovoltaics: Research and Applications* 12.2-3 (Mar. 2004), pp. 69–92. DOI: 10.1002/pip.541.

[3] Martin A. Green et al. „Solar cell efficiency tables (Version 45)“. en. In: *Progress in Photovoltaics: Research and Applications* 23.1 (Jan. 2015), pp. 1–9. DOI: 10.1002/pip.2573.

[4] *NREL: National Center for Photovoltaics Home Page*. URL: http://www.nrel.gov/ncpv/.

[5] D. E. Carlson and C. R. Wronski. „Amorphous silicon solar cell“. In: *Applied Physics Letters* 28.11 (June 1976), pp. 671–673. DOI: 10.1063/1.88617.

[6] A. Shah et al. „Photovoltaic Technology: The Case for Thin-Film Solar Cells“. en. In: *Science* 285.5428 (July 1999), pp. 692–698. DOI: 10.1126/science.285.5428.692.

[7] Amaresh Mishra and Peter Bäuerle. „Small Molecule Organic Semiconductors on the Move: Promises for Future Solar Energy Technology“. en. In: *Angewandte Chemie International Edition* 51.9 (Feb. 2012), pp. 2020–2067. DOI: 10.1002/anie.201102326.

[8] Yuze Lin, Yongfang Li, and Xiaowei Zhan. „Small molecule semiconductors for high-efficiency organic photovoltaics“. en. In: *Chemical Society Reviews* 41.11 (May 2012), pp. 4245–4272. DOI: 10.1039/C2CS15313K.

[9] Gilles Dennler, Markus C. Scharber, and Christoph J. Brabec. „Polymer-Fullerene Bulk-Heterojunction Solar Cells“. en. In: *Advanced Materials* 21.13 (Apr. 2009), pp. 1323–1338. DOI: 10.1002/adma.200801283.

[10] Christoph J. Brabec et al. „Polymer–Fullerene Bulk-Heterojunction Solar Cells“. en. In: *Advanced Materials* 22.34 (Sept. 2010), pp. 3839–3856. DOI: 10.1002/adma.200903697.

[11] Gang Li, Rui Zhu, and Yang Yang. „Polymer solar cells“. en. In: *Nature Photonics* 6.3 (Mar. 2012), pp. 153–161. DOI: 10.1038/nphoton.2012.11.

[12] Prashant V. Kamat. „Quantum Dot Solar Cells. Semiconductor Nanocrystals as Light Harvesters†“. In: *The Journal of Physical Chemistry C* 112.48 (Dec. 2008), pp. 18737–18753. DOI: 10.1021/jp806791s.

[13] Dmitri V. Talapin et al. „Prospects of Colloidal Nanocrystals for Electronic and Optoelectronic Applications“. In: *Chemical Reviews* 110.1 (Jan. 2010), pp. 389–458. DOI: 10.1021/cr900137k.

[14] Martin A. Green, Anita Ho-Baillie, and Henry J. Snaith. „The emergence of perovskite solar cells“. en. In: *Nature Photonics* 8.7 (July 2014), pp. 506–514. DOI: 10.1038/nphoton.2014.134.

[15] Samrana Kazim et al. „Perovskite as Light Harvester: A Game Changer in Photovoltaics“. en. In: *Angewandte Chemie International Edition* 53.11 (Mar. 2014), pp. 2812–2824. DOI: 10.1002/anie.201308719.

[16]Tze Chien Sum and Nripan Mathews. „Advancements in perovskite solar cells: photophysics behind the photovoltaics“. en. In: *Energy & Environmental Science* 7.8 (July 2014), pp. 2518–2534. DOI: 10.1039/C4EE00673A.

[17]William Shockley and Hans J. Queisser. „Detailed Balance Limit of Efficiency of p-n Junction Solar Cells“. In: *Journal of Applied Physics* 32.3 (Mar. 1961), pp. 510–519. DOI: 10.1063/1.1736034.

[18]Chun-Chao Chen et al. „An Efficient Triple-Junction Polymer Solar Cell Having a Power Conversion Efficiency Exceeding 11%“. en. In: *Advanced Materials* 26.32 (Aug. 2014), pp. 5670–5677. DOI: 10.1002/adma.201402072.

[19]Zhicai He et al. „Enhanced power-conversion efficiency in polymer solar cells using an inverted device structure“. en. In: *Nature Photonics* 6.9 (Sept. 2012), pp. 591–595. DOI: 10.1038/nphoton.2012.190.

[20]Yongye Liang et al. „For the Bright Future—Bulk Heterojunction Polymer Solar Cells with Power Conversion Efficiency of 7.4%“. en. In: *Advanced Materials* 22.20 (May 2010), E135–E138. DOI: 10.1002/adma.200903528.

[21]Jingbi You et al. „A polymer tandem solar cell with 10.6% power conversion efficiency“. en. In: *Nature Communications* 4 (Feb. 2013), p. 1446. DOI: 10.1038/ncomms2411.

[22]Sung Heum Park et al. „Bulk heterojunction solar cells with internal quantum efficiency approaching 100%“. en. In: *Nature Photonics* 3.5 (May 2009), pp. 297–302. DOI: 10.1038/nphoton.2009.69.

[23]Martijn Kuik et al. „25th Anniversary Article: Charge Transport and Recombination in Polymer Light-Emitting Diodes“. en. In: *Advanced Materials* 26.4 (Jan. 2014), pp. 512–531. DOI: 10.1002/adma.201303393.

[24]C. W. Tang. „Two-layer organic photovoltaic cell“. In: *Applied Physics Letters* 48.2 (Jan. 1986), pp. 183–185. DOI: 10.1063/1.96937.

[25]P. W. M. Blom et al. „Device Physics of Polymer:Fullerene Bulk Heterojunction Solar Cells“. en. In: *Advanced Materials* 19.12 (June 2007), pp. 1551–1566. DOI: 10.1002/adma.200601093.

[26]G. Yu et al. „Polymer Photovoltaic Cells: Enhanced Efficiencies via a Network of Internal Donor-Acceptor Heterojunctions“. en. In: *Science* 270.5243 (Dec. 1995), pp. 1789–1791. DOI: 10.1126/science.270.5243.1789.

[27]Ming He, Feng Qiu, and Zhiqun Lin. „Conjugated rod–coil and rod–rod block copolymers for photovoltaic applications“. en. In: *Journal of Materials Chemistry* 21.43 (Oct. 2011), pp. 17039–17048. DOI: 10.1039/C1JM11518A.

[28]Serap Günes, Helmut Neugebauer, and Niyazi Serdar Sariciftci. „Conjugated Polymer-Based Organic Solar Cells“. In: *Chemical Reviews* 107.4 (Apr. 2007), pp. 1324–1338. DOI: 10.1021/cr050149z.

[29]M. M. Mandoc, L. J. A. Koster, and P. W. M. Blom. „Optimum charge carrier mobility in organic solar cells“. In: *Applied Physics Letters* 90.13 (Mar. 2007), p. 133504. DOI: 10.1063/1.2711534.

[30]Patrick Boland, Keejoo Lee, and Gon Namkoong. „Device optimization in PCPDTBT:PCBM plastic solar cells“. In: *Solar Energy Materials and Solar Cells* 94.5 (May 2010), pp. 915–920. DOI: 10.1016/j.solmat.2010.01.022.

[31]Uli Würfel et al. „Impact of charge transport on current-voltage characteristics and power-conversion efficiency of organic solar cells“. en. In: *Nature Communications* 6 (Apr. 2015), p. 6951. DOI: 10.1038/ncomms7951.

[32]Jan C. Hummelen et al. „Preparation and Characterization of Fulleroid and Methanofullerene Derivatives“. In: *The Journal of Organic Chemistry* 60.3 (Feb. 1995), pp. 532–538. DOI: 10.1021/jo00108a012.

[33] Shigenori Morita, Anvar A Zakhidov, and Katsumi Yoshino. „Doping effect of buckminsterfullerene in conducting polymer: Change of absorption spectrum and quenching of luminescene“. In: *Solid State Communications* 82.4 (Apr. 1992), pp. 249–252. DOI: 10.1016/0038-1098(92)90636-N.

[34] N. S. Sariciftci et al. „Photoinduced Electron Transfer from a Conducting Polymer to Buckminsterfullerene“. en. In: *Science* 258.5087 (Nov. 1992), pp. 1474–1476. DOI: 10.1126/science.258.5087.1474.

[35] Sean E. Shaheen et al. „2.5% efficient organic plastic solar cells“. In: *Applied Physics Letters* 78.6 (Feb. 2001), pp. 841–843. DOI: 10.1063/1.1345834.

[36] Yongfang Li. „Molecular Design of Photovoltaic Materials for Polymer Solar Cells: Toward Suitable Electronic Energy Levels and Broad Absorption“. In: *Accounts of Chemical Research* 45.5 (May 2012), pp. 723–733. DOI: 10.1021/ar2002446.

[37] Frederik C. Krebs. „Fabrication and processing of polymer solar cells: A review of printing and coating techniques“. In: *Solar Energy Materials and Solar Cells*. Processing and Preparation of Polymer and Organic Solar Cells 93.4 (Apr. 2009), pp. 394–412. DOI: 10.1016/j.solmat.2008.10.004.

[38] Frederik C. Krebs, Thomas Tromholt, and Mikkel Jørgensen. „Upscaling of polymer solar cell fabrication using full roll-to-roll processing“. en. In: *Nanoscale* 2.6 (June 2010), pp. 873–886. DOI: 10.1039/B9NR00430K.

[39] Martijn M. Wienk et al. „Efficient Methano[70]fullerene/MDMO-PPV Bulk Heterojunction Photovoltaic Cells“. en. In: *Angewandte Chemie* 115.29 (July 2003), pp. 3493–3497. DOI: 10.1002/ange.200351647.

[40] F. Padinger, R.s. Rittberger, and N.s. Sariciftci. „Effects of Postproduction Treatment on Plastic Solar Cells“. en. In: *Advanced Functional Materials* 13.1 (Jan. 2003), pp. 85–88. DOI: 10.1002/adfm.200390011.

[41] Zhengguo Zhu et al. „Panchromatic Conjugated Polymers Containing Alternating Donor/Acceptor Units for Photovoltaic Applications“. In: *Macromolecules* 40.6 (Mar. 2007), pp. 1981–1986. DOI: 10.1021/ma062376o.

[42] Yen-Ju Cheng, Sheng-Hsiung Yang, and Chain-Shu Hsu. „Synthesis of Conjugated Polymers for Organic Solar Cell Applications“. In: *Chemical Reviews* 109.11 (Nov. 2009), pp. 5868–5923. DOI: 10.1021/cr900182s.

[43] René A. J. Janssen and Jenny Nelson. „Factors Limiting Device Efficiency in Organic Photovoltaics“. en. In: *Advanced Materials* 25.13 (Apr. 2013), pp. 1847–1858. DOI: 10.1002/adma.201202873.

[44] Tayebeh Ameri et al. „Organic tandem solar cells: A review“. en. In: *Energy & Environmental Science* 2.4 (Mar. 2009), pp. 347–363. DOI: 10.1039/B817952B.

[45] C. H. Henry. „Limiting efficiencies of ideal single and multiple energy gap terrestrial solar cells“. In: *Journal of Applied Physics* 51.8 (Aug. 1980), pp. 4494–4500. DOI: 10.1063/1.328272.

[46] Mikkel Jørgensen, Kion Norrman, and Frederik C. Krebs. „Stability/degradation of polymer solar cells“. In: *Solar Energy Materials and Solar Cells*. Degradation and Stability of Polymer and Organic Solar Cells 92.7 (July 2008), pp. 686–714. DOI: 10.1016/j.solmat.2008.01.005.

[47] Mikkel Jørgensen et al. „Stability of Polymer Solar Cells“. en. In: *Advanced Materials* 24.5 (Feb. 2012), pp. 580–612. DOI: 10.1002/adma.201104187.

[48] Julia Schafferhans et al. „Oxygen doping of P3HT:PCBM blends: Influence on trap states, charge carrier mobility and solar cell performance“. In: *Organic Electronics* 11.10 (Oct. 2010), pp. 1693–1700. DOI: 10.1016/j.orgel.2010.07.016.

[49]E. Schrödinger. „An Undulatory Theory of the Mechanics of Atoms and Molecules“. In: *Physical Review* 28.6 (Dec. 1926), pp. 1049–1070. DOI: 10.1103/PhysRev.28.1049.

[50]Per-Olov Löwdin. „On the Non-Orthogonality Problem Connected with the Use of Atomic Wave Functions in the Theory of Molecules and Crystals“. In: *The Journal of Chemical Physics* 18.3 (Mar. 1950), pp. 365–375. DOI: 10.1063/1.1747632.

[51]ISAIAH SHAVITT. „The history and evolution of configuration interaction“. In: *Molecular Physics* 94.1 (May 1998), pp. 3–17. DOI: 10.1080/002689798168303.

[52]Chr. Møller and M. S. Plesset. „Note on an Approximation Treatment for Many-Electron Systems“. In: *Physical Review* 46.7 (Oct. 1934), pp. 618–622. DOI: 10.1103/PhysRev.46.618.

[53]Rodney J. Bartlett and Monika Musiał. „Coupled-cluster theory in quantum chemistry“. In: *Reviews of Modern Physics* 79.1 (Feb. 2007), pp. 291–352. DOI: 10.1103/RevModPhys.79.291.

[54]P. Hohenberg and W. Kohn. „Inhomogeneous Electron Gas“. In: *Physical Review* 136.3B (Nov. 1964), B864–B871. DOI: 10.1103/PhysRev.136.B864.

[55]Ralf Stowasser and Roald Hoffmann. „What Do the Kohn-Sham Orbitals and Eigenvalues Mean?“ In: *Journal of the American Chemical Society* 121.14 (Apr. 1999), pp. 3414–3420. DOI: 10.1021/ja9826892.

[56]John P. Perdew, Matthias Ernzerhof, and Kieron Burke. „Rationale for mixing exact exchange with density functional approximations“. In: *The Journal of Chemical Physics* 105.22 (Dec. 1996), pp. 9982–9985. DOI: 10.1063/1.472933.

[57]Axel D. Becke. „Density-functional thermochemistry. III. The role of exact exchange“. In: *The Journal of Chemical Physics* 98.7 (Apr. 1993), pp. 5648–5652. DOI: 10.1063/1.464913.

[58]P. J. Stephens et al. „Ab Initio Calculation of Vibrational Absorption and Circular Dichroism Spectra Using Density Functional Force Fields“. In: *The Journal of Physical Chemistry* 98.45 (Nov. 1994), pp. 11623–11627. DOI: 10.1021/j100096a001.

[59]S. H. Vosko, L. Wilk, and M. Nusair. „Accurate spin-dependent electron liquid correlation energies for local spin density calculations: a critical analysis“. In: *Canadian Journal of Physics* 58.8 (Aug. 1980), pp. 1200–1211. DOI: 10.1139/p80-159.

[60]Chengteh Lee, Weitao Yang, and Robert G. Parr. „Development of the Colle-Salvetti correlation-energy formula into a functional of the electron density“. In: *Physical Review B* 37.2 (Jan. 1988), pp. 785–789. DOI: 10.1103/PhysRevB.37.785.

[61]Daan Frenkel and Berend Smit. *Understanding Molecular Simulation, Second Edition: From Algorithms to Applications*. English. 2 edition. San Diego: Academic Press, Nov. 2001. ISBN: 978-0-12-267351-1.

[62]Frank Jensen. *Introduction to Computational Chemistry*. English. 2 edition. Chichester, England ; Hoboken, NJ: Wiley, 2007. ISBN: 978-0-470-01187-4.

[63]B. J. Alder and T. E. Wainwright. „Studies in Molecular Dynamics. I. General Method“. In: *The Journal of Chemical Physics* 31.2 (Aug. 1959), pp. 459–466. DOI: 10.1063/1.1730376.

[64]A. Rahman. „Correlations in the Motion of Atoms in Liquid Argon“. In: *Physical Review* 136.2A (Oct. 1964), A405–A411. DOI: 10.1103/PhysRev.136.A405.

[65]R. Car and M. Parrinello. „Unified Approach for Molecular Dynamics and Density-Functional Theory“. In: *Physical Review Letters* 55.22 (Nov. 1985), pp. 2471–2474. DOI: 10.1103/PhysRevLett.55.2471.

[66]Anders M. N. Niklasson, C. J. Tymczak, and Matt Challacombe. „Time-Reversible Born-Oppenheimer Molecular Dynamics“. In: *Physical Review Letters* 97.12 (Sept. 2006), p. 123001. DOI: 10.1103/PhysRevLett.97.123001.

[67] Gary B. Adams et al. „Polymerized ${\mathrm{C}}_{60}$ studied by first-principles molecular dynamics“. In: *Physical Review B* 50.23 (Dec. 1994), pp. 17471–17479. DOI: 10.1103/PhysRevB.50.17471.

[68] P. J. D. Lindan et al. „First-principles molecular dynamics simulation of water dissociation on TiO2 (110)“. In: *Chemical Physics Letters* 261.3 (Oct. 1996), pp. 246–252. DOI: 10.1016/0009-2614(96)00934-7.

[69] Kevin T. Chan, J. B. Neaton, and Marvin L. Cohen. „First-principles study of metal adatom adsorption on graphene“. In: *Physical Review B* 77.23 (June 2008), p. 235430. DOI: 10.1103/PhysRevB.77.235430.

[70] *PumMa » Theory » Potentials*.

[71] E. Bright Wilson Jr, J. C. Decius, and Paul C. Cross. *Molecular Vibrations: The Theory of Infrared and Raman Vibrational Spectra*. English. Revised ed. edition. New York: Dover Publications, Mar. 1980. ISBN: 978-0-486-63941-3.

[72] William L. Jorgensen and Julian. Tirado-Rives. „The OPLS [optimized potentials for liquid simulations] potential functions for proteins, energy minimizations for crystals of cyclic peptides and crambin“. In: *Journal of the American Chemical Society* 110.6 (Mar. 1988), pp. 1657–1666. DOI: 10.1021/ja00214a001.

[73] William L. Jorgensen, David S. Maxwell, and Julian Tirado-Rives. „Development and Testing of the OPLS All-Atom Force Field on Conformational Energetics and Properties of Organic Liquids“. In: *Journal of the American Chemical Society* 118.45 (Jan. 1996), pp. 11225–11236. DOI: 10.1021/ja9621760.

[74] William L. Jorgensen and Nora A. McDonald. „Development of an all-atom force field for heterocycles. Properties of liquid pyridine and diazenes“. In: *Journal of Molecular Structure: THEOCHEM*. A Faithful Couple: Qualitative and Quantitative Understanding of Chemistry 424.1–2 (Feb. 1998), pp. 145–155. DOI: 10.1016/S0166-1280(97)00237-6.

[75] Nora A. McDonald and William L. Jorgensen. „Development of an All-Atom Force Field for Heterocycles. Properties of Liquid Pyrrole, Furan, Diazoles, and Oxazoles“. In: *The Journal of Physical Chemistry B* 102.41 (Oct. 1998), pp. 8049–8059. DOI: 10.1021/jp981200o.

[76] Wendy D. Cornell et al. „A Second Generation Force Field for the Simulation of Proteins, Nucleic Acids, and Organic Molecules“. In: *Journal of the American Chemical Society* 117.19 (May 1995), pp. 5179–5197. DOI: 10.1021/ja00124a002.

[77] Curt M. Breneman and Kenneth B. Wiberg. „Determining atom-centered monopoles from molecular electrostatic potentials. The need for high sampling density in formamide conformational analysis“. en. In: *Journal of Computational Chemistry* 11.3 (Apr. 1990), pp. 361–373. DOI: 10.1002/jcc.540110311.

[78] Brent H. Besler, Kenneth M. Merz, and Peter A. Kollman. „Atomic charges derived from semiempirical methods“. en. In: *Journal of Computational Chemistry* 11.4 (May 1990), pp. 431–439. DOI: 10.1002/jcc.540110404.

[79] Thirumurthy Madhavan et al. „Various atomic charge calculation schemes of CoMFA on HIF-1 inhibitors of moracin analogs“. en. In: *International Journal of Quantum Chemistry* 112.4 (Feb. 2012), pp. 995–1005. DOI: 10.1002/qua.23084.

[80] Emma Sigfridsson and Ulf Ryde. „Comparison of methods for deriving atomic charges from the electrostatic potential and moments“. en. In: *Journal of Computational Chemistry* 19.4 (Mar. 1998), pp. 377–395. DOI: 10.1002/(SICI)1096-987X(199803)19:4<377::AID-JCC1>3.0.CO;2-P.

[81] F. Martin and H. Zipse. „Charge distribution in the water molecule—A comparison of methods“. en. In: *Journal of Computational Chemistry* 26.1 (Jan. 2005), pp. 97–105. DOI: 10.1002/jcc.20157.

[82] Christopher M. Baker. „Polarizable force fields for molecular dynamics simulations of biomolecules“. en. In: *Wiley Interdisciplinary Reviews: Computational Molecular Science* 5.2 (Mar. 2015), pp. 241–254. DOI: 10.1002/wcms.1215.

[83] Jay W. Ponder et al. „Current Status of the AMOEBA Polarizable Force Field“. In: *The Journal of Physical Chemistry B* 114.8 (Mar. 2010), pp. 2549–2564. DOI: 10.1021/jp910674d.

[84] Victor Rühle et al. „Microscopic Simulations of Charge Transport in Disordered Organic Semiconductors“. In: *Journal of Chemical Theory and Computation* 7.10 (Oct. 2011), pp. 3335–3345. DOI: 10.1021/ct200388s.

[85] Wilfried J. Mortier, Swapan K. Ghosh, and S. Shankar. „Electronegativity-equalization method for the calculation of atomic charges in molecules“. In: *Journal of the American Chemical Society* 108.15 (July 1986), pp. 4315–4320. DOI: 10.1021/ja00275a013.

[86] Sandeep Patel and Charles L. Brooks. „CHARMM fluctuating charge force field for proteins: I parameterization and application to bulk organic liquid simulations“. en. In: *Journal of Computational Chemistry* 25.1 (Jan. 2004), pp. 1–16. DOI: 10.1002/jcc.10355.

[87] Guillaume Lamoureux and Benoit Roux. „Modeling induced polarization with classical Drude oscillators: Theory and molecular dynamics simulation algorithm“. In: *The Journal of Chemical Physics* 119.6 (Aug. 2003), pp. 3025–3039. DOI: 10.1063/1.1589749.

[88] Guillaume Lamoureux, Alexander D. MacKerell Jr, and Benoit Roux. „A simple polarizable model of water based on classical Drude oscillators“. In: *The Journal of Chemical Physics* 119.10 (Sept. 2003), pp. 5185–5197. DOI: 10.1063/1.1598191.

[89] Jon R. Maple et al. „A Polarizable Force Field and Continuum Solvation Methodology for Modeling of Protein-Ligand Interactions“. In: *Journal of Chemical Theory and Computation* 1.4 (July 2005), pp. 694–715. DOI: 10.1021/ct049855i.

[90] Christian Kramer, Alexander Spinn, and Klaus R. Liedl. „Charge Anisotropy: Where Atomic Multipoles Matter Most“. In: *Journal of Chemical Theory and Computation* 10.10 (Oct. 2014), pp. 4488–4496. DOI: 10.1021/ct5005565.

[91] Richard W. Dixon and Peter A. Kollman. „Advancing beyond the atom-centered model in additive and nonadditive molecular mechanics“. en. In: *Journal of Computational Chemistry* 18.13 (Oct. 1997), pp. 1632–1646. DOI: 10.1002/(SICI)1096-987X(199710)18:13<1632::AID-JCC5>3.0.CO;2-S.

[92] B. T. Thole. „Molecular polarizabilities calculated with a modified dipole interaction“. In: *Chemical Physics* 59.3 (Aug. 1981), pp. 341–350. DOI: 10.1016/0301-0104(81)85176-2.

[93] M. Tuckerman, B. J. Berne, and G. J. Martyna. „Reversible multiple time scale molecular dynamics“. In: *The Journal of Chemical Physics* 97.3 (Aug. 1992), pp. 1990–2001. DOI: 10.1063/1.463137.

[94] Loup Verlet. „Computer "Experiments" on Classical Fluids. I. Thermodynamical Properties of Lennard-Jones Molecules“. In: *Physical Review* 159.1 (July 1967), pp. 98–103. DOI: 10.1103/PhysRev.159.98.

[95] H. A. Posch and W. G. Hoover. „Lyapunov instability of dense Lennard-Jones fluids“. In: *Physical Review A* 38.1 (July 1988), pp. 473–482. DOI: 10.1103/PhysRevA.38.473.

[96] Berk Hess et al. „LINCS: A linear constraint solver for molecular simulations“. en. In: *Journal of Computational Chemistry* 18.12 (Sept. 1997), pp. 1463–1472. DOI: 10.1002/(SICI)1096-987X(199709)18:12<1463::AID-JCC4>3.0.CO;2-H.

[97] „A smooth particle mesh Ewald method“. In: *The Journal of Chemical Physics* 103.19 (Nov. 1995), pp. 8577–8593. DOI: 10.1063/1.470117.

[98] „Particle mesh Ewald: An N.log(N) method for Ewald sums in large systems“. In: *The Journal of Chemical Physics* 98.12 (June 1993), pp. 10089–10092. DOI: 10.1063/1.464397.

[99] Giovanni Bussi, Davide Donadio, and Michele Parrinello. „Canonical sampling through velocity rescaling“. In: *The Journal of Chemical Physics* 126.1 (Jan. 2007), p. 014101. DOI: 10.1063/1.2408420.

[100] H. J. C. Berendsen et al. „Molecular dynamics with coupling to an external bath“. In: *The Journal of Chemical Physics* 81.8 (Oct. 1984), pp. 3684–3690. DOI: 10.1063/1.448118.

[101] K. Kreis et al. „Advantages and challenges in coupling an ideal gas to atomistic models in adaptive resolution simulations“. en. In: *The European Physical Journal Special Topics* 224.12 (June 2015), pp. 2289–2304. DOI: 10.1140/epjst/e2015-02412-1.

[102] Michael J. Stephen and Joseph P. Straley. „Physics of liquid crystals“. In: *Reviews of Modern Physics* 46.4 (Oct. 1974), pp. 617–704. DOI: 10.1103/RevModPhys.46.617.

[103] Valentina Marcon et al. „Understanding Structure-Mobility Relations for Perylene Tetracarboxydiimide Derivatives“. In: *Journal of the American Chemical Society* 131.32 (Aug. 2009), pp. 11426–11432. DOI: 10.1021/ja900963v.

[104] Falk May et al. „Relationship between supramolecular assembly and charge-carrier mobility in perylenediimide derivatives: The impact of side chains“. en. In: *Journal of Materials Chemistry* 21.26 (June 2011), pp. 9538–9545. DOI: 10.1039/C1JM10500K.

[105] Valentina Marcon et al. „Columnar mesophases of hexabenzocoronene derivatives. I. Phase transitions“. In: *The Journal of Chemical Physics* 129.9 (Sept. 2008), p. 094505. DOI: 10.1063/1.2969763.

[106] Domenico Alberga et al. „Effects of Annealing and Residual Solvents on Amorphous P3HT and PBTTT Films“. In: *The Journal of Physical Chemistry C* 118.16 (Apr. 2014), pp. 8641–8655. DOI: 10.1021/jp410936t.

[107] Carl Poelking and Denis Andrienko. „Effect of Polymorphism, Regioregularity and Paracrystallinity on Charge Transport in Poly(3-hexylthiophene) [P3HT] Nanofibers“. In: *Macromolecules* 46.22 (Nov. 2013), pp. 8941–8956. DOI: 10.1021/ma4015966.

[108] Carl Poelking et al. „Characterization of Charge-Carrier Transport in Semicrystalline Polymers: Electronic Couplings, Site Energies, and Charge-Carrier Dynamics in Poly(bithiophene-alt-thienothiophene) [PBTTT]“. In: *The Journal of Physical Chemistry C* 117.4 (Jan. 2013), pp. 1633–1640. DOI: 10.1021/jp311160y.

[109] Giovanni Lipari and Attila Szabo. „Model-free approach to the interpretation of nuclear magnetic resonance relaxation in macromolecules. 1. Theory and range of validity“. In: *Journal of the American Chemical Society* 104.17 (Aug. 1982), pp. 4546–4559. DOI: 10.1021/ja00381a009.

[110] Giovanni Lipari and Attila Szabo. „Model-free approach to the interpretation of nuclear magnetic resonance relaxation in macromolecules. 2. Analysis of experimental results“. In: *Journal of the American Chemical Society* 104.17 (Aug. 1982), pp. 4559–4570. DOI: 10.1021/ja00381a010.

[111] P. W. Anderson. „Absence of Diffusion in Certain Random Lattices“. In: *Physical Review* 109.5 (Mar. 1958), pp. 1492–1505. DOI: 10.1103/PhysRev.109.1492.

[112] Sergei Baranovskii and Oleg Rubel. „Charge Transport in Disordered Materials“. en. In: *Springer Handbook of Electronic and Photonic Materials*. Ed. by Safa Kasap Prof and Peter Capper Dr. DOI: 10.1007/978-0-387-29185-7_9. Springer US, 2006, pp. 161–186. ISBN: 978-0-387-26059-4 978-0-387-29185-7.

[113] Hsin-Rong Tseng et al. „High-Mobility Field-Effect Transistors Fabricated with Macroscopic Aligned Semiconducting Polymers“. en. In: *Advanced Materials* 26.19 (May 2014), pp. 2993–2998. DOI: 10.1002/adma.201305084.

[114] Pascal Kordt et al. „Modeling of Organic Light Emitting Diodes: From Molecular to Device Properties“. en. In: *Advanced Functional Materials* 25.13 (Apr. 2015), pp. 1955–1971. DOI: 10.1002/adfm.201403004.

[115]S. V. Novikov et al. „Essential Role of Correlations in Governing Charge Transport in Disordered Organic Materials“. In: *Physical Review Letters* 81.20 (Nov. 1998), pp. 4472–4475. DOI: 10.1103/PhysRevLett.81.4472.

[116]W. F. Pasveer et al. „Unified Description of Charge-Carrier Mobilities in Disordered Semiconducting Polymers“. In: *Physical Review Letters* 94.20 (May 2005), p. 206601. DOI: 10.1103/PhysRevLett.94.206601.

[117]Rudolph A. Marcus. „Electron transfer reactions in chemistry. Theory and experiment“. In: *Reviews of Modern Physics* 65.3 (July 1993), pp. 599–610. DOI: 10.1103/RevModPhys.65.599.

[118]Geoffrey R. Hutchison, Mark A. Ratner, and Tobin J. Marks. „Hopping Transport in Conductive Heterocyclic Oligomers: Reorganization Energies and Substituent Effects“. In: *Journal of the American Chemical Society* 127.7 (Feb. 2005), pp. 2339–2350. DOI: 10.1021/ja0461421.

[119]Volkhard May and Oliver Kühn. *Charge and Energy Transfer Dynamics in Molecular Systems*. English. 3 edition. Weinheim: Wiley-VCH, Mar. 2011. ISBN: 978-3-527-40732-3.

[120]Robert Englman and Joshua Jortner. „The energy gap law for radiationless transitions in large molecules“. In: *Molecular Physics* 18.2 (Feb. 1970), pp. 145–164. DOI: 10.1080/00268977000100171.

[121]Joshua Jortner et al. „Charge transfer and transport in DNA“. en. In: *Proceedings of the National Academy of Sciences* 95.22 (Oct. 1998), pp. 12759–12765. DOI: 10.1073/pnas.95.22.12759.

[122]Hermann Grabert and Ulrich Weiss. „Thermal enhancement of the quantum decay rate in a dissipative system“. en. In: *Zeitschrift für Physik B Condensed Matter* 56.2 (June 1984), pp. 171–183. DOI: 10.1007/BF01469699.

[123]Hermann Grabert and Ulrich Weiss. „Quantum Tunneling Rates for Asymmetric Double-Well Systems with Ohmic Dissipation“. In: *Physical Review Letters* 54.15 (Apr. 1985), pp. 1605–1608. DOI: 10.1103/PhysRevLett.54.1605.

[124]Hermann Grabert, Peter Olschowski, and Ulrich Weiss. „Quantum decay rates for dissipative systems at finite temperatures“. In: *Physical Review B* 36.4 (Aug. 1987), pp. 1931–1951. DOI: 10.1103/PhysRevB.36.1931.

[125]Victor Rühle et al. „Versatile Object-Oriented Toolkit for Coarse-Graining Applications“. In: *Journal of Chemical Theory and Computation* 5.12 (Dec. 2009), pp. 3211–3223. DOI: 10.1021/ct900369w.

[126]Victor Rühle et al. „Microscopic Simulations of Charge Transport in Disordered Organic Semiconductors“. In: *Journal of Chemical Theory and Computation* 7.10 (Oct. 2011), pp. 3335–3345. DOI: 10.1021/ct200388s.

[127]Carl Poelking et al. „Impact of mesoscale order on open-circuit voltage in organic solar cells“. en. In: *Nature Materials* 14.4 (Apr. 2015), pp. 434–439. DOI: 10.1038/nmat4167.

[128]J. Ridley and Michael Zerner. „An intermediate neglect of differential overlap technique for spectroscopy: Pyrrole and the azines“. en. In: *Theoretica chimica acta* 32.2 (June 1973), pp. 111–134. DOI: 10.1007/BF00528484.

[129]Allan D. Bacon and Michael C. Zerner. „An intermediate neglect of differential overlap theory for transition metal complexes: Fe, Co and Cu chlorides“. en. In: *Theoretica chimica acta* 53.1 (Mar. 1979), pp. 21–54. DOI: 10.1007/BF00547605.

[130]J. A. Pople, D. P. Santry, and G. A. Segal. „Approximate Self-Consistent Molecular Orbital Theory. I. Invariant Procedures“. In: *The Journal of Chemical Physics* 43.10 (Nov. 1965), S129–S135. DOI: 10.1063/1.1701475.

[131]J. A. Pople and G. A. Segal. „Approximate Self-Consistent Molecular Orbital Theory. II. Calculations with Complete Neglect of Differential Overlap“. In: *The Journal of Chemical Physics* 43.10 (Nov. 1965), S136–S151. DOI: 10.1063/1.1701476.

[132]J. A. Pople and G. A. Segal. „Approximate Self-Consistent Molecular Orbital Theory. III. CNDO Results for AB2 and AB3 Systems“. In: *The Journal of Chemical Physics* 44.9 (May 1966), pp. 3289–3296. DOI: 10.1063/1.1727227.

[133]D. P. Santry and G. A. Segal. „Approximate Self-Consistent Molecular Orbital Theory. IV. Calculations on Molecules Including the Elements Sodium through Chlorine“. In: *The Journal of Chemical Physics* 47.1 (July 1967), pp. 158–174. DOI: 10.1063/1.1711841.

[134]J. A. Pople, D. L. Beveridge, and P. A. Dobosh. „Approximate Self-Consistent Molecular-Orbital Theory. V. Intermediate Neglect of Differential Overlap“. In: *The Journal of Chemical Physics* 47.6 (Sept. 1967), pp. 2026–2033. DOI: 10.1063/1.1712233.

[135]James Kirkpatrick. „An approximate method for calculating transfer integrals based on the ZINDO Hamiltonian“. en. In: *International Journal of Quantum Chemistry* 108.1 (Jan. 2008), pp. 51–56. DOI: 10.1002/qua.21378.

[136]Xinliang Feng et al. „Towards high charge-carrier mobilities by rational design of the shape and periphery of discotics“. en. In: *Nature Materials* 8.5 (May 2009), pp. 421–426. DOI: 10.1038/nmat2427.

[137]S. I. Gorelsky and A. B. P. Lever. „Electronic structure and spectra of ruthenium diimine complexes by density functional theory and INDO/S. Comparison of the two methods“. In: *Journal of Organometallic Chemistry* 635.1–2 (Oct. 2001), pp. 187–196. DOI: 10.1016/S0022-328X(01)01079-8.

[138]Björn Baumeier, James Kirkpatrick, and Denis Andrienko. „Density-functional based determination of intermolecular charge transfer properties for large-scale morphologies“. en. In: *Physical Chemistry Chemical Physics* 12.36 (Sept. 2010), pp. 11103–11113. DOI: 10.1039/C002337J.

[139]M. Elstner. „The SCC-DFTB method and its application to biological systems“. en. In: *Theoretical Chemistry Accounts* 116.1-3 (Dec. 2005), pp. 316–325. DOI: 10.1007/s00214-005-0066-0.

[140]Tristan Bereau, Denis Andrienko, and O. Anatole von Lilienfeld. „Transferable Atomic Multipole Machine Learning Models for Small Organic Molecules“. In: *Journal of Chemical Theory and Computation* 11.7 (July 2015), pp. 3225–3233. DOI: 10.1021/acs.jctc.5b00301.

[141]Anthony Stone. *The Theory of Intermolecular Forces*. Englisch. 2 Rev ed. Oxford: Oxford University Press, Jan. 2013. ISBN: 978-0-19-967239-4.

[142]U. Chandra Singh and Peter A. Kollman. „An approach to computing electrostatic charges for molecules“. en. In: *Journal of Computational Chemistry* 5.2 (Apr. 1984), pp. 129–145. DOI: 10.1002/jcc.540050204.

[143]Michelle Miller Francl et al. „Charges fit to electrostatic potentials. II. Can atomic charges be unambiguously fit to electrostatic potentials?“ en. In: *Journal of Computational Chemistry* 17.3 (Feb. 1996), pp. 367–383. DOI: 10.1002/(SICI)1096-987X(199602)17:3<367::AID-JCC11>3.0.CO;2-H.

[144]Piet Th. van Duijnen and Marcel Swart. „Molecular and Atomic Polarizabilities: Thole's Model Revisited“. In: *The Journal of Physical Chemistry A* 102.14 (Apr. 1998), pp. 2399–2407. DOI: 10.1021/jp980221f.

[145]Yue Shi et al. „Polarizable Atomic Multipole-Based AMOEBA Force Field for Proteins“. In: *Journal of Chemical Theory and Computation* 9.9 (Sept. 2013), pp. 4046–4063. DOI: 10.1021/ct4003702.

[146]A. B. Bortz, M. H. Kalos, and J. L. Lebowitz. „A new algorithm for Monte Carlo simulation of Ising spin systems“. In: *Journal of Computational Physics* 17.1 (Jan. 1975), pp. 10–18. DOI: 10.1016/0021-9991(75)90060-1.

[147]Daniel T Gillespie. „A general method for numerically simulating the stochastic time evolution of coupled chemical reactions“. In: *Journal of Computational Physics* 22.4 (Dec. 1976), pp. 403–434. DOI: 10.1016/0021-9991(76)90041-3.

[148]Daniel T. Gillespie. „Exact stochastic simulation of coupled chemical reactions“. In: *The Journal of Physical Chemistry* 81.25 (Dec. 1977), pp. 2340–2361. DOI: 10.1021/j100540a008.

[149]Zhicai He et al. „Simultaneous Enhancement of Open-Circuit Voltage, Short-Circuit Current Density, and Fill Factor in Polymer Solar Cells“. en. In: *Advanced Materials* 23.40 (Oct. 2011), pp. 4636–4643. DOI: 10.1002/adma.201103006.

[150]D. Mühlbacher et al. „High Photovoltaic Performance of a Low-Bandgap Polymer“. en. In: *Advanced Materials* 18.21 (Nov. 2006), pp. 2884–2889. DOI: 10.1002/adma.200600160.

[151]C. Soci et al. „Photoconductivity of a Low-Bandgap Conjugated Polymer“. en. In: *Advanced Functional Materials* 17.4 (Mar. 2007), pp. 632–636. DOI: 10.1002/adfm.200600199.

[152]Yongxi Li et al. „Side-Chain Effect on Cyclopentadithiophene/Fluorobenzothiadiazole-Based Low Band Gap Polymers and Their Applications for Polymer Solar Cells“. In: *Macromolecules* 46.14 (July 2013), pp. 5497–5503. DOI: 10.1021/ma4009302.

[153]Florian S. U. Fischer et al. „Structural Models of Poly(cyclopentadithiophene-alt-benzothiadiazole) with Branched Side Chains: Impact of a Single Fluorine Atom on the Crystal Structure and Polymorphism of a Conjugated Polymer“. In: *Macromolecules* 48.12 (June 2015), pp. 3974–3982. DOI: 10.1021/acs.macromol.5b00839.

[154]Chih-Yu Chang et al. „A Versatile Fluoro-Containing Low-Bandgap Polymer for Efficient Semi-transparent and Tandem Polymer Solar Cells“. en. In: *Advanced Functional Materials* 23.40 (Oct. 2013), pp. 5084–5090. DOI: 10.1002/adfm201301557.

[155]Florian S. U. Fischer et al. „Highly Crystalline Films of PCPDTBT with Branched Side Chains by Solvent Vapor Crystallization: Influence on Opto-Electronic Properties“. en. In: *Advanced Materials* 27.7 (Feb. 2015), pp. 1223–1228. DOI: 10.1002/adma.201403475.

[156]Yoann Olivier et al. „25th Anniversary Article: High-Mobility Hole and Electron Transport Conjugated Polymers: How Structure Defines Function“. en. In: *Advanced Materials* 26.14 (Apr. 2014), pp. 2119–2136. DOI: 10.1002/adma.201305809.

[157]Anne A. Y. Guilbert et al. „Influence of Bridging Atom and Side Chains on the Structure and Crystallinity of Cyclopentadithiophene–Benzothiadiazole Polymers“. In: *Chemistry of Materials* 26.2 (Jan. 2014), pp. 1226–1233. DOI: 10.1021/cm403410w.

[158]Yu Gu, Cheng Wang, and Thomas P. Russell. „Multi-Length-Scale Morphologies in PCPDTBT/PCBM Bulk-Heterojunction Solar Cells“. en. In: *Advanced Energy Materials* 2.6 (June 2012), pp. 683–690. DOI: 10.1002/aenm.201100726.

[159]James T. Rogers et al. „Structural Order in Bulk Heterojunction Films Prepared with Solvent Additives“. en. In: *Advanced Materials* 23.20 (May 2011), pp. 2284–2288. DOI: 10.1002/adma.201003690.

[160]Mauro Morana et al. „Bipolar Charge Transport in PCPDTBT-PCBM Bulk-Heterojunctions for Photovoltaic Applications“. en. In: *Advanced Functional Materials* 18.12 (June 2008), pp. 1757–1766. DOI: 10.1002/adfm.200701428.

[161]Markus C. Scharber et al. „Influence of the Bridging Atom on the Performance of a Low-Bandgap Bulk Heterojunction Solar Cell“. en. In: *Advanced Materials* 22.3 (Jan. 2010), pp. 367–370. DOI: 10.1002/adma.200900529.

[162]Rui Lin et al. „Effects of blend composition on the morphology of Si-PCPDTBT:PC71BM bulk heterojunction organic solar cells“. en. In: *physica status solidi (a)* 212.9 (Sept. 2015), pp. 1931–1940. DOI: 10.1002/pssa.201532009.

[163]Christopher J. Takacs et al. „Quadrites and Crossed-Chain Crystal Structures in Polymer Semiconductors“. In: *Nano Letters* 14.6 (June 2014), pp. 3096–3101. DOI: 10.1021/nl500150t.

[164]Jong Soo Kim et al. „Germanium- and Silicon-Substituted Donor–Acceptor Type Copolymers: Effect of the Bridging Heteroatom on Molecular Packing and Photovoltaic Device Performance“. en. In: *Advanced Energy Materials* 4.18 (Dec. 2014), n/a–n/a. DOI: 10.1002/aenm.201400527.

[165]Pierre M. Beaujuge et al. „Synthetic Principles Directing Charge Transport in Low-Band-Gap Dithienosilole–Benzothiadiazole Copolymers“. In: *Journal of the American Chemical Society* 134.21 (May 2012), pp. 8944–8957. DOI: 10.1021/ja301898h.

[166]Qi Wang et al. „Investigations of the Conjugated Polymers Based on Dithienogermole (DTG) Units for Photovoltaic Applications“. In: *Macromolecules* 47.16 (Aug. 2014), pp. 5558–5565. DOI: 10.1021/ma500831z.

[167]J. Peet et al. „Efficiency enhancement in low-bandgap polymer solar cells by processing with alkane dithiols“. en. In: *Nature Materials* 6.7 (July 2007), pp. 497–500. DOI: 10.1038/nmat1928.

[168]Gregory L. Gibson and Dwight S. Seferos. „“Heavy-Atom” Donor–Acceptor Conjugated Polymers“. en. In: *Macromolecular Chemistry and Physics* 215.9 (May 2014), pp. 811–823. DOI: 10.1002/macp.201400042.

[169]David Gendron et al. „Synthesis and Photovoltaic Properties of Poly(dithieno[3,2-b:2’,3’-d]germole) Derivatives“. In: *Macromolecules* 44.18 (Sept. 2011), pp. 7188–7193. DOI: 10.1021/ma2013496.

[170]Steve Albrecht et al. „Quantifying Charge Extraction in Organic Solar Cells: The Case of Fluorinated PCPDTBT“. In: *The Journal of Physical Chemistry Letters* 5.7 (Apr. 2014), pp. 1131–1138. DOI: 10.1021/jz500457b.

[171]Steve Albrecht et al. „Fluorinated Copolymer PCPDTBT with Enhanced Open-Circuit Voltage and Reduced Recombination for Highly Efficient Polymer Solar Cells“. In: *Journal of the American Chemical Society* 134.36 (Sept. 2012), pp. 14932–14944. DOI: 10.1021/ja305039j.

[172]H. J. C. Berendsen, D. van der Spoel, and R. van Drunen. „GROMACS: A message-passing parallel molecular dynamics implementation“. In: *Computer Physics Communications* 91.1–3 (Sept. 1995), pp. 43–56. DOI: 10.1016/0010-4655(95)00042-E.

[173]Szilárd Páll et al. „Tackling Exascale Software Challenges in Molecular Dynamics Simulations with GROMACS“. en. In: *Solving Software Challenges for Exascale*. Ed. by Stefano Markidis and Erwin Laure. Lecture Notes in Computer Science 8759. DOI: 10.1007/978-3-319-15976-8_1. Springer International Publishing, Apr. 2014, pp. 3–27. ISBN: 978-3-319-15975-1 978-3-319-15976-8.

[174]Michael J. Frisch et al. *Gaussian 09*. Wallingford, CT, USA, 2009.

[175]Jean-Marie Lehn. „Perspectives in Supramolecular Chemistry—From Molecular Recognition towards Molecular Information Processing and Self-Organization“. en. In: *Angewandte Chemie International Edition in English* 29.11 (Nov. 1990), pp. 1304–1319. DOI: 10.1002/anie.199013041.

[176]L. Brunsveld et al. „Supramolecular Polymers“. In: *Chemical Reviews* 101.12 (Dec. 2001), pp. 4071–4098. DOI: 10.1021/cr990125q.

[177]Li-Min Chen et al. „Recent Progress in Polymer Solar Cells: Manipulation of Polymer:Fullerene Morphology and the Formation of Efficient Inverted Polymer Solar Cells“. en. In: *Advanced Materials* 21.14-15 (Apr. 2009), pp. 1434–1449. DOI: 10.1002/adma.200802854.

[178]Beng S. Ong et al. „High-Performance Semiconducting Polythiophenes for Organic Thin-Film Transistors“. In: *Journal of the American Chemical Society* 126.11 (Mar. 2004), pp. 3378–3379. DOI: 10.1021/ja039772w.

[179]Iain McCulloch et al. „Liquid-crystalline semiconducting polymers with high charge-carrier mobility“. en. In: *Nature Materials* 5.4 (Apr. 2006), pp. 328–333. DOI: 10.1038/nmat1612.

[180]Itaru Osaka and Richard D. McCullough. „Advances in Molecular Design and Synthesis of Regioregular Polythiophenes“. In: *Accounts of Chemical Research* 41.9 (Sept. 2008), pp. 1202–1214. DOI: 10.1021/ar800130s.

[181]Tao Wang, Andrew J. Pearson, and David G. Lidzey. „Correlating molecular morphology with optoelectronic function in solar cells based on low band-gap copolymer:fullerene blends“. en. In: *Journal of Materials Chemistry C* 1.44 (Oct. 2013), pp. 7266–7293. DOI: 10.1039/C3TC31235F.

[182]Gaurav Giri et al. „One-dimensional self-confinement promotes polymorph selection in large-area organic semiconductor thin films“. en. In: *Nature Communications* 5 (Apr. 2014), p. 3573. DOI: 10.1038/ncomms4573.

[183]Suchol Savagatrup et al. „Mechanical degradation and stability of organic solar cells: molecular and microstructural determinants“. en. In: *Energy & Environmental Science* 8.1 (Dec. 2014), pp. 55–80. DOI: 10.1039/C4EE02657H.

[184]Nichole Cates Miller et al. „Factors Governing Intercalation of Fullerenes and Other Small Molecules Between the Side Chains of Semiconducting Polymers Used in Solar Cells“. en. In: *Advanced Energy Materials* 2.10 (Oct. 2012), pp. 1208–1217. DOI: 10.1002/aenm.201200392.

[185]Clément Cabanetos et al. „Linear Side Chains in Benzo[1,2-b:4,5-b']dithiophene–Thieno[3,4-c]pyrrole-4,6-dione Polymers Direct Self-Assembly and Solar Cell Performance“. In: *Journal of the American Chemical Society* 135.12 (Mar. 2013), pp. 4656–4659. DOI: 10.1021/ja400365b.

[186]Alan T. Yiu et al. „Side-Chain Tunability of Furan-Containing Low-Band-Gap Polymers Provides Control of Structural Order in Efficient Solar Cells“. In: *Journal of the American Chemical Society* 134.4 (Feb. 2012), pp. 2180–2185. DOI: 10.1021/ja2089662.

[187]Peter K. Watkins, Alison B. Walker, and Geraldine L. B. Verschoor. „Dynamical Monte Carlo Modelling of Organic Solar Cells: The Dependence of Internal Quantum Efficiency on Morphology“. In: *Nano Letters* 5.9 (Sept. 2005), pp. 1814–1818. DOI: 10.1021/nl051098o.

[188]Bobby G. Sumpter and Vincent Meunier. „Can computational approaches aid in untangling the inherent complexity of practical organic photovoltaic systems?“ en. In: *Journal of Polymer Science Part B: Polymer Physics* 50.15 (Aug. 2012), pp. 1071–1089. DOI: 10.1002/polb.23075.

[189]Hsiang-Yu Chen et al. „Silicon Atom Substitution Enhances Interchain Packing in a Thiophene-Based Polymer System“. en. In: *Advanced Materials* 22.3 (Jan. 2010), pp. 371–375. DOI: 10.1002/adma.200902469.

[190]Jörn Ilja Siepmann and Daan Frenkel. „Configurational bias Monte Carlo: a new sampling scheme for flexible chains“. In: *Molecular Physics* 75.1 (Jan. 1992), pp. 59–70. DOI: 10.1080/00268979200100061.

[191]Carl Poelking et al. „Morphology and Charge Transport in P3HT: A Theorist's Perspective“. en. In: *P3HT Revisited – From Molecular Scale to Solar Cell Devices*. Ed. by Sabine Ludwigs. Advances in Polymer Science 265. DOI: 10.1007/12_2014_277. Springer Berlin Heidelberg, 2014, pp. 139–180. ISBN: 978-3-662-45144-1 978-3-662-45145-8.

[192]Alexander A. Voityuk. „INDO/X: A New Semiempirical Method for Excited States of Organic and Biological Molecules“. In: *Journal of Chemical Theory and Computation* 10.11 (Nov. 2014), pp. 4950–4958. DOI: 10.1021/ct500717u.

[193]Thomas Frauenheim et al. „Atomistic simulations of complex materials: ground-state and excited-state properties“. en. In: *Journal of Physics: Condensed Matter* 14.11 (2002), p. 3015. DOI: 10.1088/0953-8984/14/11/313.

[194]Adam Kubas et al. „Electronic couplings for molecular charge transfer: Benchmarking CDFT, FODFT, and FODFTB against high-level ab initio calculations“. In: *The Journal of Chemical Physics* 140.10 (Mar. 2014), p. 104105. DOI: 10.1063/1.4867077.

[195]Adam Kubas et al. „Electronic couplings for molecular charge transfer: benchmarking CDFT, FODFT and FODFTB against high-level ab initio calculations. II“. en. In: *Physical Chemistry Chemical Physics* 17.22 (May 2015), pp. 14342–14354. DOI: 10.1039/C4CP04749D.

[196] Sybille Allard et al. „Organic Semiconductors for Solution-Processable Field-Effect Transistors (OFETs)“. en. In: *Angewandte Chemie International Edition* 47.22 (May 2008), pp. 4070–4098. DOI: 10.1002/anie.200701920.

[197] Michael L. Chabinyc et al. „X-ray Scattering Study of Thin Films of Poly(2,5-bis(3-alkylthiophen-2-yl)thieno[3,2-b]thiophene)“. In: *Journal of the American Chemical Society* 129.11 (Mar. 2007), pp. 3226–3237. DOI: 10.1021/ja0670714.

[198] Eunkyung Cho et al. „Three-Dimensional Packing Structure and Electronic Properties of Biaxially Oriented Poly(2,5-bis(3-alkylthiophene-2-yl)thieno[3,2-b]thiophene) Films“. In: *Journal of the American Chemical Society* 134.14 (Apr. 2012), pp. 6177–6190. DOI: 10.1021/ja210272z.

[199] Iain McCulloch et al. „Semiconducting Thienothiophene Copolymers: Design, Synthesis, Morphology, and Performance in Thin-Film Organic Transistors“. en. In: *Advanced Materials* 21.10-11 (Mar. 2009), pp. 1091–1109. DOI: 10.1002/adma.200801650.

[200] Laure Biniek et al. „Large Scale Alignment and Charge Transport Anisotropy of pBTTT Films Oriented by High Temperature Rubbing“. In: *Macromolecules* 46.10 (May 2013), pp. 4014–4023. DOI: 10.1021/ma400516d.

[201] R. Joseph Kline et al. „Critical Role of Side-Chain Attachment Density on the Order and Device Performance of Polythiophenes“. In: *Macromolecules* 40.22 (Oct. 2007), pp. 7960–7965. DOI: 10.1021/ma0709001.

[202] Christopher Bruner et al. „Molecular Intercalation and Cohesion of Organic Bulk Heterojunction Photovoltaic Devices“. en. In: *Advanced Functional Materials* 23.22 (June 2013), pp. 2863–2871. DOI: 10.1002/adfm.201202969.

[203] W. Ma et al. „Thermally Stable, Efficient Polymer Solar Cells with Nanoscale Control of the Interpenetrating Network Morphology“. en. In: *Advanced Functional Materials* 15.10 (Oct. 2005), pp. 1617–1622. DOI: 10.1002/adfm.200500211.

[204] Mariateresa Scarongella et al. „A Close Look at Charge Generation in Polymer:Fullerene Blends with Microstructure Control“. In: *Journal of the American Chemical Society* 137.8 (Mar. 2015), pp. 2908–2918. DOI: 10.1021/ja510032x.

[205] Mark R. Hansen, Mark Rance, and Arthur Pardi. „Observation of Long-Range 1H-1H Distances in Solution by Dipolar Coupling Interactions“. In: *Journal of the American Chemical Society* 120.43 (Nov. 1998), pp. 11210–11211. DOI: 10.1021/ja9829665.

[206] Kwaku T. Dayie, and Gerhard Wagner, and Jean-François Lefèvre. „Theory and Practice of Nuclear Spin Relaxation in Proteins“. In: *Annual Review of Physical Chemistry* 47.1 (1996), pp. 243–282. DOI: 10.1146/annurev.physchem.47.1.243.

[207] Mark W. F. Fischer, Ananya Majumdar, and Erik R. P. Zuiderweg. „Protein NMR relaxation: theory, applications and outlook“. In: *Progress in Nuclear Magnetic Resonance Spectroscopy* 33.3–4 (Nov. 1998), pp. 207–272. DOI: 10.1016/S0079-6565(98)00023-5.

[208] Michael Ryan Hansen et al. „Columnar Packing Motifs of Functionalized Perylene Derivatives: Local Molecular Order Despite Long-Range Disorder“. In: *Journal of the American Chemical Society* 131.14 (Apr. 2009), pp. 5251–5256. DOI: 10.1021/ja8095703.

[209] Dmytro Dudenko et al. „A Strategy for Revealing the Packing in Semicrystalline π-Conjugated Polymers: Crystal Structure of Bulk Poly-3-hexyl-thiophene (P3HT)“. en. In: *Angewandte Chemie International Edition* 51.44 (Oct. 2012), pp. 11068–11072. DOI: 10.1002/anie.201205075.

[210] Fumitaka Horii et al. „Solid-State NMR and MaterialsSolid-state NMR analyses of the structure and dynamics of polymers in the different states“. In: *Journal of Molecular Structure* 441.2 (Jan. 1998), pp. 303–311. DOI: 10.1016/S0022-2860(97)00303-7.

[211] Scott A. Showalter and Rafael Brüschweiler. „Validation of Molecular Dynamics Simulations of Biomolecules Using NMR Spin Relaxation as Benchmarks: Application to the AMBER99SB Force Field“. In: *Journal of Chemical Theory and Computation* 3.3 (May 2007), pp. 961–975. DOI: 10.1021/ct7000045.

[212] Alrun N. Koller, Harald Schwalbe, and Holger Gohlke. „Starting Structure Dependence of NMR Order Parameters Derived from MD Simulations: Implications for Judging Force-Field Quality“. In: *Biophysical Journal* 95.1 (July 2008), pp. L04–L06. DOI: 10.1529/biophysj.108.132811.

[213] Alexandre Esadze et al. „Dynamics of Lysine Side-Chain Amino Groups in a Protein Studied by Heteronuclear 1H-15N NMR Spectroscopy“. In: *Journal of the American Chemical Society* 133.4 (Feb. 2011), pp. 909–919. DOI: 10.1021/ja107847d.

[214] Catherine Musselman, Hashim M. Al-Hashimi, and Ioan Andricioaei. „iRED Analysis of TAR RNA Reveals Motional Coupling, Long-Range Correlations, and a Dynamical Hinge“. In: *Biophysical Journal* 93.2 (July 2007), pp. 411–422. DOI: 10.1529/biophysj.107.104620.

[215] Scott A. Showalter and Kathleen B. Hall. „A Functional Role for Correlated Motion in the N-terminal RNA-binding Domain of Human U1A Protein“. In: *Journal of Molecular Biology* 322.3 (Sept. 2002), pp. 533–542. DOI: 10.1016/S0022-2836(02)00804-5.

[216] Malene Ringkjøbing Jensen et al. „Exploring Free-Energy Landscapes of Intrinsically Disordered Proteins at Atomic Resolution Using NMR Spectroscopy“. In: *Chemical Reviews* 114.13 (July 2014), pp. 6632–6660. DOI: 10.1021/cr400688u.

[217] Klaartje Houben et al. „Intrinsic Dynamics of the Partly Unstructured PX Domain from the Sendai Virus RNA Polymerase Cofactor P“. In: *Biophysical Journal* 93.8 (Oct. 2007), pp. 2830–2844. DOI: 10.1529/biophysj.107.108829.

[218] Sara R. R. Campos and António M. Baptista. „Conformational Analysis in a Multidimensional Energy Landscape: Study of an Arginylglutamate Repeat“. In: *The Journal of Physical Chemistry B* 113.49 (Dec. 2009), pp. 15989–16001. DOI: 10.1021/jp902991u.

[219] Yi Xue and Nikolai R. Skrynnikov. „Motion of a Disordered Polypeptide Chain as Studied by Paramagnetic Relaxation Enhancements, 15N Relaxation, and Molecular Dynamics Simulations: How Fast Is Segmental Diffusion in Denatured Ubiquitin?“ In: *Journal of the American Chemical Society* 133.37 (Sept. 2011), pp. 14614–14628. DOI: 10.1021/ja201605c.

[220] Eva Meirovitch, Antonino Polimeno, and Jack H. Freed. „Methyl Dynamics in Proteins from NMR Slowly Relaxing Local Structure Spin Relaxation Analysis: A New Perspective“. In: *The Journal of Physical Chemistry B* 110.41 (Oct. 2006), pp. 20615–20628. DOI: 10.1021/jp061403+.

[221] Devon Sheppard et al. „Variation in Quadrupole Couplings of α Deuterons in Ubiquitin Suggests the Presence of Cα-H$\alpha\cdots$O=C Hydrogen Bonds“. In: *Journal of the American Chemical Society* 132.22 (June 2010), pp. 7709–7719. DOI: 10.1021/ja101691s.

[222] Kate A. Stafford et al. „Conformational Preferences Underlying Reduced Activity of a Thermophilic Ribonuclease H“. In: *Journal of Molecular Biology* 427.4 (Feb. 2015), pp. 853–866. DOI: 10.1016/j.jmb.2014.11.023.

[223] Jens Meiler et al. „Model-Free Approach to the Dynamic Interpretation of Residual Dipolar Couplings in Globular Proteins“. In: *Journal of the American Chemical Society* 123.25 (June 2001), pp. 6098–6107. DOI: 10.1021/ja010002z.

[224] Jianhan Chen, Charles L. Brooks Iii, and Peter E. Wright. „Model-free Analysis of Protein Dynamics: Assessment of Accuracy and Model Selection Protocols Based on Molecular Dynamics Simulation“. en. In: *Journal of Biomolecular NMR* 29.3 (July 2004), pp. 243–257. DOI: 10.1023/B:JNMR.0000032504.70912.58.

[225] Jeanine J. Prompers and Rafael Brüschweiler. „General Framework for Studying the Dynamics of Folded and Nonfolded Proteins by NMR Relaxation Spectroscopy and MD Simulation“. In: *Journal of the American Chemical Society* 124.16 (Apr. 2002), pp. 4522–4534. DOI: 10.1021/ja012750u.

[226] Nils-Alexander Lakomek et al. „Self-consistent residual dipolar coupling based model-free analysis for the robust determination of nanosecond to microsecond protein dynamics“. en. In: *Journal of Biomolecular NMR* 41.3 (June 2008), pp. 139–155. DOI: 10.1007/s10858-008-9244-4.

[227] Carl Diehl et al. „Conformational entropy changes upon lactose binding to the carbohydrate recognition domain of galectin-3“. en. In: *Journal of Biomolecular NMR* 45.1-2 (July 2009), pp. 157–169. DOI: 10.1007/s10858-009-9356-5.

[228] Aart J. Nederveen and Alexandre M. J. J. Bonvin. „NMR Relaxation and Internal Dynamics of Ubiquitin from a 0.2 μs MD Simulation“. In: *Journal of Chemical Theory and Computation* 1.3 (May 2005), pp. 363–374. DOI: 10.1021/ct0498829.

[229] Bertil Halle. „The physical basis of model-free analysis of NMR relaxation data from proteins and complex fluids“. In: *The Journal of Chemical Physics* 131.22 (Dec. 2009), p. 224507. DOI: 10.1063/1.3269991.

[230] Samuel Genheden et al. „Starting-Condition Dependence of Order Parameters Derived from Molecular Dynamics Simulations“. In: *Journal of Chemical Theory and Computation* 6.7 (July 2010), pp. 2176–2190. DOI: 10.1021/ct900696z.

[231] Nikola Trbovic et al. „Protein Side-Chain Dynamics and Residual Conformational Entropy“. In: *Journal of the American Chemical Society* 131.2 (Jan. 2009), pp. 615–622. DOI: 10.1021/ja806475k.

[232] Da-Wei Li and Rafael Brüschweiler. „A Dictionary for Protein Side-Chain Entropies from NMR Order Parameters“. In: *Journal of the American Chemical Society* 131.21 (June 2009), pp. 7226–7227. DOI: 10.1021/ja902477s.

[233] Jean-Christophe Hus and Rafael Brüschweiler. „Principal component method for assessing structural heterogeneity across multiple alignment media“. en. In: *Journal of Biomolecular NMR* 24.2 (Oct. 2002), pp. 123–132. DOI: 10.1023/A:1020927930910.

[234] Da-Wei Li and Rafael Brüschweiler. „Iterative Optimization of Molecular Mechanics Force Fields from NMR Data of Full-Length Proteins“. In: *Journal of Chemical Theory and Computation* 7.6 (June 2011), pp. 1773–1782. DOI: 10.1021/ct200094b.

[235] Richard H. Boyd et al. „Conformational dynamics in bulk polyethylene: A molecular dynamics simulation study“. In: *The Journal of Chemical Physics* 101.1 (July 1994), pp. 788–797. DOI: 10.1063/1.468134.

[236] Rishikesh K. Bharadwaj and Richard H. Boyd. „Conformational dynamics in polyethylene under isochoric conditions: A molecular dynamics simulation study“. In: *The Journal of Chemical Physics* 114.11 (Mar. 2001), pp. 5061–5068. DOI: 10.1063/1.1345878.

[237] Eric Johnson, Arthur G. Palmer, and Mark Rance. „Temperature dependence of the NMR generalized order parameter“. en. In: *Proteins: Structure, Function, and Bioinformatics* 66.4 (Mar. 2007), pp. 796–803. DOI: 10.1002/prot.21274.

[238] Jie Han, Richard L. Jaffe, and Do Y. Yoon. „Conformational Characteristics of Polymethylene Chains in Melts and in Various Phantom Chains from Explicit Atom Molecular Dynamics Simulations“. In: *Macromolecules* 30.23 (Nov. 1997), pp. 7245–7252. DOI: 10.1021/ma961772b.

[239] W. Paul, Grant D. Smith, and Do Y. Yoon. „Static and Dynamic Properties of a n-C100H202 Melt from Molecular Dynamics Simulations“. In: *Macromolecules* 30.25 (Dec. 1997), pp. 7772–7780. DOI: 10.1021/ma971184d.

[240] Kostas Ch. Daoulas, Vagelis A. Harmandaris, and Vlasis G. Mavrantzas. „Detailed Atomistic Simulation of a Polymer Melt / Solid Interface: Structure, Density, and Conformation of a Thin Film of Polyethylene Melt Adsorbed on Graphite“. In: *Macromolecules* 38.13 (June 2005), pp. 5780–5795. DOI: 10.1021/ma050176r.

[241] M. B Robertson et al. „NMR study of the energy difference and population of the gauche and trans conformations in solid polyethylene“. In: *Polymer* 42.3 (Feb. 2001), pp. 1261–1264. DOI: 10.1016/S0032-3861(00)00537-1.

[242] Michael M. Fuson, Kent H. Hanser, and M. D. Ediger. „Local Dynamics of Poly(ethylene oxide) in Solution. 2. Vector Autocorrelation Functions and Motional Anisotropy“. In: *Macromolecules* 30.19 (Sept. 1997), pp. 5714–5720. DOI: 10.1021/ma970035s.

[243] Shirley W. I. Siu, Kristyna Pluhackova, and Rainer A. Böckmann. „Optimization of the OPLS-AA Force Field for Long Hydrocarbons“. In: *Journal of Chemical Theory and Computation* 8.4 (Apr. 2012), pp. 1459–1470. DOI: 10.1021/ct200908r.

List of Figures

List of Tables